Generation of Frequency Tunable and Low Phase Noise Micro- and Millimeter-Wave Signals using Photonic Technologies

Von der Fakultät für Ingenieurwissenschaften
Abteilung Elektrotechnik und Informationstechnik
der Universität Duisburg-Essen

zur Erlangung des akademischen Grades

Doktor der Ingenieurwissenschaften

genehmigte Dissertation

von

Dipl.-Ing. Sascha Fedderwitz
aus
Mülheim an der Ruhr

Gutachter: Prof. Dr. habil. Andreas Stöhr
Gutachter: Prof. Dr. rer. nat. Franz-Josef Tegude
Tag der mündlichen Prüfung: 12.03.2015

Abstract

The concept of generating micro- and millimeter-wave signals by optical means offers a variety of unique features compared to purely electronics such as high frequency tunability, ultra-wideband operation and the possibility to distribute micro- and millimeter-wave signals over kilometers of optical fiber to a remote site. These features make the photonic synthesizer concept a very interesting alternative for several applications in the micro- and millimeter-wave regime.

This thesis focuses on the realization and characterization of different photonic synthesizer concepts for the optical generation of frequency tunable and low phase noise micro- and millimeter-wave signals. Advanced microwave photonic approaches utilizing external optical modulation and optical multiplication will be presented, offering high frequency optical millimeter-wave generation up to 110 GHz with superior performances in terms of maximum frequency tuning ranges and phase noise characteristics. In addition, the concept of a novel dual-loop optoelectronic oscillator will be presented that enables optical millimeter-wave signal generation without the need of any electronic reference oscillator. By using the developed dual-loop optoelectronic oscillator, microwave signal generation with tuning ranges in the gigahertz regime has been experimentally demonstrated for the first time.

Acknowledgement

This thesis was mainly originated during my time as a research assistant at the Center for Semiconductor Technology and Optoelectronics at the University of Duisburg-Essen. This work was funded by the European Commission within the integrated project IPHOBAC under grant number 35317 as well as the European Space Agency within the PHOMIGEN project under contract number 21615.

First and foremost, I would like to thank Professor Andreas Stöhr for his continuous support and guidance during my time at the institute and beyond. Moreover, I thank Professor Franz-Josef Tegude for acting as co-referee and for his interest in my work.

I would like to thank all employees at the institute for their cooperativeness and the good atmosphere. Especially, I thank Dr. Rüdiger Buß, Dr. Mario Weiß and Sebastian Babiel for proofreading parts of the thesis. Further on, I would like to thank Prof. Dieter Jäger, Vitaly Rymanov, Heinz Slomka, Melanie Wachholz and all the other nice people who always had an open ear.

Finally, I would like to express my sincere thanks to my wife Kathrin for her support, patience, understanding during my dissertation and above all for her love.

Duisburg, March 2015 Sascha Fedderwitz

Contents

List of Acronyms

Abbreviations

ASE	Amplified spontaneous emission
C-band	Third optical window (1530-1565 nm)
CD	Chromatic dispersion
CDD	Carrier density depletion
CH	Carrier heating
CW	Continuous wave
DD	Dual-drive
DFB	Distributed feedback
DGD	Differential group delay
DSB-CS	Double-sideband with carrier suppression
EAM	Electro-absorption modulator
E-band	Frequency range of 60-90 GHz
EDFA	Erbium-doped fiber amplifier
e/o	Electro-optical
ER	Extinction ratio
ESA	Electrical spectrum analyzer
FSR	Free spectral range
FWHM	Full-width-at-half-maximum
FWM	Four-wave mixing
IL	Insertion loss
K-band	Frequency range of 18-26.5 GHz
LA	Limiting amplifier
LD	Laserdiode
LNA	Low-noise amplifier
LO	Local oscillator
LSB	Lower sideband
MNF	Measurement noise floor
MW	Micro- and millimeter-wave
MWP	Microwave Photonics
MZM	Mach-Zehnder modulator
NSR	Noise-to-signal ratio

OBPF	Optical bandpass filter
ODE	Ordinary differential equation
o/e	Opto-electrical
OEO	Optoelectronic oscillator
OIL	Optical injection locking
OIPLL	Optical injection phase lock loop
OPLL	Optical phase lock loop
PC	Polarization controller
PD	Photodetector
PDL	Polarization dependent loss
PMD	Polarization mode dispersion
PS	Phase shifter
PSD	Power spectral density
QP	Quadrature point
QPSK	Quadrature phase shift keying
RBW	Resolution bandwidth
RC	Resistance-capacitance
RIN	Relative intensity noise
RoF	Radio-over-Fiber
SHB	Spectral hole burning
SMF	Single-mode fiber
SNR	Signal-to-noise ratio
SOA	Semiconductor optical amplifier
SSB	Single-sideband
(T)LS	(Tunable) laser source
TW	Traveling-wave
USB	Upper sideband
UTC	Uni-traveling-carrier
V-band	Frequency range of 50-75 GHz
W-band	Frequency range of 75-110 GHz

Constants and mathematical symbols

B_{N}	Noise equivalent bandwidth
c_0	Speed of light in vacuum ($2.99 \cdot 10^8$ m/s)

D	Dispersion parameter
E	Electrical field strength
f	Frequency
g_{m}	Integrated gain coefficient
G_{opt}	Optical gain
G_{S}	Small-signal open-loop gain
h	Planck constant ($6.626 \cdot 10^{-34}$ Ws^2)
I_{d}	Dark current
I_{ph}	Photocurrent, average
j	Imaginary unit
$\mathrm{J_n}$	First kind Bessel function of n^{th} order
$\mathrm{k_B}$	Boltzman constant ($1.3806504 \cdot 10^{-23}$ Ws/K)
L	Length unit
m	Modulation index
N	Multiplication factor
N_{el}	Electrical noise power
NF	Noise figure
n_{SMF}	Refractive index of SMF-28 (1.4682)
P	Power, general
P_{opt}	Optical power
Q	Quality factor
q	Electron charge ($1.60219 \cdot 10^{-19}$ As)
R	Responsivity
R_{L}	Load resistance
$S_{\mathrm{x}}(f)$	Power spectral density of x
T	Absolute temperature
T_{MZM}	Electro-optic transfer function of an MZM
$V(t)$	Time-dependent voltage, general
V_{bias}	Bias voltage
V_{π}	Half-wave voltage of an MZM, general
$V_{\pi,\mathrm{DC}}$	Half-wave voltage of an MZM, DC electrode
$V_{\pi,\mathrm{RF}}$	Half-wave voltage of an MZM, RF electrode
W_{g}	Band-gap energy

$\mathcal{L}(f)$	Phase noise representation
α	Optical fiber attenuation coefficient
$\beta(\omega)$	Propagation constant
β_{m}	Dispersion parameter of m^{th} order
δ	Noise-to-signal ratio
ε	Nonlinear gain suppression factor
η_{ext}	External quantum efficiency
λ	Wavelength
π	pi (3.14159)
σ^2	Variance
τ	time delay
τ_{CCD}	Carrier lifetime
τ_{CH}	Carrier-phonon scattering time
τ_{SHB}	Carrier-carrier scattering time
ϕ	Phase
$\chi^{(\mathrm{n})}$	Susceptibility of order n
ω	Angular frequency
ω_0	Angular center frequency

List of Own Publications

[A] A. Poloczek, M. Weiß, **S. Fedderwitz**, A. Stöhr, W. Prost, D. Jäger, and F.-J. Tegude, "Integrated InGaAs pin-diode on exactly oriented silicon (001) substrate suitable for 10 Gbit/s digital applications," *IEEE LEOS Annual 2007*, Lake Buena Vista, Florida, USA, 2007

[B] M. Weiß, A.G. Steffan, **S. Fedderwitz**, G. Tsianos, A. Stöhr, and D. Jäger, "Highly-Compact Fibre-Optic Package for 30-300GHz Wireless Transmitter Modules," *2nd Electronics System-Integration Technology Conference*, London, UK, pp. 1111-1114, 2008

[C] A. Stöhr, C.C. Renaud, D. Moodie, A.G. Steffan, L. Pavlovic, D. Jäger, A.J. Seeds, M. Robertson, A. Umbach, M. Vidmar, M. Weiß, V. Rymanov, and **S. Fedderwitz**, "Optical Millimeter-Wave Generation using 1.55µm Photodiodes with and without Integrated Antennas," *2008 URSI General Assembly*, Chicago, Illinois, USA, 2008

[D] A. Stöhr, M. Weiß, **S. Fedderwitz**, D. Jäger, M. Huchard, and B. Charbonnier, "60 GHz Wireless Photonic Link System for 12.5Gb/s Data Transmission," *9. ITG-Fachtagung Photonische Netze*, 28-29 April, Leipzig, Germany, pp. 101-104, ISBN 978-3-8007-3097-1, 2008

[E] K.H. Tan, S.F. Yoon, W. K. Loke, S. Wicaksono, T. K. Ng, K. L. Lew, A. Stöhr, **S. Fedderwitz**, M. Weiß, D. Jäger, N. Saadsaoud, E. Dogheche, D. Decoster, and J. Chazelas, "High responsivity GaNAsSb p-i-n photodetectors at 1.3µm grown by radio-frequency nitrogen plasma-assisted molecular beam epitaxy," *Optics Express*, vol. 16, no. 11, pp. 7720-7725, 2008

[F] M. Weiß, A. Stöhr, M. Huchard, **S. Fedderwitz**, V. Rymanov, B. Charbonnier, and D. Jäger, "Broadband 60GHz Wireless Radio-over-Fibre System for up to 12.5Gb/s Wireless Transmission," *ISIS Summer School & Workshop 2008*, June 2-4, Stockholm, Sweden, 2008

[G] M. Weiß, A. Stöhr, M. Huchard, **S. Fedderwitz**, B. Charbonnier, V. Rymanov, S. Babiel, and D. Jäger, "60GHz Radio-over-Fibre Wireless System for Bridging 10Gb/s Ethernet Links," *European Conference and Exhibition on Optical Communication*, Sept. 21-25, Brussels, Belgium, 2008

[H] **S. Fedderwitz**, A. Stöhr, S. F. Yoon, K. H. Tan, M. Weiß, W. K. Loke, A. Poloczek, S. Wicaksono, and D. Jäger, "Multigigabit 1.3 µm GaNAsSb/GaAs Photodetectors," *Applied Physics Letters*, 93, 033509, pp. 1-3, 2008

[I] **S. Fedderwitz**, V. Rymanov, M. Weiß, A. Stöhr, D. Jäger, A.G. Steffan and, A. Umbach, "Ultra-Broadband and Low Phase Noise Photonic Millimeter-Wave Generation," *Int. Topical Meeting on Microwave Photonics*, Sept. 30 - Oct. 3, Goldcoast, Australia, pp. 283-286, 2008

[J] A. Stöhr, M. Weiß, V. Polo, R. Sambaraju, J.L. Corral, J. Marti, M. Huchard, B. Charbonnier, I. Siaud, **S. Fedderwitz**, and D. Jäger, "60GHz Radio-over-Fiber Techniques for 10Gb/s Broadband Wireless Transmission," *20th Wireless World Research Forum*, Ottawa, Canada, 2008

[K] M. Weiß, M. Huchard, A. Stöhr, B. Charbonnier, **S. Fedderwitz**, and D. Jäger, "60GHz Photonic Millimeter-Wave Link for Short to Medium-Range Wireless Transmission up to 12.5Gb/s," *IEEE Trans. Microw. Theory Tech. and J. Lightw. Techn.*, Special Issue of, vol. 26, no. 15, pp. 2424-2429, 2008, (invited)

[L] V. Rymanov, M. Weiß, A.G. Steffan, **S. Fedderwitz**, A. Stöhr, and D. Jäger, "An Antenna-Integrated Photonic Millimeter-Wave Transmitter," *European workshop on photonic solutions for wireless, access, and in-house networks*, Duisburg, Germany, May 18-20, pp. 77-80, 2009

[M] **S. Fedderwitz**, A. Stöhr, K. H. Tan, S. F. Yoon, M. Weiß, A. Poloczek, W.K. Loke, S. Wicaksono, T.K. Ng, V. Rymanov, A. Patra, E. Tangdiongga, and D. Jäger, "1.3µm GaNAsSb/GaAs UTC-Photodetectors for 10 Gigabit Ethernet Links," *IEEE Photonics Technology Letters*, vol. 21, no. 13, pp. 911-913, 2009

[N] V. Rymanov, **S. Fedderwitz**, M. Weiß, A. Stöhr, and D. Jäger, "Photonic Millimeter-Wave Generation for Ultra-Broadband and Low Phase Noise Applications," *5th Joint Symposium on Opto- & Microelectronic Devices and Circuits*, SODC 2009, Beijing, China, May 9-15, pp. 77-81, 2009

[O] S.F. Yoon, K.H. Tan, W. K. Loke, S. Wicaksono, K. Lew, T.K. Ng, Y.K. Sim, Z. Xu, A. Stöhr, **S. Fedderwitz**, M. Weiss, O. Ecin, A. Poloczek, A. Malcoci, D. Jäger, N. Saadsaoud, E. Dogheche, M. Zegaoui, J.F. Lampin, S. Faci, J. Chazelas, J. A. Gupta, and S.P. McAlister, "Recent Progress in Dilute Nitride-antimonide Materials for Photonic and Electronic Applications," *ECS Transactions*, vol. 19, no. 3, 2009

[P] M. Weiß, A. Stöhr, **S. Fedderwitz**, V. Rymanov, B. Charbonnier, and D. Jäger, "Photonic Millimeter-Wave System for Broadband Wireless Access," *European workshop on photonic solutions for wireless, access, and in-house networks*, Duisburg, Germany, May 18-20, pp. 123-126, 2009

[Q] A. Stöhr, A. Akrout, R. Buß, B. Charbonnier, F. van Dijk, A. Enard, **S. Fedderwitz**, D. Jäger, M. Huchard, F. Lecoche, J. Marti, R. Sambaraju, A.G. Steffan, A. Umbach, and M. Weiß, "60 GHz Radio-over-Fiber Technologies for Broadband Wireless Services," *Journal of Optical Networking*, vol. 8, no. 5, pp. 471-487, 2009, (invited)

[R] K.H. Tan, S.F. Yoon, **S. Fedderwitz**, A. Stöhr, W. K. Loke, S. Wicaksono, T.K. Ng, M. Weiß, A. Poloczek, V. Rymanov, A.S. Patra, E. Tangdiongga, and D. Jäger, "14-GHz GaNAsSb Unitraveling-Carrier 1.3-µm Photodetectors Grown by RF Plasma-Assisted Nitrogen Molecular Beam Epitaxy," *IEEE Electron Device Letters*, vol. 30, no. 6, pp. 590-592, 2009

[S] A. Stöhr, S. Babiel, P.J. Cannard, B. Charbonnier, F. van Dijk, **S. Fedderwitz**, D. Moodie, L. Pavlovic, L. Ponnampalam, C.C. Renaud, D. Rogers,V. Rymanov, Seeds, , A.G. Steffan, A. Umbach, and M. Weiß, "Millimeter-Wave Photonic Components for Broadband Wireless Systems," *IEEE Transactions on Microwave Theory and Techniques*, vol. 58, no. 11, pp. 3071-3082, 2010, invited paper

[T] **S. Fedderwitz**, A. Stöhr, S. Babiel, V. Rymanov, and D. Jäger, "Opto-Electronic Dual-Loop 50 GHz Oscillator with Wide Tunability and Low Phase Noise," *Int. Topical Meeting on Microwave Photonics*, Oct. 5-9, Montreal, Canada, 2010

[U] **S. Fedderwitz**, A. Stöhr, S. Babiel, V. Rymanov, and D. Jäger, "Optoelectronic K-Band Oscillator With Gigahertz Tuning Range and Low Phase Noise," *IEEE Photonics Technology Letters*, vol. 22, no. 20, pp. 1497-1499, 2010

[V] V. Rymanov, S. Babiel, M. Weiß, A.G. Steffan, **S. Fedderwitz**, L. Pavlovic, L. Naglic, A. Stöhr, and D. Jäger, "Continuous-Wave Photonic THz-Transmitter Modules employing Antenna-Integrated 1.55µm Waveguide-Photodetectors," *Int. Forum on Terahertz Spectroscopy and Imaging*, 4th Workshop on Terahertz Technology, Kaiserslautern, March 2-3, Paper Identity No. 40, Abstract 03, 2010

[W] F. van Dijk, B. Charbonnier, S. Constant, A. Enard, **S. Fedderwitz**, S. Formont, I. F. Lealman, F. Lecoche, F.Lelarge, D. Moodie, L. Ponnampalam, C. Renaud, M. J. Robertson, A. J. Seeds, A. Stöhr, and M. Weiß, "Quantum dash mode-locked lasers for millimeter wave signal generation and transmission," *The 23rd Annual Meeting of the IEEE Photonics Society*, November 7-11, Denver, USA, 2010, invited paper

[X] A. Garcia, **S. Fedderwitz**, and A. Stöhr, "Optical Generation of Low-Phase Noise Microwave Signals using Nonlinear MZM and Ultra-Long SOA," *International*

Microwave and Optoelectronics Conference, IMOC 2011, Natal, Oct. 29 - Nov. 01, Brazil, 2011

[Y] S. Babiel, A. Perentos, **S. Fedderwitz**, B. Kunz, S. Iezekiel, and A. Stöhr, "100 GHz Band Photonic Wireless System employing Passive RoF Transmitters," *Int. Symposium on Green Radio over Fibre & All Optical technologies for Wireless Access Networks*, GROWAN 2011, Brest (France), June 15-17, 2011

[Z] A. Garcia, G. Pillet, L. Menager, L. Morvan, S. Babiel, **S. Fedderwitz**, and A. Stöhr, "Low Phase Noise and Frequency Tunable 95-115 GHz Photonic LO Based Upon DSB-SC Modulation in an MZM and FWM in an UL-SOA," *2012 Int. Topical Meeting on Microwave Photonics*, ESA/ESTEC, Noordwijk, The Netherlands, 11-14 September, 978-90-815839-2-3, 2012

List of Figures

1 Introduction

“Microwave Photonics is an interdisciplinary area that studies the interaction between microwave and optical signals” [1]. Within the last few years, the field of Microwave Photonics (MWP) has attracted growing interest worldwide. The term Microwave Photonics describes the study of interacting optical waves and microwaves in novel high-speed and high-frequency photonic devices and their applications [2]. Generally, MWP offers several advantages as compared to other technologies. By integrating the best from the photonic and radio frequency engineering worlds, MWP technologies and components can enable broadband connectivity with unique advantages that cannot be easily achieved by other competing technologies like all electronic systems.

Generally, the microwave region of the electromagnetic spectrum extends from wavelengths of 1 m, down to 1 mm corresponding to a frequency range from 0.3 GHz to 300 GHz. Thus the definition of the microwave region also includes the millimeter-wave region from 30-300 GHz. For simplicity, the abbreviation MW will be used throughout this work for both, microwave and millimeter-wave frequencies.

Usually, an MW signal is generated using a low-frequency and low phase noise electronic oscillator and many stages of frequency multiplication to achieve the desired operation frequency which makes it complicated and costly. In contrast, the generation of MW signals using photonic technologies offers a variety of unique advantages compared to purely electronics due to the extremely broad bandwidth and low loss of optical fibers. In addition to these benefits, MWP technologies also enable low phase noise analog MW signal generation and ultra-wide frequency tuning ranges, as well as broadband modulation capabilities over the entire MW bands [3]. Furthermore, for some applications the distribution of the generated MW signal to a remote site is necessary, which is not practical by electric means due to the high losses of electrical distribution lines such as coaxial cables. The distribution of an MW signal over optical fiber is an ideal solution to overcome the limitations of pure electronic oscillators or multipliers. The generated MW signals can be easily distributed from a central site to a remote station with low complexity by simplifying the equipment requirements. Furthermore, MWP is capable of performing up- and down-conversion of high frequency signals to achieve even higher or lower frequency

signals. This will significantly reduce the complexity of the electrical design if e.g. ultra-high frequency signals are desired where electrical or electronic designs are limited.

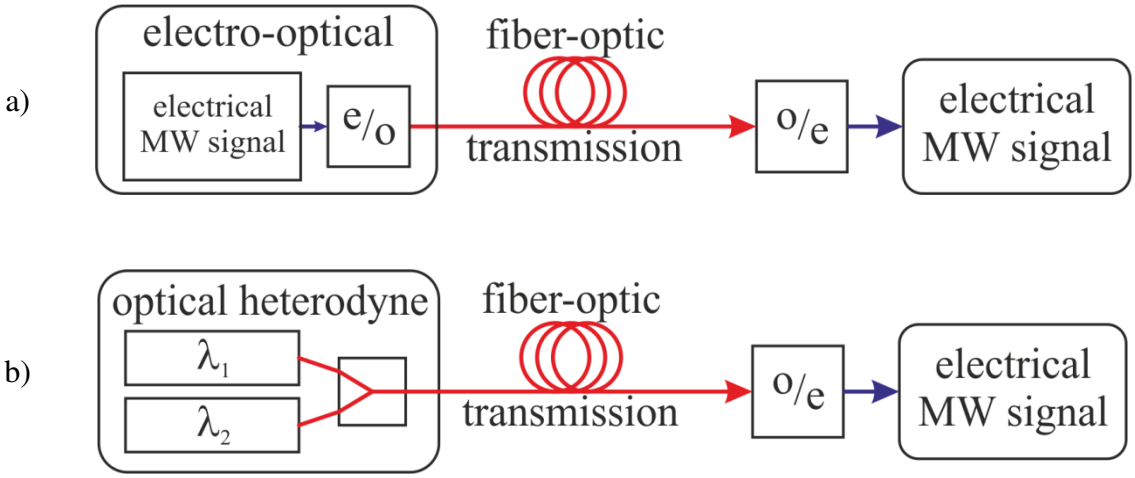

Figure 1.1: Basic principle of an MWP link with different optical signal generation schemes.

The basic concept of an optical link for MW signal transmission, here with two different optical signal generation schemes, is shown in Figure 1.1. Typically, an optical link consists of three different parts; the generation of the optical signal, the transmission of the optical signal and the detection and conversion of the optical signal. The generation of the optical signal can be performed using different schemes. The two most common ways are shown in the figure. In the first scheme (Figure 1.1 a), an electro-optical (e/o) converter, typically a modulated laser, converts the electrical MW signal into an optical signal which contains the information of the electrical MW signal. The second scheme is a pure optical approach named optical heterodyning (Figure 1.1 b). Here, two or more optical modes having different wavelengths are combined such that the difference in wavelengths (or optical frequency) is equal to the desired frequency of the MW signal. Beside these two basic approaches, several further and advanced approaches exist to generate an optical MW signal. After generation, the optical signal is then transmitted over several meters up to kilometers of optical fiber to the remote site where the opto-electrical (o/e) converter, often a photodetector, detects the optical signal and reconverts it into the original electrical MW signal.

MWP is able to address a wide range of applications. One of the widely-used applications is communication including Radio-over-Fiber (RoF) and/or wireless communication [D], [F], [G], [J], [K]. Here, e.g. a frequency range around 60 GHz is of great interest as it

offers several GHz of bandwidth and is furthermore unlicensed. Also other frequency bands are becoming more and more important for wireless communications such as the E-band (60 – 90 GHz) and the W-band (75 – 110 GHz) as both bands are also offering wide bandwidth capabilities. Although communications is a key application field for MWP, there are nevertheless several other important applications fields worth to mention, including radar, instrumentation, radio astronomy, security systems and many others. Although the key objectives among the different applications are of course different, it is also true that in most of the above listed applications a high frequency MW signal is required. The demands on the performance of the generated MW signal of course vary from application to application. Assuming a device will be characterized concerning its frequency tuning range (e.g. a synthesizer for instrumentation), then the signal source must provide an ultra-wide bandwidth in which the operation frequency can be tuned. Here, tuning can be defined twofold; continuously, meaning that the operating frequency can be changed in a continuous manner and coarse or stepwise tuning, meaning that only certain operating frequencies are provided by the source with a more or less fixed difference frequency between two operating frequencies. For applications where tuning is of minor importance often a high-stability MW signal with very low phase noise is needed. Of course, in some applications such as frequency modulated continuous-wave radars, the generated MW signal must provide both, a wide frequency tuning range and low phase noise. To meet these requirements, MWP technologies are particularly suitable as MWP enable both, low phase noise analog MW signal generation and ultra-wide frequency tuning ranges over the entire MW bands [3]. Thus, the concept of generating an MW signal using photonic technologies, which will be stated as a photonic synthesizer in the following, is a very interesting alternative compared to purely electronics.

Several techniques, which can be found in the literature, are investigated to provide a photonic synthesizer which is capable of generating such wide tunable MW signals with low phase noise. One option to achieve an ultra-wide tuning range is based on optical heterodyning, in which two optical modes of different wavelengths beat in a photodetector. The basic idea of heterodyning or photomixing was already invented in the year 1955 [4]. Today, different approaches exist for generating those two optical modes, including dual-mode lasers, dual-frequency lasers or optical comb generators to name just a few. In the latter approach, not just two optical modes but a high number is generated and subsequently filtered. The easiest way of generating two optical modes is to use two

independent free-running lasers in which at least one laser is tunable in wavelength. Using this scheme, the generated MW signal at an advanced photodetector can be tuned in a continuous manner with a frequency resolution just defined by the wavelength tuning resolution of the tunable laser(s). Although this scheme typically provides extremely wide frequency tuning ranges, only limited by the frequency response of the used photodetector, the phase noise performance of such a scheme is rather poor. This is due to the fact that all lasers have random phase fluctuations, resulting in a non-negligible linewidth, that appear in the phase of the resulting heterodyne signal [5]. In order to achieve low phase noise operation, the optical modes must be phase locked. Locking techniques, e.g. optical injection locking or an optical phase lock loop are able to lock the optical modes.

Previously, most optical heterodyne experiments for photonic MW signal generation were performed in the microwave domain. In [6], optical heterodyne frequency generation of up to 20 GHz was achieved using a solid-state dual-frequency laser. Phase noise measurements using this scheme have shown phase noise levels at 100 kHz offset frequency of about -90 dBc/Hz and -120 dBc/Hz for the free-running and the optically phase locked dual-frequency laser, respectively [7], [8]. Although the integrated dual-frequency laser offers low phase noise performance, the maximum operating frequency was limited to about 20 GHz. Nevertheless, compared to solid-state devices, semiconductor lasers benefit from a direct electrical pumping allowing a higher level of integration. By using a multi-section gain-coupled distributed feedback (DFB) laser, a wide frequency tuning range of 46.5-322 GHz has been presented [9] but in this case the laser needed to be locked to an optical comb and thus the frequency of the generated MW signal could only be tuned in steps with a rather poor frequency resolution of no better than 35 GHz.

A possibility to overcome the need for complicated phase locking schemes required in optical heterodyne approaches with two or more lasers is to use optical modulation. In this case, the optical modes are generated from only one laser source. By employing direct or external optical modulation, wide frequency tuning as well as low phase noise performance can be achieved. For example, in a recent experiment using an optical phase modulator and a fixed optical notch filter, continuous frequency tuning from 37.6-50 GHz has been obtained when the electrical drive signal was tuned from 18.8-25 GHz [10]. Although no phase noise measurements were performed in this work, it was shown that the linewidth of

the generated signal was below 5 Hz. However, this work was seriously limited in terms of output power, at 50 GHz an output power level of less than -30 dBm was achieved, signals in excess of 50 GHz could even not be measured in the electrical domain but were seen only in the optical domain. Nevertheless, from this scheme it can be seen that the frequency of the generated MW signal is the double frequency of the electrical drive signal provided by the local oscillator (LO) or electrical synthesizer. As the phase noise of such an external modulation scheme is mainly determined by the phase noise of the LO plus a term depending on the multiplication factor, the phase noise of the LO has to be very small for low phase noise operation. Typically, the phase noise of an electronic high frequency LO with a tuning range up to some tens of GHz is much higher than the phase noise performance of a lower frequency LO. This is due to the fact that for LOs, normally ultra-low phase noise and low frequency crystal or quartz oscillators are used as the basis for generating high frequencies via several complex mixing and multiplication stages. However, this not only increases the complexity and cost but it is also true that the more multiplication and mixing stages, the worse the phase noise performance of the LO.

An option to overcome the use of complex electronic multiplication and mixing stages is to perform the multiplication in the optical domain. As already described above, the frequency can be doubled by optical means when using external modulation. A promising scheme to further increase the optical multiplication factor is presented in [11]. Here, the four-wave mixing effect in a saturated semiconductor optical amplifier (SOA) has been used. It has been shown that a Mach-Zehnder modulator (MZM) with a subsequent SOA is capable of generating a six times optical multiplied mm-wave signal of 42 GHz from a 7 GHz electrical reference oscillator. Furthermore, a phase noise level of -75 dBc/Hz at 1.6 kHz offset from the 42 GHz carrier has been obtained.

Although external modulation in conjunction with an SOA allows optical frequency multiplication as discussed above, this approach still relies on the use of an electrical reference oscillator and consequently, the phase noise of the generated MW signals is related to the phase noise performance of the reference oscillator. To overcome this limitation, the use of an electrical reference oscillator has to be omitted. Early investigations have shown the capability to generate stable picosecond pulses without the need for a reference LO by using semiconductor lasers and a resonant optoelectronic feedback loop [12]. A scheme with a fiber-based resonant feedback loop also known as

optoelectronic oscillator has shown the capability to generate MW signals with extremely low phase noise [13]. The phase noise was measured to be -105 dBc/Hz at 1 kHz offset from a 10 GHz carrier. However, in order to achieve frequency tuning, several bandpass filters selected by a switch had to be used in [13]. In addition, the continuous frequency tuning range inside the bandwidth of the employed bandpass filter was limited to only 110 kHz. With the objective to improve the frequency tuning range of an optoelectronic oscillator, a tunable laser was used in [14]. But although the laser was tunable by ±40 nm in the optical domain, the frequency tunability was still very limited with a maximum tuning range of less than 2 MHz around a central frequency of 9 GHz.

1.1 Aim and Organization of this Thesis

The overall aim of this work is to theoretically and experimentally study the generation of frequency tunable and low phase noise MW signals using photonic technologies. MWP technologies based on optical heterodyning, external modulation and the optoelectronic oscillator concept are the basis for novel and innovative photonic synthesizer concepts studied and developed in this work.

One general aim of this work is to achieve extremely broadband and wideband frequency operation. Innovative approaches based on optical heterodyning have been analyzed and experimentally investigated and will be reported. Since the phase noise performance of optically generated signals using free running laser sources is rather limited, a fiber-based approach based upon external modulation is investigated. In this work, a photonic synthesizer concept based upon external optical modulation is presented and investigated. From experimental results it will be shown, that the developed photonic synthesizer enables low phase noise and frequency tunable signal generation well up into the millimeter-wave region, i.e. well beyond 30 GHz. Beside low phase noise operation, it will be shown that external modulation also represents the fundamental basis for another innovative approach in which a low frequency reference signal (in the optical domain) will be multiplied by optical means before being converter to an electrical high frequency MW signal.

It will be experimentally shown that the phase noise of the generated MW signal using external modulation is fundamentally limited by the phase noise performance of the

employed electrical reference oscillator. To circumvent this limitation, it was another major objective of this work to investigate possibilities for generating frequency tunable MW signals with ultra-low phase noise performances using a concept that does not require any electrical reference local oscillator. In this thesis, a novel approach of an optoelectronic oscillator based on a dual-loop configuration is presented and studied. It will be shown that such a dual-loop optoelectronic oscillator allows high frequency generation with ultra-low phase noise performances while at the same time providing hundreds of MHz frequency tuning range.

This thesis is organized as follows:

The theoretical background of the key optical components and the various photonic techniques required for the development of the various photonic synthesizers studied in this work will be presented in chapter 2. At first the theoretical background of lasers will be described. Here, the focus is laid on the basic theory about the laser's relative intensity noise. Chapter 2.2 deals with the basic theory about external modulation techniques and especially with the transfer characteristic of a Mach-Zehnder modulator. In the next chapter, the nonlinear effect of four-wave mixing in a semiconductor optical amplifier will be analyzed. For connecting a remote transmitter unit to the photonic synthesizer, a single-mode optical fiber will be used. Thus, the basic theory about optical fiber propagation including glass fiber dispersion effects will be described in chapter 2.4. For the remote opto-electronic converter, photodetectors will be used in this work. Therefore, the basic working principle as well as the design differences between different types of photodetectors will be described in the next chapter. At last, the noise contributions in optical links will be analyzed in chapter 2.6. Here, the main focus is laid on phase noise as one aim of this work is to achieve low phase noise operation.

In chapter 3, different MWP approaches for generating wide-tunable and low phase noise micro- and millimeter-wave signals will be studied. At first, in chapter 3.1, approaches based upon optical heterodyning will be discussed and analyzed. While in chapter 3.1.1 the basic operating principle of the optical heterodyning technique will be analyzed, record experimental results on optical heterodyne broadband (DC to 110 GHz) and wideband (70-110 GHz) photonic signal generation which were accomplished during this work will be reported in chapter 3.1.2. Chapter 3.1.3 presents different solutions for further improving

the phase noise performance of the generated MW signals by using optical locking techniques.
In addition to approaches based on optical heterodyning, chapter 3.2 presents wide frequency tunable and low phase noise MW signal generation based on external modulation. At first, the principle of double- and single-sideband modulation is briefly analyzed in chapter 3.2.1. Experiments using double-sideband modulation with carrier suppression are then presented in chapter 3.2.2, showing wide tunable MW signal generation with low phase noise. Next, innovative approaches utilizing optical multiplication schemes based on optical nonlinearities will be studied in chapter 3.2.3. Experimental results are presented showing that very high optical multiplication factors can be achieved.

In chapter 4, the generation of MW signals with ultra-low phase noise performance based on the optoelectronic oscillator approach will be discussed. At first, chapter 4.1 describes the general principle of an optoelectronic oscillator using a single-loop configuration while chapter 4.2 is dealing with advanced multi-loop configurations. Next, in chapter 4.3, the invention of a novel dual-loop optoelectronic oscillator that allows frequency tuning is presented and experimentally, MW signal generation with ultra-low phase noise performance and hundreds of MHz frequency tuning range is presented.

Finally, in chapter 5, a concluding summary discussion on the developed innovative approaches and the achieved results is presented. Chapter 6 lists all references used in this thesis and all components and measurement equipment used for this work is listed in the Appendix.

1.2 Research Projects

Parts of this thesis were performed within the frame of two research projects, namely the European integrated project IPHOBAC and the European Space agency mission PHOMIGEN. In the following, the general objectives of these projects which are related to this work will be briefly summarized.

The IPHOBAC (**I**ntegrated **Pho**tonic Millimeter-Wave Functions For **B**ro**a**dband **C**onnectivity) project started in 06/2006 and ended in 11/2009. It was funded by the

European Commission under grant number 35317. The aims of IPHOBAC were the development of innovative photonic mm-wave components and integrated functions for applications in the field of communications, security, radar and instrumentation using MWP technologies. The key objectives of IPHOBAC include the development of photonic sources enabling the generation of wideband tunable and low phase noise MW signals, the development of transmitters and receivers based upon electro-absorption modulation enabling broadband and processing of MW signals, as well as the development of ultra-wideband photomixers based on broadband high-speed photodetectors enabling the detection of the optically generated MW signals. Innovative functions and systems using these IPHOBAC components were further developed including the generation of high power, low phase noise MW signals, the allocation of a fully tunable 30-300 GHz MW source, as well as a 60 GHz RoF system including wireless transmission as described above.

The PHOMIGEN (Microwave **Pho**tonics **Mi**llimeter-wave **Gen**eration) mission was initiated by the European Space Agency in March 2009 and is coordinated by THALES under contract number 21615. The intention of the PHOMIGEN project is to develop a fully functional and RF tested photonic synthesizer including a remote transmitter unit. One aim of PHOMIGEN was to develop a photonic synthesizer concept which allows for generating millimeter-wave signals around 100 GHz with at least 10% frequency tuning range. The frequency resolution for stepwise frequency tuning should be better than 1 GHz. Furthermore, the photonic synthesizer should provide low phase noise performance (-70 dBc/Hz at 1 kHz offset, -75 dBc/Hz at 10 kHz offset and -80 dBc/Hz at 100 kHz offset from the carrier). Another research aim was to investigate possibilities that allow efficient optical frequency multiplication with an as high as possible multiplication factor.

2 Photonic Technologies – Theoretical Background

The general objective of this thesis was to investigate and realize systems which provide high tunability and low phase noise performance in the mm-wave range using MWP technologies. The photonic synthesizer is a concept for generating such frequency tunable and low phase noise continuous-wave signals. In comparison to purely electrical oscillators, a photonic synthesizer features ultra-wideband and high-frequency operation up to the mm-wave region. The basic concept of a photonic synthesizer is shown in Figure 2.1. In general, a photonic synthesizer consists of an optical transmitter which provides an MW signal in the optical domain. A transmission medium (an optical fiber in this work) is used to transmit the optical MW signal to a remote site (receiver). The receiver (a photodetector in this work) receives the optical MW signal on the one hand and converts it into an electrical MW signal on the other hand.

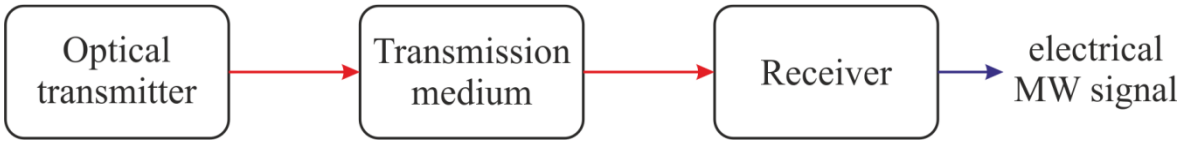

Figure 2.1: Basic concept of a photonic synthesizer.

The intention of this chapter is to give a brief overview and a theoretical background of the main optical components and photonic technologies which have been used in this thesis. For all photonic links, optical sources such as laserdiodes are essential. Thus, in section 2.1, the basic operating principle of laserdiodes, often operating at 1.55 µm wavelength, is discussed. External modulation techniques that allow the generation of optical double sideband signals are discussed in chapter 2.2. For efficient optical frequency multiplication of a low-frequency optical reference signal it is possible to exploit the nonlinearities in a semiconductor optical amplifier. This is expected to result in a multiplication of the reference MW signal in the optical domain and thus would allow generating even higher frequencies at the output of a photonic synthesizer. Chapter 2.3 will discuss the nonlinearities in semiconductor optical amplifiers leading to four-wave mixing of the optical double sideband input signal. Before the modulated light will be o/e converted in a photodetector (see chapter 2.5), it propagates through optical fibers. The influence of the fibers absorption and dispersion characteristics on the optical signal will be analyzed in 2.4. Besides output power and frequency tunability, the phase noise of the generated MW

signals is of great importance for many applications. Chapter 2.6 will analyze the different contributions to the overall phase noise of a photonic synthesizer.

2.1 Laserdiodes

For all microwave photonic links, the laser is the most used light source. A laserdiode (LD) is characterized by several properties of which the most important are wavelength (λ), the optical linewidth (full-width-at-half-maximum - FWHM), the output power and the relative intensity noise (RIN).

The third optical window (C-band) is of great interest for several applications in the field of MWP, as the attenuation of a standard single-mode fiber at 1.55 µm wavelength is minimum ($\alpha \approx 0.2$ dB/km). Another important advantage of the C-band is that optical amplifiers working in this band like the most common erbium-doped fiber amplifiers (EDFA) are commercially available. Lasers and receivers for this wavelength range became already available in the late 1980s [15].

In the ideal case, the spectrum of a laser is monochromatic but in reality a laser exhibits a non-negligible optical linewidth. The optical linewidth of a laser is defined as the width of its optical spectrum at FWHM. The fundamental physical limitation for this finite optical linewidth, which is also stated as the natural linewidth, comes from spontaneous emission events inside the laser cavity. The natural linewidth is a characteristic of all lasers mainly arising from phase fluctuations of the lasing optical field $E(t)$ [16]. Drifts of the resonator length as well as effects like e.g. the Doppler-effect can also contribute to the linewidth [17]. The E-field of the laser is affected by amplitude and phase fluctuations. However, the amplitude fluctuations are on the one hand comparably low and on the other hand, stabilizing mechanisms exist to further minimize these fluctuations. Therefore, in a first instance, the E-field of a single-mode laser can be modeled as quasi-monochromatic and amplitude-stabilized electromagnetic wave with phase fluctuations [18] resulting in

$$E(t) = E_0 \cdot \mathrm{e}^{\mathrm{j}(\omega_0 t + \phi_0(t))}, \tag{2.1}$$

where E_0 represents the constant amplitude, ω_0 is the angular monochromatic optical center frequency and $\phi_0(t)$ the random phase fluctuations which lead to the non-negligible linewidth.

As this thesis mainly deals with the photonic generation of low noise MW signals, the following analysis will especially concentrate on the RIN of a laser, as it affects the overall performance of a photonic synthesizer. It can decrease the maximum achievable electrical signal-to-noise ratio (SNR) in a photonic synthesizer when the synthesizer's phase noise is limited by RIN. Here, with electrical SNR the signal-to-noise ratio at the output of a square-law detector is meant. Laser RIN is defined as the ratio between the mean square intensity fluctuation spectral density $\langle \Delta P \rangle^2$ (in a 1-Hz bandwidth) and the mean square average light output power $\langle P_{\mathrm{opt}} \rangle^2$ [19]:

$$RIN = \frac{\langle \Delta P \rangle^2}{\langle P_{\mathrm{opt}} \rangle^2}. \tag{2.2}$$

In this case, the RIN is specified in units of Hz^{-1}, but more often it is given in logarithmic form as dB/Hz. If, for example, the dominant noise source in a photonic synthesizer concept with modulation index m and noise equivalent bandwidth $B_{\mathrm{N,el}}$ is the laser's relative intensity noise, then the SNR decreases with the RIN as follows [20]:

$$SNR = \frac{m^2}{2 \cdot B_{\mathrm{N,el}} \cdot RIN}. \tag{2.3}$$

The RIN for the 1.55 µm laserdiode used for the experiments in this work (Agilent Tunable Laser 81680A) has a value of RIN^{dB} = -145 dB/Hz. A more detailed analysis of RIN can be found in chapter 2.6.

2.2 External Modulation

By modulating the injection current, the laserdiode's output can be modulated resulting in an optical double-sideband signal when the modulating injection current is a cosine function. However, the direct modulation of laserdiodes is limited to about 30 GHz which is a too low bandwidth for achieving extremely broadband or wideband frequency

operation in the mm-wave region. Thus, external modulation techniques must be used as they provide much higher bandwidths than directly modulated lasers.

Two different types of electro-optical modulators are used for external laser modulation: phase modulators and intensity modulators. As for intensity modulators, one commonly used modulator is the semiconductor based electro-absorption modulator (EAM). The physical effects, which are also valid for most phase modulators are the Franz-Keldysh effect, observed in conventional bulk semiconductors, and the Quantum-confined Stark effect, observed in quantum well structures. The Franz-Keldysh effect causes a change of the band-gap energy and therefore a change in the absorption spectrum due to an applied electric field [21], [22]. In the case of the Quantum-confined Stark effect, an applied electric field causes a shift in the energy states of the quantum wells such that the energy of the ground state is being modulated by the electric field [23].

Beside semiconductor based modulators, the most common phase and interferometric intensity modulators are made on crystal electro-optic materials such as lithium niobate ($LiNbO_3$) which provides e.g. large electro-optic coefficients and high bandwidths to name just a few examples [24], [25]. One of the most often used modulator concept on $LiNbO_3$ substrate is the Mach-Zehnder modulator (MZM) which has also been used in this work. The operating principle of the MZM is based on the linear electro-optic effect (Pockels effect). The Pockels effect is described as a modification of the refractive index of a medium in proportion to the applied electric field strength [26].

The Mach-Zehnder modulator

The MZM is based upon a Mach-Zehnder interferometer where the incoming optical signal is split equally into two beams which propagate independently through two different optical paths and then are recombined accordingly. For the simplest form of an MZM (see Figure 2.2), the optical wave propagating in one of the optical paths will be phase modulated by applying an electrical voltage. This will result in an intensity modulation at the output of the MZM.

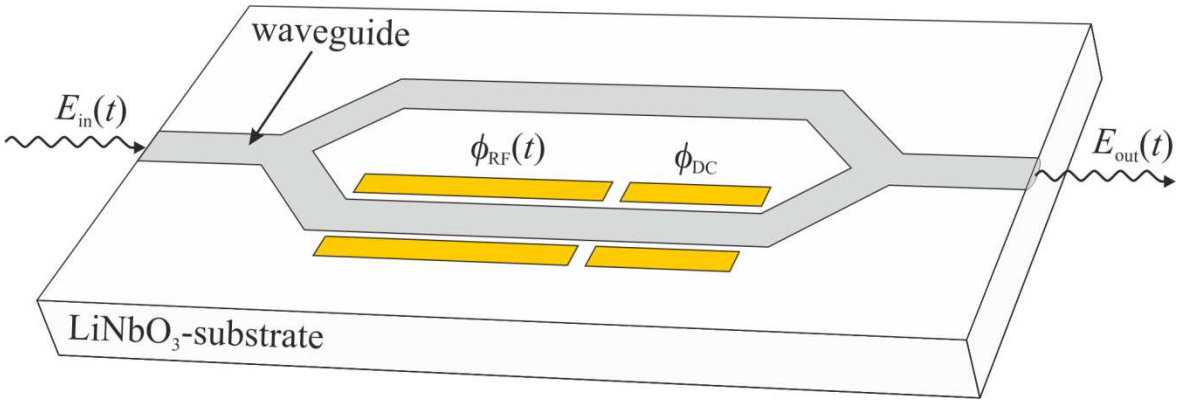

Figure 2.2: Schematic of a single-drive Mach-Zehnder modulator.

In many cases the modulator consists of an RF and a DC modulation section as shown in Figure 2.2. By applying a modulation voltage, e.g. a sinusoidal signal to the RF electrodes, a phase shift of $\phi_{\mathrm{RF}}(t)$ is induced. The DC section is used to adjust the static operating point of the MZM. By applying a static electrical voltage to the DC electrodes, a static phase shift of ϕ_{DC} is induced. If e.g. the applied static electrical voltage is chosen such that the phase difference between both optical paths becomes π, the optical signal at the output of the MZM is cancelled out due to destructive interference. By changing the applied static electrical voltage such that the phase difference becomes zero, the optical signal at the output becomes maximum due to constructive interference. With this capability of changing the phase difference and thus the operation point of the MZM, different modulation techniques can be achieved. As can be obtained from the electro-optic transfer function shown in Figure 2.3, two techniques of electro-optical modulation are common by applying a static electrical voltage (bias voltage - V_{bias}) at the DC section.

- First, by adjusting V_{bias} to the quadrature point (QP), i.e. to $V_0 + V_{\pi,\mathrm{DC}}/2$. At quadrature, the optical input signal is being modulated in a quasi-linear manner for small signal amplitudes of the modulation RF signal. This is an important modulation approach especially for multilevel data modulation formats requiring a high linearity like e.g. in RoF links [27].
- Second, by adjusting V_{bias} close to $V_0 + V_{\pi,\mathrm{DC}}$ (carrier suppression – CS), the static phase shift between both arms becomes π. In the case of an ideal MZM, the incoming light is now modulated in such a way that the fundamental optical carrier is cancelled out and only the RF sidebands appear at the modulator's output. This results in a situation in which the RF frequency applied to the modulator is doubled when the modulator's output signal is detected by a photodiode [28]. This

modulation scheme is called double-sideband signal with carrier suppression (DSB-CS) modulation and is often used as a solution to double the applied RF frequency by optical means.

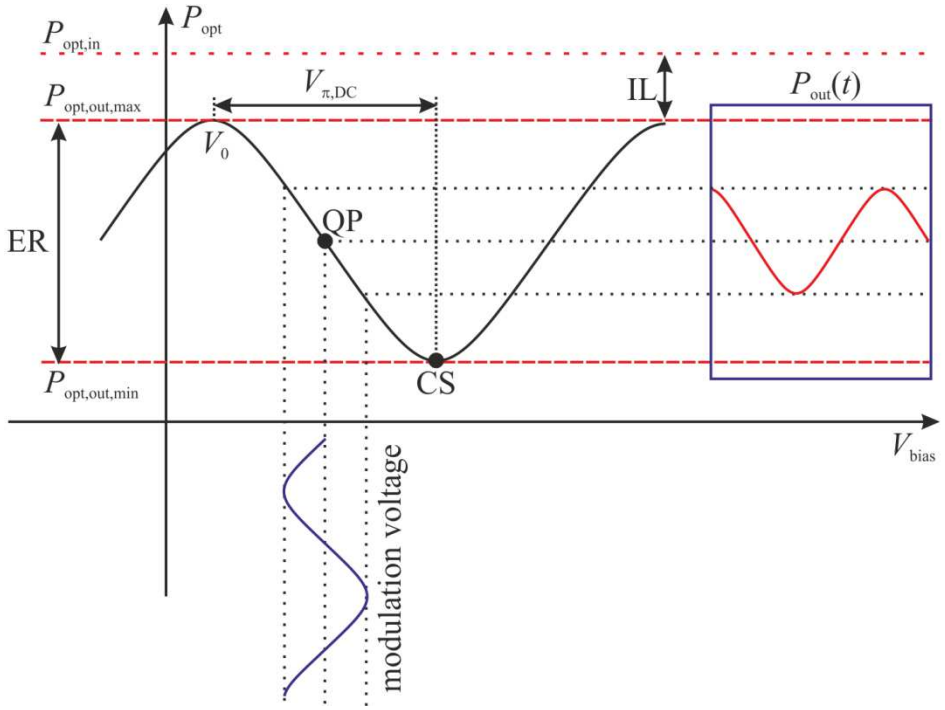

Figure 2.3: Nonlinear electro-optic transfer function of a MZM with important key parameters.

In reality, an MZM is subject to material and technological variations, resulting in the fact that the split ratio between both arms is not exactly 50%. Therefore, a small amount of the fundamental mode is transmitted even in the case of carrier suppression. Furthermore, a specific amount of the optical power gets lost due to material-specific losses, splitting and recombining of the waveguide, as well as fiber-chip (input) and chip-fiber (output) coupling losses. The addition of all these losses are denoted as the insertion loss (IL) which is described as the ratio between the optical input power $P_{\mathrm{opt,in}}$ and the optical output power $P_{\mathrm{opt,out}}$. As already mentioned above, the DC section is used to change the phase difference between both paths and thus to change the modulation format. Due to the fact that the optical input signal has a finite linewidth, i.e. it is not monochromatic, a phase difference of π (DSB-CS) is only achieved for one specific wavelength. As a result, destructive interference cannot be perfect, i.e. the optical carrier cannot be cancelled out completely. This also leads to a finite extinction ratio (ER) [29], [30]. The ER is defined as

the ratio of the maximum achievable output power ($P_{\mathrm{opt,out,max}}$) to the minimum achievable output power ($P_{\mathrm{opt,out,min}}$).

The mathematical expression of the electro-optic transfer function (T_{MZM}) of an MZM as a function of an applied modulation voltage $V(t)$ is given by [31], [32]

$$T_{\mathrm{MZM}} = \frac{P_{\mathrm{opt,out}}(t)}{P_{\mathrm{opt,in}}(t)} = \frac{IL}{2}\left[1 + \cos\left(\pi\frac{V(t)}{V_{\pi}} + \phi_{\mathrm{b}}\right)\right], \tag{2.4}$$

where ϕ_{b} is a static retardation (phase shift) resulting from an internal path length mismatch between the two paths of the MZM. The parameter V_{π}, which is denoted as the half-wave voltage, is the voltage needed to cause a phase shift of π between both arms. It should be noted that in practice V_{π} will be different for DC and RF. As most modulators have separated electrodes for DC and RF supply (see Figure 2.2), the modulation voltage $V(t)$ is separated into the constant bias voltage V_{bias}, supplied at the DC electrode, and the time-varying modulation voltage $V_{\mathrm{RF}}(t)$, supplied at the RF electrode. Assuming that $V_{\mathrm{RF}}(t)$ is a sinusoidal voltage, the modulation voltage $V(t)$ can be stated as

$$V(t) = V_{\mathrm{bias}} + V_{\mathrm{RF}}(t) = V_{\mathrm{bias}} + V_{\mathrm{e}}\cos[\omega_{\mathrm{e}}t + \phi_{\mathrm{e}}(t)], \tag{2.5}$$

with V_{e} and ω_{e} are the voltage amplitude and angular frequency ($\omega_{\mathrm{e}} = 2\pi f_{\mathrm{e}}$) of the electrical drive signal, respectively. The term $\phi_{\mathrm{e}}(t)$ represents a random process that induces phase fluctuations, which can be interpreted as a parasitic phase modulation, to the RF signal [33]. These fluctuations will be analyzed in chapter 2.6. Thus, the electro-optic transfer function can be extended to

$$T_{\mathrm{MZM}} = \frac{IL}{2}\left[1 + \cos\left(\pi\frac{V_{\mathrm{RF}}(t)}{V_{\pi,\mathrm{RF}}} + \pi\frac{V_{\mathrm{bias}}}{V_{\pi,\mathrm{DC}}} + \phi_{\mathrm{b}}\right)\right]. \tag{2.6}$$

Assuming an optical carrier which is linear polarized and aligned to the polarization state axis of the modulator, the electric field of the optical input wave $E_{\mathrm{in}}(t)$ can be expressed in scalar form as

$$E_{\mathrm{in}}(t) = E_0 \cdot \cos[\omega_0 t + \phi_0(t)]. \tag{2.7}$$

E_0 and ω_0 are the electric field amplitude and angular frequency ($\omega_0 = 2\pi f_0$) of the optical carrier, respectively. The term $\phi_0(t)$ also represents a random process analog to the electrical signal, but for the optical carrier. To derive an expression for the electric field of the optical wave at the output of the MZM, it has to be considered that the electro-optic transfer function given above is related to the optical power. Thus, if the insertion loss is neglected, the proportionality between the optical output power and the optical electric field is

$$\begin{aligned} P_{\mathrm{opt,out}}(t) \propto T_{\mathrm{MZM}} \cdot P_{\mathrm{opt,in}}(t) &\propto \frac{1}{2}\left[1 + \cos\left(\pi \frac{V_{\mathrm{RF}}(t)}{V_{\pi,\mathrm{RF}}} + \pi \frac{V_{\mathrm{bias}}}{V_{\pi,\mathrm{DC}}} + \phi_{\mathrm{b}}\right)\right] \\ &\propto \cos^2\left[\frac{1}{2}\left(\pi \frac{V_{\mathrm{RF}}(t)}{V_{\pi,\mathrm{RF}}} + \pi \frac{V_{\mathrm{bias}}}{V_{\pi,\mathrm{DC}}} + \phi_{\mathrm{b}}\right)\right] \propto E_{\mathrm{opt,out}}^2(t). \end{aligned} \tag{2.8}$$

If the optical carrier is now applied to the optical input port of the MZM and modulation is performed, the normalized field of the modulated optical signal at the output port is given by [34], [35]

$$E_{\mathrm{out}}(t) = E_0 \cdot \cos[\omega_0 t + \phi_0(t)] \cdot \cos\left\{\frac{\phi_{\mathrm{DC}}}{2} + \frac{\pi}{2V_{\pi,\mathrm{RF}}} V_{\mathrm{e}} \cos[\omega_{\mathrm{e}} t + \phi_{\mathrm{e}}(t)]\right\}, \tag{2.9}$$

where

$$\phi_{\mathrm{DC}} = \pi \frac{V_{\mathrm{bias}}}{V_{\pi,\mathrm{DC}}} + \phi_{\mathrm{b}}. \tag{2.10}$$

Due to the nonlinearity of the electro-optic transfer function, it is obvious that various spectral harmonics will be generated, depending on the amplitude V_{e} of the modulation signal and on the static phase shift ϕ_{DC} caused by the static bias. To get a better understanding of the output spectrum, equation (2.9) can be expanded using Bessel functions [36], [37] leading to

$$
\begin{aligned}
E_{\mathrm{out}}(t) &= E_0 \cos\left(\frac{\phi_{\mathrm{DC}}}{2}\right) \mathrm{J}_0(m) \cos[\omega_0 t + \phi_0(t)] \\
&+ E_0 \cos\left(\frac{\phi_{\mathrm{DC}}}{2}\right) \left\{ \sum_{n=1}^{\infty} \mathrm{J}_{2n}(m) \begin{bmatrix} \cos\left[\omega_0 t + \phi_0(t) - 2n\left(\omega_{\mathrm{e}} t + \phi_{\mathrm{e}}(t)\right) + n\pi\right] \\ + \cos\left[\omega_0 t + \phi_0(t) + 2n\left(\omega_{\mathrm{e}} t + \phi_{\mathrm{e}}(t)\right) - n\pi\right] \end{bmatrix} \right\} \\
&+ E_0 \sin\left(\frac{\phi_{\mathrm{DC}}}{2}\right) \left\{ \sum_{n=1}^{\infty} \mathrm{J}_{2n-1}(m) \begin{bmatrix} \cos\left[\omega_0 t + \phi_0(t) - (2n-1)\left(\omega_{\mathrm{e}} t + \phi_{\mathrm{e}}(t)\right) + n\pi - \frac{\pi}{2}\right] \\ + \cos\left[\omega_0 t + \phi_0(t) + (2n-1)\left(\omega_{\mathrm{e}} t + \phi_{\mathrm{e}}(t)\right) - n\pi + \frac{\pi}{2}\right] \end{bmatrix} \right\},
\end{aligned}
\tag{2.11}
$$

where $\mathrm{J_n}$ is the first kind Bessel function of n^{th} order and m is the phase modulation index expressed as

$$
m = \frac{\pi}{2V_{\pi,\mathrm{RF}}} V_{\mathrm{e}}. \tag{2.12}
$$

2.3 Nonlinearities in a Semiconductor Optical Amplifier

Due to nonlinearities in materials, which are based on the material's second- or third-order susceptibility, optical nonlinearities are showing an instantaneous response. This is referred to as parametric nonlinearities. The result of this is a modulation of a material parameter, like e.g. the refractive index. This leads to different nonlinear effects such as frequency doubling, sum and difference frequency generation and four-wave mixing to name just a few. The cause for these parametric processes is that bound electrons of a material are showing a nonlinear response to an applied optical field. In the case of a nonlinear semiconductor optical amplifier (SOA), this means for example a carrier density change induced by the optical signals at the amplifier's input [38]. Here, the main parametric process is related to the third-order susceptibility $\chi^{(3)}$ [39], [40]. It is responsible for the nonlinear interaction of four coherent optical fields resulting in phenomena such as parametric amplification, third-harmonic generation and four-wave mixing (FWM) [41], [42]. FWM is a quite efficient way to generate new optical modes, e.g. for optical multiplication schemes, and has been extensively studied in optical fibers [43]-[47]. However, to achieve a high FWM conversion efficiency in optical fibers, an issue is that the optical input power has to be very high. Furthermore, the interaction length has to be very long, i.e. several kilometers of optical fiber have to be used. Here, nonlinear SOAs are able to address these issues. The major advantage of using an SOA is that the nonlinearities are so strong that the interaction length is just a few hundredths of micrometers up to a few

millimeters resulting in a high FWM conversion efficiency. Another advantage is that much lower optical input powers are required to drive an SOA in the nonlinear region.

Theory of FWM in SOAs

In an SOA four-wave mixing can occur between two optical fields of different frequencies having the same polarization. A strong signal, the so called pump, at angular frequency ω_p and a usually weaker signal, also called probe, at $\omega_s = \omega_p - \Delta\omega$ are injected to the SOA. The beating of the two optical fields causes a modulation of the amplifier's gain at the beat frequency $\Delta\omega$. Thus, new optical fields referred to as FWM beams at $\omega_p + \Delta\omega$ and $\omega_p - 2\Delta\omega$ are generated [11], [48]. Figure 2.4 shows the optical spectrum at the output of a nonlinear SOA. P_p, P_s, P_{FWM+} and P_{FWM-} are defined as the powers of the pump, the signal and the FWM products, respectively.

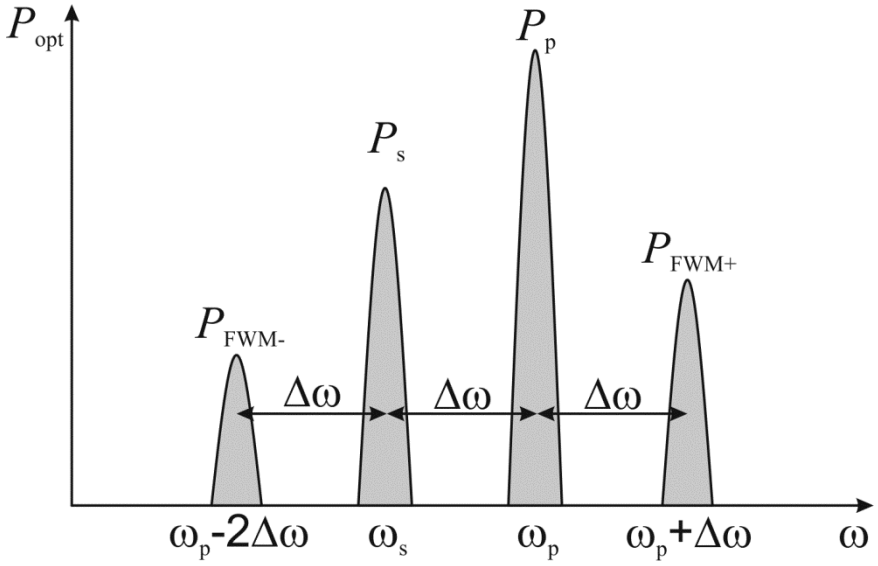

Figure 2.4: Optical input and output spectrum of an SOA using a conventional FWM configuration.

The mechanisms that lead to FWM in an SOA are related to nonlinear gain dynamics. These nonlinear gain dynamics are based on different physical effects and are referred to as inter- and intraband effects [38].

Interband effects, which are dominant at low $\Delta\omega$, refer to carrier-hole recombination between the material's conduction- and valence band and lead to a modulation of the carrier density [38]. This modulation is a result of the pump-signal beating and is referred to as carrier density depletion (CDD). As a consequence, the optical carriers will be

depleted and thus, the optical gain will be reduced. The characteristic time of CDD is the stimulated lifetime and therefore, it represents the carrier lifetime (τ_{CDD}). Typically, the carrier lifetime is in the order of several hundreds of picoseconds [49], [50]. Intraband effects are basically based on two mechanisms. These include carrier heating (CH) and spectral hole burning (SHB) [38], [49]-[57].

CH describes a process which increases the average carrier temperature, i.e. the temperature of the electrons in the conduction band and holes in the valence band, to a temperature beyond the lattice temperature. It is caused by two physical processes that contribute to the temperature change of the carriers [38], [49]. The first process is due to stimulated emission which removes "cold" carriers, i.e. carriers which are cooler than the average, near the bottom of the corresponding band. In the second process, referred to as free carrier absorption, free carriers will be shifted to higher energy levels in the bands. This will result in an overall increase of the temperature and thus to a decrease of the gain. Here, a change of a few degrees results in a decrease of the gain of several percent [55], [56]. The overall characteristic time of CH (τ_{CH}) consists of two contributions. The average time the carriers need to cool down to the lattice temperature is referred to as carrier-phonon scattering time (τ_{CH1}). The second contribution is the carrier-carrier scattering time (τ_{CH2}). This is the time the carrier population needs to reach a heated equilibrium state related to the non-heated initial state. The characteristic time of CH is in the order of hundreds of femtoseconds [38], [49].

As a strong pump has to be injected for FWM, a hole in the intraband carrier distribution will be created. This effect is called spectral hole burning. Within the respective band, the occupation probability of the carriers will be modulated which furthermore leads to a fast modulation of the gain. As a result, a deep spectral hole is burned in the profile of the gain spectrum. At a few milliwatts of operation power, this nonlinear suppression of the gain is affected by a few percent [57]. The time associated with SHB is the carrier-carrier scattering time (τ_{SHB}), i.e. within the bands the carriers need this time, which is typically in the order of hundreds of femtoseconds, to reach a thermal equilibrium [49].

To describe FWM in SOAs based on the contributions of these physical effects, several numerical models have been investigated. The first model, which is based on coupled-mode equations, was investigated by Agrawal in 1988 [58]. Since then, many groups have

published improved models which are usually also based on coupled-mode equations [49], [59], [60]. As most of these numerical models describe the change of the optical field inside the SOA during propagation, the interaction length of the SOA is split into equally sized small regions in which the physical properties are assumed to be constant. Due to the nonlinear response of the semiconductor material as a consequence of the incoming optical signal, local changes of the carrier distribution at any longitudinal position z within the interaction length are produced. These local density changes are the result of CDD, CH and SHB. Due to the fact that each contribution has an influence on the gain spectrum, the total gain consists of the sum of these gain contributions g_{j} with j = CDD, CH and SHB. Because these gain contributions are coupled through rate equations to the equation which describes the field propagation along the waveguide, a set of partial differential equations with the two independent variables time (t) and longitudinal position (z) have to be solved numerically to calculate the optical field at the output of the SOA [61]. Although a high accuracy can be achieved, if a dense partition for the equally sized small regions inside the interaction length is used, this model is very complex resulting in very long computation times.

Based on the model described in [61], Cassioli et al. reduced the device description to its input-output relation by reducing the initial set of partial differential equations to a set of ordinary differential equations (ODEs) [50]. The advantages are that on the one hand, time is the only independent variable and on the other hand, that there is no need to explicitly calculate the field inside the device which makes this model much less complex. However, it should be noted that in contrast to the theory developed in [61], where the partial differential equations are separated for electrons and holes, here just the electrons are taken into account as they offer a smaller effective mass and therefore a longer relaxation time compared to the holes. This allows the model to be easily integrated in numerical simulation environments, if the material parameters of the device are known. In the following, the model based on this theory will be described.

In a first step, both sides of the partial differential equations will be integrated over the device length, i.e. from 0 to the interaction length L of the device which is the basis to simplify the model from [61] to a model, where time is the only independent variable. This leads to three new variables denoted as h_{j} given as [50]

$$h_{\mathrm{j}}(t) = \Gamma \int_0^L g_{\mathrm{j}}(t, z')\,\mathrm{d}z', \tag{2.13}$$

where j represents the contributions from CDD, CH and SHB to the integrated gain coefficient (g_{m}) of the device and Γ is attributed to the mode confinement factor. The integrated gain coefficient, with time as the only independent variable, is the sum of the three variables $h_{\mathrm{j}}(t)$ and expressed as

$$g_{\mathrm{m}}(t) = h_{\mathrm{CDD}}(t) + h_{\mathrm{CH}}(t) + h_{\mathrm{SHB}}(t). \tag{2.14}$$

With the expression of the integrated gain coefficient, the overall gain of the device can be calculated by

$$G(t) = \exp[g_{\mathrm{m}}(t)] = \exp[h_{\mathrm{CDD}} + h_{\mathrm{CH}} + h_{\mathrm{SHB}}]. \tag{2.15}$$

With the expression for the overall gain as well as the new variables h_{j}, the initial set of partial differential equations from [61] are thus reduced to the following ODEs [50]

$$\frac{\mathrm{d}h_{\mathrm{CDD}}}{\mathrm{d}t} = -\frac{h_{\mathrm{CDD}}}{\tau_{\mathrm{CDD}}} - \frac{1}{P_{\mathrm{S}}\tau_{\mathrm{CDD}}}[G(t) - 1]P_{\mathrm{in}}(t) + \frac{g_0}{\tau_{\mathrm{CDD}}} \tag{2.16a}$$

$$\frac{\mathrm{d}h_{\mathrm{SHB}}}{\mathrm{d}t} = -\frac{h_{\mathrm{SHB}}}{\tau_{\mathrm{SHB}}} - \frac{\varepsilon_{\mathrm{SHB}}}{\tau_{\mathrm{SHB}}}[G(t) - 1]P_{\mathrm{in}}(t) - \frac{\mathrm{d}h_{\mathrm{CH}}}{\mathrm{d}t} - \frac{\mathrm{d}h_{\mathrm{CDD}}}{\mathrm{d}t} \tag{2.16b}$$

$$\frac{\mathrm{d}h_{\mathrm{CH}}}{\mathrm{d}t} = -\frac{h_{\mathrm{CH}}}{\tau_{\mathrm{CH}}} - \frac{\varepsilon_{\mathrm{CH}}}{\tau_{\mathrm{CH}}}[G(t) - 1]P_{\mathrm{in}}(t). \tag{2.16c}$$

Here, P_{S} represents the saturation power of the SOA, g_0 is the unsaturated gain and $P_{\mathrm{in}}(t)$ is the optical power applied to the SOA. The parameters $\varepsilon_{\mathrm{SHB}}$ and $\varepsilon_{\mathrm{CH}}$ are the nonlinear gain suppression factors related to SHB and CH, respectively.

Due to the fact that any change of the optical gain results in a change of the effective waveguide refractive index, the phase $\phi(t)$ of the optical output field, which is dependent on the refractive index, is also affected. Therefore, the optical gain can also be traced back

to the phase of the optical output field. This leads to the linear function for the phase given as [50]

$$\phi(t) = -\frac{1}{2}\alpha_{\mathrm{CDD}}[h_{\mathrm{CDD}} - g_0] - \frac{1}{2}\alpha_{\mathrm{CH}}h_{\mathrm{CH}}, \tag{2.17}$$

with α_{CDD} and α_{CH} being the phase-amplitude coupling coefficients with respect to CDD and CH. As the phase-amplitude coupling coefficients are not part of the ODEs, it is obvious that they do not affect the gain. Nevertheless, these parameters are essential as the optical output field is not only dependent on the gain but also on the phase. From the set of ODEs (2.16), along with (2.14) and (2.17), one can see that the only function which stimulates the gain and the phase of the SOA results from the optical input power $P_{\mathrm{in}}(t)$. Thus, the optical field $E_{\mathrm{out}}(t)$ at the output of the SOA as a function of the injected optical field $E_{\mathrm{in}}(t)$ is given as [50]

$$E_{\mathrm{out}}(t) = E_{\mathrm{in}}(t) \cdot \exp\left[\frac{1}{2}g_{\mathrm{m}}(t) + \mathrm{j}\phi(t)\right]. \tag{2.18}$$

Here, the output field describes an ideal device, as the amplified spontaneous emission (ASE) noise which typically appears in optical amplifiers is neglected. The contribution of ASE noise will be modeled by an equivalent noise source inserted to the input of the SOA. Therefore, $P_{\mathrm{in}}(t)$ enhances to [50]

$$P_{\mathrm{in}}(t) \propto |E_{\mathrm{in}}(t) + E_{\mathrm{ASE}}(t)|^2, \tag{2.19}$$

resulting in the optical output field $E_{\mathrm{out}}(t)$ including ASE as

$$E_{\mathrm{out}}(t) = [E_{\mathrm{in}}(t) + E_{\mathrm{ASE}}(t)] \cdot \exp\left[\frac{1}{2}g_{\mathrm{m}}(t) + \mathrm{j}\phi(t)\right]. \tag{2.20}$$

The complete detailed analysis of ASE contribution for this case can be also found in [50]. Furthermore, a general description of ASE and other noise processes can be found in chapter 2.6 of this work.

2.4 Optical Fiber Propagation

As the intention of this work is to develop a photonic synthesizer including a remote transmitter unit, the needed MW signal has to be transmitted to a remote site. Thus, this chapter analyzes the transmission via an optical fiber. In the year 1970, the invention of silica fibers with losses below 20 dB/km led to a revolution in the field of optical fiber communication techniques [62]. Furthermore, due to an improved fabrication technology [63], an attenuation factor of α = 0.2 dB/km at a wavelength of 1.55 µm has been achieved in 1979 [64] which is still state-of-the-art. If an optical signal with power P_0 is introduced into an optical fiber with length L, the transmitted optical power P_T is affected by the attenuation factor α which is given in units of dB/km as [65]

$$\alpha = -\frac{1}{L} 10 \log_{10}\left(\frac{P_\mathrm{T}}{P_0}\right). \tag{2.21}$$

Nowadays, such standard optical single-mode fibers (SMF) are widely used in optical fiber links. Nevertheless, SMF are subject to further limiting factors that have to be considered, such as chromatic dispersion and polarization mode dispersion.

Chromatic dispersion

Chromatic dispersion (CD) describes the broadening of an input signal after traveling through a dispersive medium such as an SMF. The interaction between photons and the fiber materials gives rise to a frequency dependent refractive index $n(\omega)$. This leads to the fact that the different spectral components of an optical signal travel at different velocities through the SMF on the one hand and to a relative phase delay between the different wavelengths on the other hand. Nevertheless, CD in a standard optical SMF is also dependent on the wavelength. For different wavelengths, the influence of CD on the optical signal is also different. While the CD is negligible for a wavelength of 1.3 µm, it is important for photonic links working at 1.55 µm wavelength.

Assuming a DSB signal, CD induces a periodically power fading of the signal depending on the propagation distance along an SMF resulting from a relative phase delay between the different wavelengths. As a consequence, the information will be lost at the first total extinction. The phase ϕ of a single wavelength with angular frequency ω propagating through an SMF is given by [66]

$$\phi = \beta(\omega) \cdot z, \tag{2.22}$$

with z as the travel distance and $\beta(\omega)$ as the propagation constant. By expanding the propagation constant in a Taylor series around $\omega = \omega_0$, the expression for the phase can be derived as [67]

$$\begin{aligned} \phi &= n(\omega)\frac{\omega}{\mathrm{c}_0} \cdot z \\ &= \beta_0 \cdot z + \beta_1 \cdot (\omega - \omega_0) \cdot z + \frac{1}{2}\beta_2 \cdot (\omega - \omega_0)^2 \cdot z + \frac{1}{6}\beta_3 \cdot (\omega - \omega_0)^3 \cdot z + \cdots, \end{aligned} \tag{2.23}$$

where c_0 is the speed of light in vacuum and

$$\beta_\mathrm{m} = \left(\frac{\mathrm{d}^\mathrm{m}\beta}{\mathrm{d}\omega^\mathrm{m}}\right)_{\omega = \omega_0}, \qquad (m = 0, 1, 2, \ldots). \tag{2.24}$$

The parameters β_0 and β_1 are related to constant phase shift and group velocity, respectively. Both terms have no influence on the distortion of the signal. The main contribution on the pulse broadening is caused by the second-order term β_2 which is given by [68]

$$\beta_2 = -\frac{2\pi \mathrm{c}_0 D}{\omega_0^2} = -\frac{D\lambda_0^2}{2\pi \mathrm{c}_0}. \tag{2.25}$$

The parameter D is the fiber dispersion parameter, which has a typical value for a standard SMF at a wavelength of 1.55 µm of $D = 17$ ps/nm/km. Neglecting all parameters rather than β_2 and substituting (2.25) into (2.23), the resulting phase becomes

$$\phi = \frac{1}{2}\beta_2 \cdot (\omega - \omega_0)^2 \cdot z = -\frac{D\lambda_0^2}{4\pi \mathrm{c}_0} \cdot (\omega - \omega_0)^2 \cdot z. \tag{2.26}$$

Assuming a modulated optical signal comprising first- and second-order upper and lower sidebands at angular frequencies $\pm n\omega_\mathrm{m}$ ($n = 1, 2$) around the optical carrier frequency ω_0 is introduced into an optical fiber, the optical field can be expressed as

$$\begin{aligned} E_{\mathrm{in}} &= A_0 \exp[\mathrm{j}\omega_0 t] \\ &+ A_{-1}\exp[\mathrm{j}(\omega_0 - \omega_{\mathrm{m}})t] + A_{+1}\exp[\mathrm{j}(\omega_0 + \omega_{\mathrm{m}})t] \\ &+ A_{-2}\exp[\mathrm{j}(\omega_0 - 2\omega_{\mathrm{m}})t] + A_{+2}\exp[\mathrm{j}(\omega_0 + 2\omega_{\mathrm{m}})t], \end{aligned} \tag{2.27}$$

where A_{m} denotes the amplitudes of each optical component. Evaluating the phase given in (2.26) for the optical carrier and for the first- and second order sidebands gives

$$\phi_{0,1,2} = \begin{cases} 0 \\ -\dfrac{D\lambda_0^2}{4\pi \mathrm{c}_0} \cdot (\omega_{\mathrm{m}})^2 \cdot z \\ -\dfrac{D\lambda_0^2}{4\pi \mathrm{c}_0} \cdot (2\omega_{\mathrm{m}})^2 \cdot z. \end{cases} \tag{2.28}$$

From (2.28), it is obvious to see that the phase changes quadratically with the order of the sideband which means that the phase of any sideband can be related to the first-order sideband by

$$\phi_{\mathrm{n}} = n^2 \phi_1. \tag{2.29}$$

If the optical field given in (2.27) has traveled through the SMF, the resulting field at the output becomes

$$\begin{aligned} E_{\mathrm{out}} &= A_0 \exp[\mathrm{j}\omega_0 t] \\ &+ A_{-1}\exp[\mathrm{j}(\omega_0 - \omega_{\mathrm{m}})t + \phi_1] + A_{+1}\exp[\mathrm{j}(\omega_0 + \omega_{\mathrm{m}})t + \phi_1] \\ &+ A_{-2}\exp[\mathrm{j}(\omega_0 - 2\omega_{\mathrm{m}})t + 4\phi_1] + A_{+2}\exp[\mathrm{j}(\omega_0 + 2\omega_{\mathrm{m}})t + 4\phi_1]. \end{aligned} \tag{2.30}$$

If the optical field will now be detected by a photodetector (PD), a photocurrent proportional to the square of the optical field will be generated (see chapter 2.5). As the carrier and the sidebands interfere with each other, the phase difference will lead to either destructive or constructive interference. This will cause a periodic dispersion induced power penalty depending on the fiber length. Simulations have been performed showing this dependency for different frequencies (Figure 2.5).

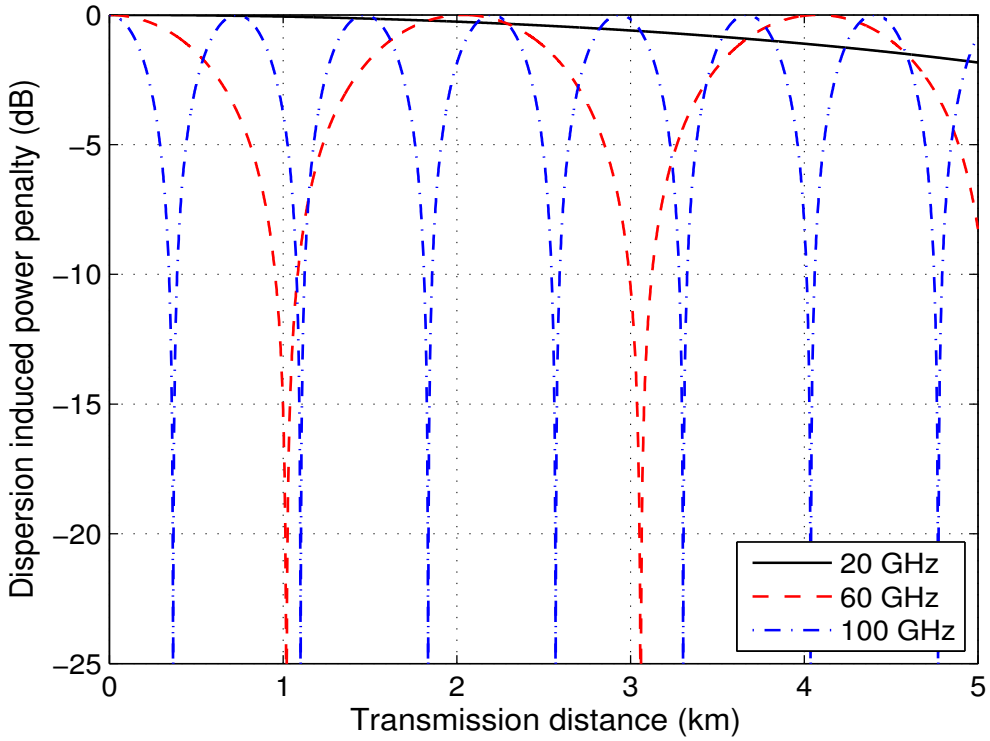

Figure 2.5: Dispersion induced power penalty as a function of SMF length for different frequencies at a wavelength of 1550 nm and a dispersion factor of $D = 17$ ps/nm/km.

It should be noted that the simulation has been made on the assumption that the modulation is chirp-free. In reality, any modulator exhibits at least a small chirp which has an influence on the dispersion induced power penalty [69]. Nevertheless, the chirp of the MZM used in this work is so small that it can be stated as a zero-chirp modulator. The knowledge on the CD and thus on the dispersion induced power penalty is of great interest e.g. for remote applications. Assuming an optical 100 GHz signal should be transmitted via a standard SMF to a remote site, the length of the SMF has to be carefully selected in order that there is no extinction. From the simulation results of the 100 GHz signal one can see that there are discrete lengths where the extinction is about zero.

Polarization mode dispersion

Polarization mode dispersion (PMD) describes the broadening of an input signal due to a phase delay between the input polarization states. In an ideal SMF, the core is perfectly circular which means that the refractive index for both polarization states of a fundamental mode is the same. However, in reality mechanical and thermal stresses lead to asymmetries in the core which means that the core is not perfectly circular. These stresses are caused by

manufacturing and environmental influences. This, in fact, leads to a small change in the refractive index for each polarization state, and it is referred to as birefringence [70]. Birefringence will result in different optical axes, whereas the axis with the smaller refractive index in which the group velocity of the polarization mode is higher is called the fast axis. Analog to this, the axis with the larger refractive index is called the slow axis. In general, this means that the two orthogonal polarization states travel at different velocities through the fiber, leading to a differential group delay (DGD) between the fast and the slow axis, as illustrated in Figure 2.6. DGD can further induce polarization rotation as the birefringence changes randomly along the fiber, i.e. it is not constant over the fiber length caused by twist, stress and bend. Therefore, a misalignment of polarization occurs at the output of the SMF even if the polarization of the optical mode was aligned at the input of the fiber. Since the responsivity of a PD depends on the relative polarization, a power penalty will be induced which is referred to as polarization dependent loss (PDL).

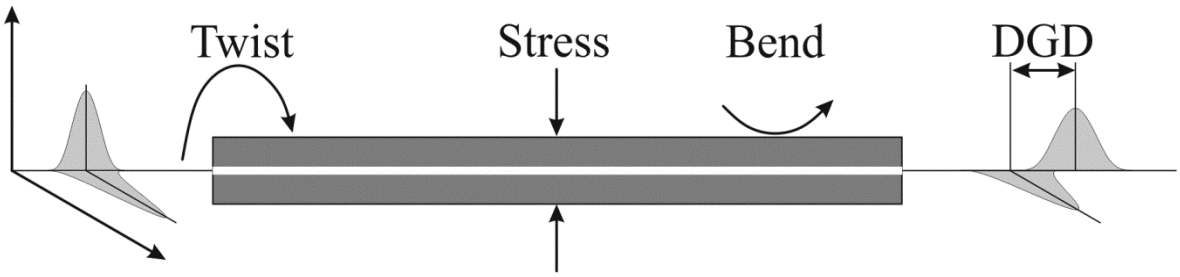

Figure 2.6: Schematic of an SMF showing the effect of PMD.

Due to the fact that PMD is in general a much smaller effect than CD due to a $\sqrt{L}$ dependence [39] and since the PDL of the PDs used in this work is below 0.3 dB, the influence of PMD will be neglected. Nevertheless, a detailed analysis of PMD including the fundamental concepts and the basic theory can be found in [71].

2.5 Photodetectors

In general, a photodetector is an optoelectronic device that converts optical energy into electrical energy. Nowadays, several types of photodetectors depending on the requirements for specific applications are used. These include vacuum-tube devices, thermal detectors, metal-semiconductor-metal photodetectors and semiconductor photodiodes to name just a few.

Semiconductor PDs are widely used, as they offer small dimensions (integration), low drive voltages, high linearity, fast response and so forth. The main physical mechanism is absorption, i.e. a photon with energy $\mathrm{h}f$ is absorbed inside the active region of a PD which creates an electron-hole pair. For this, it is necessary that the photon energy is larger than the band-gap energy of the semiconductor [72], which can be mathematically expressed as

$$\mathrm{h}f = \mathrm{h} \cdot \frac{\mathrm{c}_0}{\lambda} \geq W_g, \tag{2.31}$$

where h, λ and W_g are the Planck's constant, wavelength and the band-gap energy of the semiconductor, respectively. If the PD is illuminated and a bias voltage is applied, the optical generation of free moving carriers results in a generated photocurrent. For the characterization of the semiconductor material, the external quantum efficiency (η_{ext}) is introduced which is defined as the ratio between the number of generated electron-hole pairs per incident photon. The PD itself is described by the conversion efficiency referred to as responsivity, which is

$$R = \eta_{\mathrm{ext}} \cdot \frac{\mathrm{q}\lambda}{\mathrm{hc}_0} = \frac{I_{\mathrm{ph}}}{P_{\mathrm{opt}}}, \tag{2.32}$$

with q being the electron charge, I_{ph} the photocurrent and P_{opt} the optical input power. A PD is a so-called square-law detector, which means that the photocurrent is proportional to the square of the optical electric field. Thus, the photocurrent becomes

$$I_{\mathrm{ph}} = R \cdot P_{\mathrm{opt}} \propto R \cdot \left|E_{\mathrm{opt}}\right|^2. \tag{2.33}$$

From (2.33), it is obvious that if the optical field is modulated, i.e. time dependent, then the resulting photocurrent also becomes time dependent. In this thesis, the output power of a PD is defined as the power which is related to an impedance of 50 Ω.

Several semiconductor based PDs having different performances and different designs have been developed. Although the most common is the pin-PD, new designs have been investigated, such as the uni-traveling-carrier PD (UTC-PD) and the traveling-wave PD (TW-PD).

pin-photodetector

In a pin-PD, an intrinsic absorption layer (i-zone) is inserted between the p- and n-doped semiconductor layers. Applying a reverse bias voltage to the PD causes an electric field inside the intrinsic or rather absorption region. As a result, electron-hole pairs generated by photo excitation are separated and transported to their respective contacts. In the simplest case, a pin-PD is vertically illuminated. The two major bandwidth limiting factors are the carrier-transit time and the external resistance-capacitance (RC) time [73]. The carrier transit time is defined as the time a carrier takes to drift across the absorption region. It is dependent on the carrier velocities and therefore on the applied electric field inside the PD. It is desirable to achieve short transit times, as these result in an increase of the bandwidth. This can be realized by decreasing the absorption width at the expense of a lower responsivity [74]. The RC time is mainly affected by the inherent and any parasitic capacitance. It is the time needed for charging and discharging these capacitances of the PD. To reduce the RC time and therefore to increase the bandwidth of the PD, the capacitance can be decreased either by making the device area smaller or by increasing the absorption width [75]. It is obvious that a design trade-off for achieving the maximum bandwidth of the device exists, as an increase or decrease of the absorption width will result in higher transit or RC times, respectively. Another critical issue is the space charge effect [76], i.e. high optical input powers can perturb the electrical field. As a result, the carriers start drifting and the relationship between the current and the optical input power becomes nonlinear. This leads to distortions of the photocurrent and thus the electrical output signal if the optical input signal is modulated.

One way to overcome these design limitations is to let the direction of the incident light be in plane to the pin structure, i.e. side illumination using a waveguide design [77]. The advantage is that the effect of the absorption region thickness on the quantum efficiency is rather small if the absorption region is long enough. However, the major drawback is to achieve high input coupling efficiencies, as the dimensions of the absorption layer are very small. Low input coupling efficiencies will result in limited quantum efficiency of the PD [78]. Nevertheless, already in 1994, Kato et. al. have presented waveguide pin PDs obtaining a high 3 dB bandwidth of up to 110 GHz [79]. Also, waveguide PDs having an electrical 3 dB bandwidth of 90 GHz are commercially available [80].

UTC-photodetector

A promising candidate to achieve high frequency operation is the uni-traveling-carrier photodetector. The first UTC-PD design was proposed and presented by NTT [81]. Unlike a conventional pin-PD, the absorption takes place in a neutral p-type layer where the band-gap is smallest. The UTC-PD further consists of a typically undoped wide-gap (depleted) carrier-collection layer. If an incoming photon now generates an electron-hole pair, the minority electrons drift into the depleted collection layer. Due to the fact that the absorption layer is quasi-neutral, the holes underlie a very fast recombination within the dielectric relaxation time, as their transport is a collective motion. As a result, the UTC-PD response is primarily determined by the electron transport and hence the name uni-traveling-carrier [82].

UTC-PDs exhibiting a 3 dB bandwidth up to 310 GHz at 1.55 µm wavelength [83] and an RF output power of more than 20 mW at 100 GHz [84] were already presented. It should be mentioned that the high bandwidth of 310 GHz was calculated from the femtosecond-pulse response, i.e. at continuous wave operation the bandwidth could be decreased, as the DC current is much higher, resulting in saturation effects [85]. Nevertheless, the UTC-PD is capable to handle high optical input powers, resulting in a very linear behavior to the electrical output power. The space charge effect is drastically reduced as only electrons, whose velocity is much higher than that of holes, contribute to the charge transport. Therefore, saturation effects only appear if the current density becomes an order of magnitude higher than that for a pin-PD [86]. The high saturation and high speed capability of a UTC-PD can be achieved at low or even zero bias voltage, due to the fact that at a relatively low electric field or even with the built-in field of the p-n junction, the electron velocity is high [87].

TW-photodetector

As already mentioned before, a waveguide design can be used to overcome design limitations of a conventional pin-PD. An enhancement of this design is the traveling-wave photodetector. However, the TW-PD differs from the lumped-element waveguide PD, as it is a distributed structure that overcomes the RC bandwidth limitation [88]. The TW-PD consists of a combination of both, optical waveguide and electrical waveguide or transmission line. If an optical signal is applied to the input facet of the TW-PD, it will be guided and gradually absorbed over the device length [89]. This will result in a distributed

current that contributes to the overall current propagating along the electrical transmission line [90]. The bandwidth limitation of such a TW-PD results from the optical absorption coefficient on the one hand and from the velocity mismatches between the optical and electrical (photocurrent) waves on the other hand [91]. This means that even if the device is longer than the absorption length, the bandwidth is not affected. A record 3 dB bandwidth of up to 570 GHz at 780 nm wavelength calculated from the femtosecond-pulse response has been reported in [92]. At 1.55 µm wavelength, ultra wideband operation (0.06-1 THz) utilizing a WR10 waveguide-coupled TW-PD has been experimentally and theoretically investigated [93].

2.6 Noise in Optical Links

As already described at the beginning of this thesis, the generation and distribution of MW signals in the optical domain is a key technology for several applications. However, for most applications the requirements on high spectral purity of the generated MW signal are very stringent. Accordingly, the generation and distribution due to the optical link must not degrade the spectral quality of the signals, as this gives rise to random fluctuations of the photocurrent.

In an optical link, the different noise contributions are relative intensity noise (RIN) caused by the laser, amplified spontaneous emission (ASE) noise due to optical amplifiers and thermal and shot noise generated in the PD. Due to the fact that the noise contributions can be treated as stationary zero-mean Gaussian random processes [94], it allows to use the variance of the noise induced current variations. Thus, the independent noise contributions can be easily summarized as current sources because they all act together during o/e-conversion [95]. Passive optical and electrical components such as optical fibers, electric cables, connectors etc. have no influence on the overall noise so that they can be neglected. Furthermore, an MZM can also be treated as a passive component without noise contributions [96]. In an MZM, just waveguide losses are present which do not provide noise.

In addition to the above mentioned noise contributions, phase noise is also important, as it degrades the system performance. Due to the special characteristics of phase noise, it will be analyzed independently from the other noise sources.

Thermal Noise

Thermal noise, also known as Johnson noise [97] or Nyquist noise [98], is evoked from a random movement of carriers in a conductor, resulting in random fluctuations of the generated current. The thermal noise in a PD, for instance, can be modeled as a current source i_{th} in parallel to the circuit load resistor R_{L}. The variance of the thermal noise is then [70]

$$\sigma_{\mathrm{th}}^2 = \langle i_{\mathrm{th}}^2(t) \rangle = \frac{4\mathrm{k_B}TB_{\mathrm{N,el}}}{R_{\mathrm{L}}}, \tag{2.34}$$

where $\mathrm{k_B}$ is the Boltzmann constant, T the absolute temperature and $B_{\mathrm{N,el}}$ the noise equivalent electrical bandwidth. If the reference resistor of a subsequent element R_{ref} is matched to the load resistor ($R_{\mathrm{ref}} = R_{\mathrm{L}}$), maximum power transfer occurs and the thermal noise power becomes [28]

$$N_{\mathrm{el,th}} = \left(\frac{\sqrt{\sigma_{\mathrm{th}}^2}}{2} \right)^2 R_{\mathrm{ref}} = \mathrm{k_B}TB_{\mathrm{N,el}}. \tag{2.35}$$

Assuming the noise equivalent bandwidth to be 1 Hz and the temperature 290 K (room temperature), the thermal noise power becomes ~ $4 \cdot 10^{-21}$ W or approximately -174 dBm.

Shot Noise

In 1918, Walter Schottky established the theoretical basis for shot noise [99]. Shot noise is a quantum noise representing random fluctuations of a signal due to the discrete nature and random arrival time of the charge carriers. In the case of a PD, the individual photons arrive randomly, thus leading to random fluctuations of the photocurrent I_{ph}. In addition to the generated photocurrent, the dark current I_{d} of the PD has to be taken into account. Dark current flows even in the absence of light due to the presence of current leakage paths in the PD. It results from thermally excited carriers, generation-recombination in the depletion region and tunneling between conduction and valence band [100]. The variance of the shot noise including the contributions of the average photocurrent and dark current is expressed as [101]

$$\sigma_{\text{shot}}^2 = \langle i_{\text{shot}}^2(t)\rangle = 2\text{q}\big(I_{\text{ph}} + I_{\text{d}}\big)B_{\text{N,el}}, \tag{2.36}$$

where q denotes the electron charge. If the PD is connected to a subsequent element with the reference resistor, the corresponding shot noise power is given by

$$N_{\text{el,shot}} = \langle i_{\text{shot}}^2(t)\rangle \cdot R_{\text{ref}} = 2\text{q}\big(I_{\text{ph}} + I_{\text{d}}\big)B_{\text{N,el}}R_{\text{ref}}. \tag{2.37}$$

Relative Intensity Noise

As already discussed in chapter 2.1, a laser is affected by random fluctuations of the output intensity referred to as relative intensity noise. The origin of RIN results from spontaneous emission and from random electron-hole pair recombination [102]. Often, the RIN is statistically described with a power spectral density which depends on the noise frequency. The unit of this RIN power spectral density is Hz^{-1}, but typically, it is characterized in a logarithmic scale and therefore expressed as dB/Hz. Although it is dependent on frequency, for a small bandwidth it can be assumed to be constant [103]. Thus, the variance of the RIN can be expressed as [104]

$$\sigma_{\text{RIN}}^2 = \langle i_{\text{RIN}}^2(t)\rangle = 10^{\frac{RIN^{\text{dB}}}{10}} \cdot I_{\text{ph}}^2 \cdot B_{\text{N,el}}. \tag{2.38}$$

Here, RIN^{dB} is expressed in dB/Hz. This leads to the following expression of the noise power due to RIN after o/e-conversion:

$$N_{\text{el,RIN}} = \langle i_{\text{RIN}}^2(t)\rangle \cdot R_{\text{ref}} = 10^{\frac{RIN^{\text{dB}}}{10}} \cdot I_{\text{ph}}^2 \cdot B_{\text{N,el}} \cdot R_{\text{ref}}. \tag{2.39}$$

It is obvious that shot noise and RIN are dependent on the photocurrent while the thermal noise is independent.

Amplified Spontaneous Emission Noise

If an optical amplifier is introduced in an MWP link, additional noise will be added. The most common optical amplifier for 1.55 µm wavelength is the erbium-doped fiber amplifier (EDFA). Another one is the SOA, whose FWM characteristics for a nonlinear device are described in chapter 2.3. The outcome of such an optical amplifier is the

amplified signal, as well as amplified spontaneous emission (ASE) noise which is generated inside the amplifier itself. Assuming a linear behavior of the amplification, the optical amplifier is described by its gain G_{opt} and noise figure NF_{opt} over the entire optical noise bandwidth $B_{\mathrm{N,opt}}$ determined by the gain spectrum. Although the SOA described above is nonlinear, the ASE contribution is considered to be linear [38]. The noise figure is given by [105]

$$NF_{\mathrm{opt}} = \frac{P_{\mathrm{ASE}}}{\mathrm{h}f B_{\mathrm{N,opt}} G_{\mathrm{opt}}} + \frac{1}{G_{\mathrm{opt}}}. \tag{2.40}$$

The noise power is given by $P_{\mathrm{ASE}} = 2n_{\mathrm{sp}}\mathrm{h}f B_{\mathrm{N,opt}}\left(G_{\mathrm{opt}} - 1\right)$, where $\mathrm{h}f$ is the photon energy and n_{sp} is the population inversion parameter. Assuming that the gain G_{opt} of the amplifier is >>1, (2.40) reduces to [106]

$$NF_{\mathrm{opt}} = \frac{2\rho_{\mathrm{sp}}}{G_{\mathrm{opt}}\mathrm{h}f}, \tag{2.41}$$

where ρ_{sp} denotes the spontaneous power density. If the optical signal from the output of the optical amplifier is now inserted in a PD, noise beating products will be created. These mainly include beating between the signal and the ASE noise (sig-ASE), as well as the ASE noise beating with itself (ASE-ASE). The noise powers of these beating products with respect to the corresponding variances can be expressed as [107]

$$N_{\mathrm{el,sig-ASE}} = \sigma^2_{\mathrm{sig-ASE}} \cdot R_{\mathrm{ref}} = 2\left(R \cdot G_{\mathrm{opt}}\right)^2 P_{\mathrm{opt,in}} NF_{\mathrm{opt}} B_{\mathrm{N,el}} \mathrm{h}f \cdot R_{\mathrm{ref}} \tag{2.42}$$

$$N_{\mathrm{el,ASE-ASE}} = \sigma^2_{\mathrm{ASE-ASE}} \cdot R_{\mathrm{ref}} = \left(R \cdot G_{\mathrm{opt}} NF_{\mathrm{opt}} \mathrm{h}f\right)^2 B_{\mathrm{N,opt}} B_{\mathrm{N,el}} \cdot R_{\mathrm{ref}}, \tag{2.43}$$

where R is the responsivity of the PD and $P_{\mathrm{opt,in}}$ is the average optical input power. Due to the fact that the ASE-ASE noise power is a function of the optical bandwidth, the noise contribution can be drastically reduced by using e.g. narrowband optical filters.

The requirements for many applications concerning noise are very stringent. It is desired that the generated RF signal is significantly higher than the noise, i.e. that the SNR has to

be high. Assuming an amplified analog optical link, the SNR including all noise contributions described above becomes [108]

$$SNR = \frac{m^2\left(R \cdot P_{\mathrm{opt,in}} G_{\mathrm{opt}}\right)^2}{2\left(\sigma_{\mathrm{th}}^2 + \sigma_{\mathrm{shot}}^2 + \sigma_{\mathrm{RIN}}^2 + \sigma_{\mathrm{sig-ASE}}^2 + \sigma_{\mathrm{ASE-ASE}}^2\right)}, \tag{2.44}$$

with m as the modulation index. Since the signal is amplified, the photocurrent I_{ph} in equation (2.36) and (2.38) can be replaced by $R \cdot P_{\mathrm{opt,in}} G_{\mathrm{opt}}$. As the SNR is typically given in units of dB, equation (2.44) becomes

$$\begin{aligned} SNR_{\mathrm{dB}} &= 10 \cdot \log_{10}\left(\frac{m^2\left(R \cdot P_{\mathrm{opt,in}} G_{\mathrm{opt}}\right)^2}{2\left(\sigma_{\mathrm{th}}^2 + \sigma_{\mathrm{shot}}^2 + \sigma_{\mathrm{RIN}}^2 + \sigma_{\mathrm{sig-ASE}}^2 + \sigma_{\mathrm{ASE-ASE}}^2\right)}\right) \\ &= P_{\mathrm{el,out,dB}} - N_{\mathrm{el,out,dB}}, \end{aligned} \tag{2.45}$$

where $P_{\mathrm{el,out,dB}}$ and $N_{\mathrm{el,out,dB}}$ are the electrical signal output power and the summation of all noise powers in dB, respectively.

Phase Noise

Phase noise is a term used to describe random time-dependent phase fluctuations of a signal. The phase noise of a frequency synthesizer or oscillator plays a critical role in the system performance if it is used as an RF carrier or a local oscillator (LO) signal. If the phase noise is higher than desired, the overall performance of the system can be degraded e.g. by reducing the SNR, reducing the adjacent channel rejection and increasing the adjacent channel power. An ideal oscillator delivers a pure sinusoidal signal without any fluctuations in time domain representing an infinite thin line in frequency domain which is mathematically described as a Dirac delta function. In a real frequency synthesizer, however, random time-dependent amplitude $A(t)$ and phase $\phi(t)$ fluctuations occur [109]. Thus, the output signal becomes

$$V(t) = V_0[1 + A(t)] \cdot \cos[2\pi f_0 t + \phi(t)]. \tag{2.46}$$

As for most quality sources the presence of limiting mechanisms results in very small amplitude fluctuations [110] and furthermore, due to the fact that this chapter just deals

with the phase noise representation of signals, the amplitude noise will be neglected in the following. Figure 2.7 shows the output spectrum of a real synthesizer containing phase noise in time-domain [110].

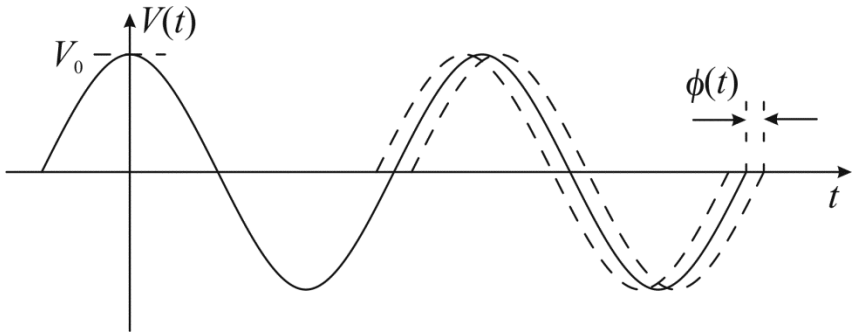

Figure 2.7: Output spectrum of a real synthesizer in time domain.

Typically, the phase term consists of two types of fluctuations [111]. The first type, described by the discrete signals, is called “spurious” and appears as distinct components. The second type appears as random phase fluctuations and is referred to as phase noise. Figure 2.8 shows the output spectrum of a real synthesizer in frequency domain [111].

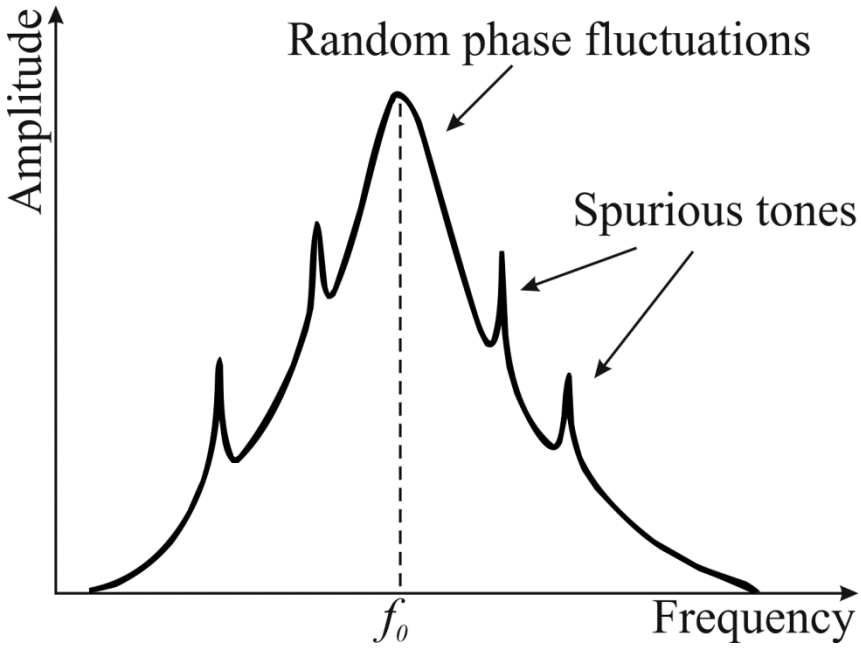

Figure 2.8: Output spectrum of a real synthesizer in frequency domain.

The phase noise of an oscillator is specified as the ratio between the noise power in a bandwidth of 1 Hz at any frequency offset from the carrier to the power of the carrier (see

Figure 2.9), [112]. It is typically quantified as the single-sideband (SSB) phase noise with the unit dBc/Hz. The SSB phase noise can therefore be expressed as

$$\mathcal{L}(f) = 10 \cdot \log\left(\frac{P_{\mathrm{SSB}}(f_0 + \Delta f, 1\ \mathrm{Hz})}{P_{\mathrm{carrier}}}\right), \tag{2.47}$$

where $P_{\mathrm{SSB}}(f_0 + \Delta f, 1\ \mathrm{Hz})$ is the noise power in a 1 Hz bandwidth at an offset frequency Δf from the carrier frequency f_0, and P_{carrier} is the total signal power at frequency f_0.

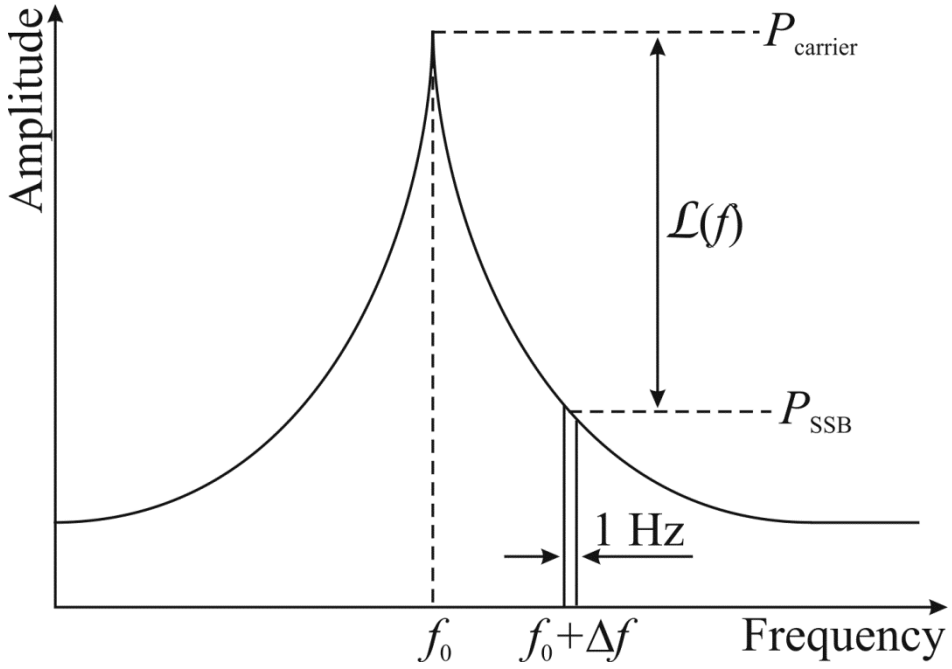

Figure 2.9: Definition of SSB phase noise to carrier ratio.

Phase noise limits the ability to detect signals in a system as it has a strong impact on the receiver front ends SNR and thus, also on the bit-error-rate in digital applications. One example for this limitation is called reciprocal mixing [113]. Assuming two RF signals are present, one desired signal f_0 with a small amplitude and one undesired adjacent signal f_{n} with a large amplitude as shown in Figure 2.10. Furthermore, an LO signal with a noisy spectrum is used for down-conversion. Then, the reciprocal noise due to the strong adjacent signal's noise will dominate the SNR at IF making it difficult to detect the desired signal.

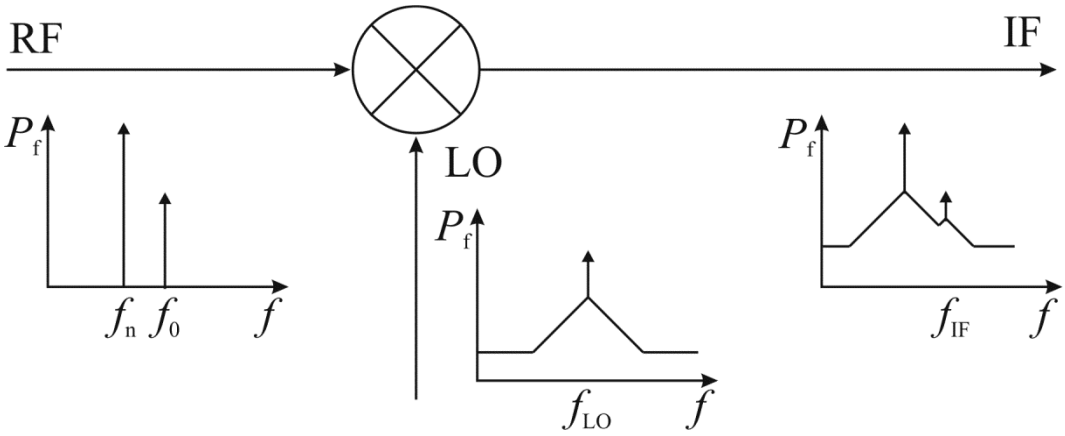

Figure 2.10: Effect of reciprocal mixing on the receiver's performance.

Another example is referred to as phase impairment [114]. In a coherent transmission system, where a coherent receiver is used to detect a phase encoded signal like e.g. a quadrature phase shift keying (QPSK) signal, an LO signal is needed to gain the phase information of the received signal. However, the phase noise of the LO signal, which appears as phase error in the phase domain, adds a random error to the received signal's phase. This results in position shifts of constellation points which means a phase error between the actual received signal and the ideal signal which causes a misdetection of the signal if the phase error and thus the phase noise is too large.

As this thesis deals with the optical generation of MW signals, the following analysis is based on beating two optical modes inside a PD which converts the two-mode optical signal into an electrical signal (optical heterodyning – see chapter 3.1). The resulting heterodyne beat, neglecting the amplitude fluctuations, becomes

$$V(t) = V_0 \cdot \cos[2\pi(f_1 - f_2)t + \Delta\phi(t)], \tag{2.48}$$

where V_0 represents the amplitude, f_1 and f_2 are the optical frequencies and $\Delta\phi(t)$ is a random process that represents the overall electrical phase noise given by

$$\Delta\phi(t) = \phi_1(t) - \phi_2(t). \tag{2.49}$$

It is obvious that the resulting electrical phase noise implies the optical phase noise contributions $\phi_1(t)$ and $\phi_2(t)$ of the two optical modes. Assuming, the two optical modes

are from two free-running lasers, the optical phase noise contributions $\phi_1(t)$ and $\phi_2(t)$ are uncorrelated. As a consequence, the overall electrical phase noise of the beat signal is much higher compared to the case if the optical phase noise contributions are correlated. This can be easily verified with the delay line method [115], [116] and [117] described in the following. For this method, just one laser with frequency f_0 is used for the generation of the RF beat signal. The optical signal is split into two paths with one path frequency shifted at an amount of δf from f_0 to generate a difference frequency between both paths. Furthermore, the modulated path is also delayed (τ) to adjust the correlation. Then, both paths are combined and the resulting optical signal beats at a PD. Figure 2.11 shows the principle setup for the delay line method [117].

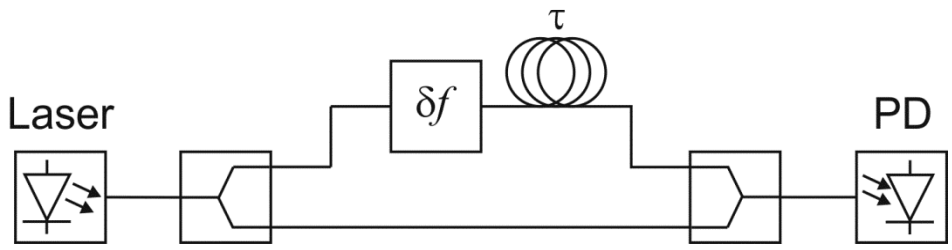

Figure 2.11: Principle setup for the delay line method.

The resulting heterodyne beat at the output of the PD is given by

$$V(t) = V_0 \cdot \cos[2\pi\delta f t + 2\pi(f_0 + \delta f)\tau + \Delta\phi(t,\tau)], \tag{2.50}$$

with the representation of the phase noise as

$$\Delta\phi(t,\tau) = \phi_0(t+\tau) - \phi_0(t). \tag{2.51}$$

Under the assumption that the frequency shifter does not have any influence on the phase noise, the resulting overall phase noise is just affected by the laser's phase noise ϕ_0.

For characterizing the phase noise, the phase noise power spectral density (PSD) as a function of Fourier frequency f has to be introduced. Several measurement techniques exist to obtain the PSD. Most of them require a reference source with lower phase noise than that of the device under test. However, all phase noise measurements in this work have been performed using an electrical spectrum analyzer (ESA) which makes the use of

a reference oscillator unnecessary. Thus, the following analysis is based on this technique. A detailed analysis for other techniques can be found e.g. in [109], [118] and [119].

Turning $\Delta\phi(t,\tau)$ and $\phi_0(t)$ into their respective Fourier transforms, the phase noise representation of (2.51) becomes [116]

$$\Delta\phi(f) = H_\phi(f) \cdot \phi_0(f), \tag{2.52}$$

with the transfer function $H_\phi(f) = 1 - \mathrm{e}^{-\mathrm{j}2\pi f\tau}$. The corresponding phase noise PSD of the beat note is thus equal to [115], [116]

$$S_\phi(f) = \left|H_\phi(f)\right|^2 \cdot S_{\phi 0}(f), \tag{2.53}$$

where $S_{\phi 0}(f)$ is the PSD of the laser phase noise and

$$\left|H_\phi(f)\right|^2 = 4 \cdot \sin^2(\pi f\tau). \tag{2.54}$$

From (2.53) and (2.54) it becomes clear that if the delay is chosen that $\sin^2(\pi f\tau) \approx 1$ (uncorrelated), the overall phase noise PSD is much higher compared to the case that $\sin^2(\pi f\tau) \ll 1$ (correlated).

Due to the fact that an ESA measures not only the phase noise but also amplitude and frequency fluctuations, $S_\phi(f)$ is a quantity that cannot be measured directly. Thus, those measurements are so called “all-noise” measurements. However, as already mentioned above, amplitude fluctuations are typically very small such that they can be neglected. Frequency fluctuations can be easily described in terms of its PSD as they are directly related to the phase noise PSD by [116]

$$S_\mathrm{y}(f) = \frac{f^2}{\nu_0^2} \cdot S_{\phi 0}(f), \tag{2.55}$$

where ν_0^2 is the carrier frequency. Combining equations (2.53) and (2.55), the expression for the phase noise PSD dependent on $S_\mathrm{y}(f)$ becomes

$$S_{\phi}(f) = \frac{\nu_0^2}{f^2} \cdot 4\sin^2(\pi f \tau) \cdot S_{\mathrm{y}}(f). \tag{2.56}$$

A common scheme to generate two correlated optical modes from one laser source is based on external modulation using an electro-optical modulator in conjunction with an electrical reference LO (see chapter 2.2). Here, the resulting phase noise of the beat signal is mainly determined by the phase noise of the electrical LO signal. A detailed analysis for the phase noise representation of the generated MW signal using external modulation can be found in [120].

As already described above, the phase noise is typically quantified as the SSB phase noise $\mathcal{L}(f)$. The SSB phase noise $\mathcal{L}(f)$ and the PSD $S_{\phi}(f)$ are equivalent since $\mathcal{L}(f)$, given in dBc/Hz, is defined by the IEEE standard 1139 as [121]

$$\mathcal{L}(f) = \frac{1}{2} \cdot S_{\phi}(f). \tag{2.57}$$

For several applications, MW signals with frequencies exceeding several tens of GHz which offer low phase noise performance are of great interest. Thus, frequency multiplication schemes are widely used to obtain such high frequency low phase noise MW signals. Typically, electronic frequency multipliers are used. However, frequency multiplication is not only possible in the electrical domain but also in the optical domain using electro-optic modulators. Imagine an external modulation scheme where an MZM is used to obtain a DSB-CS signal. After photo detection, the generated RF signal has a frequency twice ($N = 2$) that of the reference LO used to drive the MZM, where N denotes the multiplication factor. As a consequence, the phase noise of the generated signal is also affected. The phase noise $\mathcal{L}_{\mathrm{out}}(f)$ given in dBc/Hz of the generated signal is then

$$\mathcal{L}_{\mathrm{out}}(f) = \mathcal{L}_{\mathrm{LO}}(f) + 20 \cdot \log(N), \tag{2.58}$$

where $\mathcal{L}_{\mathrm{LO}}(f)$ represents the phase noise of the LO given in dBc/Hz. This is exactly the same relation as it was identified for electronic frequency multipliers [122].

To get a better knowledge of how the different spectra representing the phase fluctuations look like, it is useful to introduce the so called power-law model. The model for $S_\phi(f)$ is given as [123]

$$S_\phi(f) = \sum_{i=0}^{-4} b_i f^i, \tag{2.59}$$

where b_i is a coefficient representing the noise level and f^i represents a straight line of slope i, i.e. the slope is i times 10 dB/decade, representing the characteristic of the noise. The following table gives an overview of the noise types and the spectral density.

Table 2.1: The power-law model for noise types and spectral density [123].

Noise type	$S_\phi(f)$	slope
white ϕ	b_0	0
flicker ϕ	$b_{-1}f^{-1}$	10 dB/decade
white f	$b_{-2}f^{-2}$	20 dB/decade
flicker f	$b_{-3}f^{-3}$	30 dB/decade
random walk f	$b_{-4}f^{-4}$	40 dB/decade

As the different noise types have different physical origins, not always all noise terms are present in a system. The physical origins of the different noise types are described in the following [109]. The physical origin of white noise is related to thermal noise (temperature). While it is internal to the oscillator loop for white frequency noise (white f), white phase noise (white ϕ) usually arises due to additive white noise of external sources. Flicker ϕ noise is a result of external active components like e.g. amplifiers, while flicker f noise is related to resonator noise and active components inside the oscillator. The last contribution is random walk frequency noise (random walk f). Its physical origin is related to environmental factors such as mechanical shocks, vibration, temperature, etc. Figure 2.12 shows the schematic of the power-law model for $S_\phi(f)$ [116], [123].

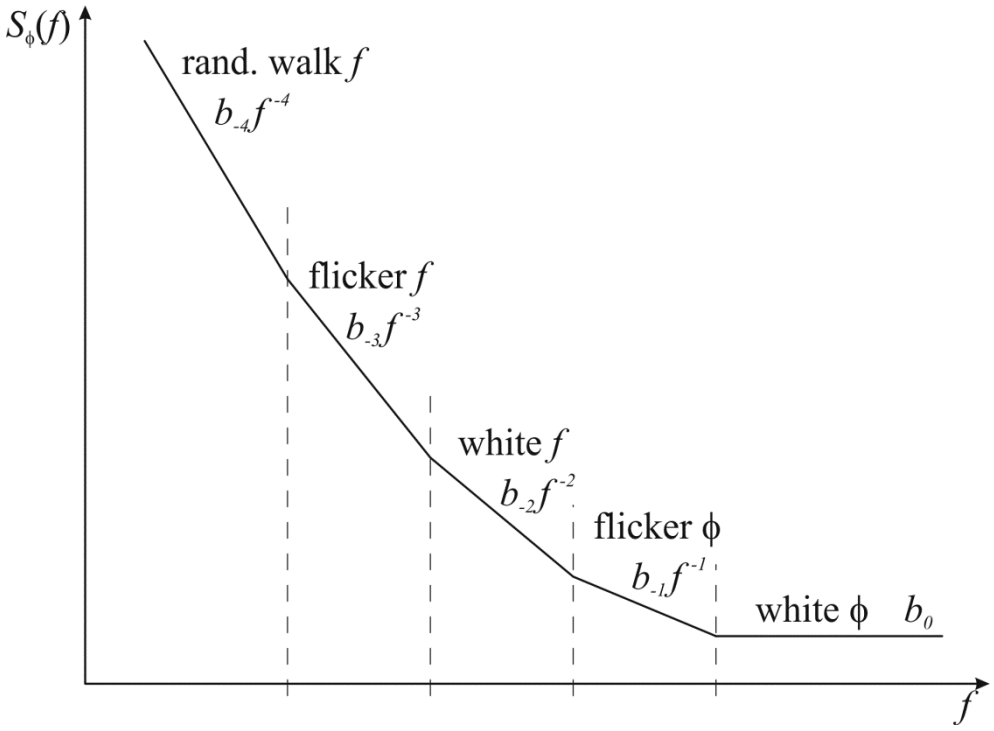

Figure 2.12: Schematic of the power-law model for $S_\phi(f)$.

3 Photonic Micro- and Millimeter-Wave Signal Generation

One general aim of this work was the development of photonic synthesizer concepts enabling the generation of low phase noise MW signals with the capability to tune the frequency over a wide range. An attractive solution for achieving such a wide frequency tuning range is based on optical heterodyning in which two optical modes of different wavelengths beat in a photodetector. For generating those two optical modes, today different approaches like e.g. dual-mode lasers or dual-frequency lasers. Using a solid-state dual-frequency laser, low phase noise optical heterodyne MW signal generation of up to 20 GHz was achieved [6]. Phase noise levels at 100 kHz offset from a 2 GHz carrier of about -90 dBc/Hz and -120 dBc/Hz for the free-running and the optically phase locked solid-state dual-frequency have been measured, respectively [7], [8]. However, the maximum operating frequency was limited to just about 20 GHz. In order to improve the frequency tuning range an approach using a multi-section gain-coupled DFB laser was presented in [9]. Although, a wide frequency tuning range of 46.5-322 GHz was achieved, the generated MW signal could only be tuned in steps with a frequency resolution of about 35 GHz as the laser needed to be locked to an optical comb. In this work, innovative approaches based on optical heterodyning using two independent free-running lasers, in which at least one laser in tunable in wavelength, will be investigated and reported. The generated MW signal at an advanced photodetector can be tuned in a continuous manner with a frequency resolution just defined by the wavelength tuning resolution of the tunable laser(s). Experiments using two different output port configurations, one for achieving an ultra-broadband tuning range and another for achieving an extremely flat frequency response and high output power levels even at millimeter-wave frequencies, will be presented. Using the first configuration, MW signal generation with an ultra-broadband frequency tuning range from 30 kHz up to 110 GHz has been achieved. A total signal roll-off within this frequency range of about 6 dB and electrical output power levels up to -3.23 dBm have been measured. In order to achieve a flat frequency response and high output power levels at millimeter-wave frequencies, a limiting amplifier has been used for the second configuration. With this configuration, frequency tunable MW signal generation providing an extremely flat frequency response within W-band and output power levels as high as -4 dBm (1 dB compression point) at a frequency of 110 GHz has been achieved. However, due to the fact that the lasers are free-running, i.e. the optical phase noise contributions of the lasers are not correlated, the overall electrical phase noise of the

generated MW signal is much higher compared to the correlated case (see chapter 2.6). Thus, in order to achieve low phase noise operation, the phase terms of the optical modes have to be locked against each other. Different locking techniques like optical injection locking and optical phase lock loops, which will be analyzed shortly in this work, are able to lock these terms. However, these locking techniques are complicated and furthermore, the frequency tuning range is limited [124]-[128].

An option to overcome the need for complicated locking techniques is to use external optical modulation. As the optical modes are generated from only one laser source, low phase noise MW signals with a wide frequency tuning range can be generated. In [10], an optical phase modulator in conjunction with a fixed optical notch filter has shown the capability to generate continuously frequency tunable MW signals from 37.6-50 GHz by using an electrical drive signal tuned from 18.8-25 GHz. Although the phase noise was not measured in this work, the linewidth of the generated MW signals was below 5 Hz. However, signals above 50 GHz could not be measured but were seen in the optical domain. Furthermore, the output power at 50 GHz was seriously limited to be less than -30 dBm. Nevertheless, it can be seen that the frequency of the generated MW signal is the double frequency of the electrical drive signal provided by the LO or electrical synthesizer. In this work, an innovative approach based on double-sideband modulation with carrier suppression in an external MZM without the need for any filtering techniques will be investigated and reported. Using this scheme, continuously frequency tunable MW signals from 20 MHz up to 110 GHz by using an electrical synthesizer tuned from 10 MHz-55 GHz have been generated. At a frequency of 100 GHz, an electrical output power of -33 dBm without any electrical amplification has been achieved. Furthermore, phase noise measurements have been performed. At a sample frequency of 100 GHz a phase noise level of better than -70 dBc/Hz at 10 kHz offset has been measured.

As already described in chapter 2.6, the phase noise of the generated MW signal using external modulation is mainly determined by the phase noise of the LO plus a term depending on the multiplication factor, i.e. the lower the phase noise of the LO the lower the phase noise of the generated MW signal. For an LO, normally ultra-low phase noise and low frequency crystal or quartz oscillators build the basis for generating high frequencies via several complex mixing and multiplications stages. As a consequence, the phase noise of a high frequency LO requiring more multiplication and mixing stages than a

lower frequency LO is also much higher. Thus, another aim of this work was to investigate possibilities that allow an efficient frequency multiplication in the optical domain with an as high as possible multiplication factor such that low frequency LOs can be used (see PHOMIGEN project). As already described above, double-sideband modulation with carrier suppression using an external MZM already doubles the frequency by optical means. To further increase the optical multiplication factor, an approach using two cascaded MZM will be analyzed and presented in this work. It will be experimentally shown that such a scheme is in principle able to achieve a four times optical multiplication. However, this approach is very complex and furthermore, very high electrical or optical gain is needed to achieve a high conversion efficiency. A promising approach to overcome these issues is to use the four-wave mixing effect in a saturated SOA. In [11], an MW signal with a frequency of 42 GHz from a 7 GHz electrical reference oscillator was generated by using an MZM with a subsequent SOA, i.e. a six times optical multiplication was achieved. The phase noise of the generated 42 GHz signal was measured to be -75 dBc/Hz at 1.6 kHz offset. An improvement of the multiplication factor based on the use of an external MZM, driven at high RF input powers to create higher harmonics, in conjunction with a highly nonlinear SOA, to achieve four-wave mixing, will be presented in this work. With this scheme, a 32 GHz MW signal has been generated from a 4 GHz LO reference, i.e. an optical multiplication factor of eight times has been achieved. Furthermore, phase noise measurements have been performed showing phase noise levels of -78 dBc/Hz and -96 dBc/Hz at 10 kHz offset from the generated 32 GHz and the 4 GHz LO signal, respectively. This means that the phase noise of the generated MW signal increases by 18 dB verifying that the same relation as identified for electronic frequency multipliers is valid (see chapter 2.6).

3.1 Photonic Signal Generation using Optical Heterodyning

This chapter will deal with photonic MW signal generation based on optical heterodyning. In chapter 3.1.1, the basic principle of operation using a two-mode optical signal beating in a PD is analyzed. Next, possibilities for achieving wideband as well as broadband optical MW signal generation are discussed and corresponding experimental results are presented in chapter 3.1.2. Finally, different techniques for locking the optical modes are analyzed shortly in chapter 3.1.3.

3.1.1 Optical Heterodyning Technique

A straightforward approach for generating a two-mode optical signal is to use two independent free-running laser sources as shown in Figure 3.1. A polarization controller (PC) is used to ensure that both optical modes are polarized in the same direction. By combining both optical modes using a standard 3 dB coupler, the optical signal beats in a PD which converts the two-mode optical signal into an electrical signal MW signal. In this case, the generated electrical MW signal has a frequency equal to the difference frequency between the two optical modes. In order to achieve continuous frequency tuning, one laser source (LS) is fixed in wavelength while the other one is a tunable laser source (TLS).

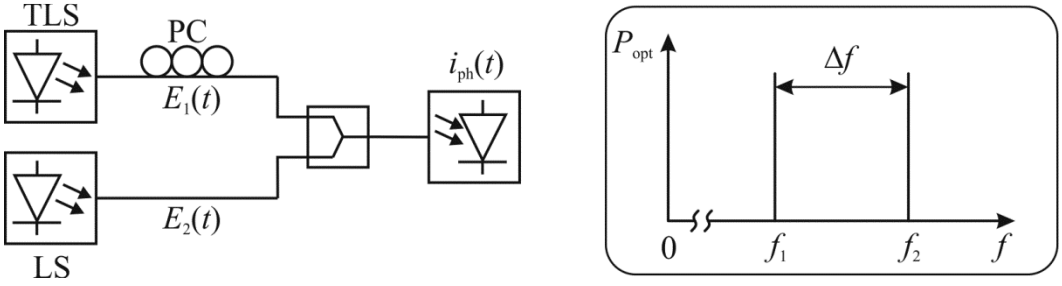

Figure 3.1: Optical heterodyning of two optical modes to generate an MW signal.

Assuming that the electric fields of the two linearly polarized optical modes from the laser sources are given by

$$E_1(t) = E_{01} \cdot \exp[\mathrm{j}(\omega_1 t + \phi_1(t))] \tag{3.1}$$

$$E_2(t) = E_{02} \cdot \exp\big[\mathrm{j}\big(\omega_2 t + \phi_2(t)\big)\big], \tag{3.2}$$

where E_{01} and E_{02} are the amplitudes, ω_1 and ω_2 are the angular frequencies ($\omega_{1,2} = 2\pi f_{1,2}$), and $\phi_1(t)$ and $\phi_2(t)$ are the phase terms. For simplification issues, the phase information as well as losses like e.g. the losses resulting from the 3 dB coupler will be neglected in the following. Thus, by combining both optical modes and taking into account the relationship between the photocurrent and the intensity as can be obtained from (2.33), the intensity becomes [129]

$$\begin{aligned} |E_{\mathrm{tot}}(t)|^2 &= [E_1(t) + E_2(t)] \cdot [E_1(t) + E_2(t)]^* \\ &= E_{01}^2 + E_{02}^2 + 2\cos(\varphi_{\mathrm{Pol}}) E_{01} E_{02} \cos[(\omega_1 - \omega_2)t], \end{aligned} \tag{3.3}$$

where * denotes the conjugate complex operation and φ_{Pol} is the angle between the polarized directions of the two optical modes. As the wavelengths from both lasers are typically in the range around 1.55 µm, it is obvious that the PD has to be sensitive for these wavelengths (see chapter 2.5). The difference frequency between the optical modes $(\omega_1 - \omega_2)$ will be detected if this frequency is within the bandwidth of the PD. As already stated above, also the polarization has to be adjusted to ensure the same polarization. If the angle between the polarized directions of the optical modes is e.g. 90°, the term $\cos(\varphi_{\mathrm{Pol}})$ in equation (3.3) becomes "0". Thus, also the generated MW signal becomes "0". In the following it is assumed that the polarization is adjusted to achieve maximum MW signals, i.e. the term $\cos(\varphi_{\mathrm{Pol}})$ becomes "1". Considering the relation between the intensity and power from (2.33), the total optical power which is introduced in the PD is given as

$$P_{\mathrm{tot}}(t) = P_{01} + P_{02} + 2\sqrt{P_{01}P_{02}}\cos[(\omega_1 - \omega_2)t]. \tag{3.4}$$

Thus, the photocurrent at the output of a PD becomes

$$i_{\mathrm{ph}}(t) = R \cdot \left\{P_{01} + P_{02} + 2\sqrt{P_{01}P_{02}}\cos[(\omega_1 - \omega_2)t]\right\}, \tag{3.5}$$

where R denotes the responsivity of the PD. As can be seen from (3.5), an electrical signal with a frequency equal to the difference frequency of the two optical modes is generated. The wavelength tuning range of a tunable laser is typically in the range of tens of nanometers. Taken into account that at around 1.55 µm wavelength a wavelength difference of just 0.8 nm between both optical modes is equal to a difference frequency of about 100 GHz, an extremely wide tuning range can be achieved. Thus, the only limiting factor for generating wide tunable MW signals using the heterodyne technique described above is the bandwidth of the PD.

3.1.2 Wideband and broadband optical MW signal generation

Using a special broadband high power pin PD (Figure 3.2), wideband (W-band) and broadband (30 kHz to 110 GHz) optical MW signal generation can be obtained using the optical heterodyning technique [I]. The PD is equipped with an integrated bias network, a tapered passive optical waveguide suitable for standard cleaved fiber coupling and a 50 Ω matched coplanar output.

Figure 3.2: Photograph of the developed PD (u^2t Photonics), featuring a passive optical waveguide and an integrated bias network.

At 1.55 µm wavelength, the PD exhibits a responsivity of about 0.3 A/W when using cleaved fiber coupling. Measurements have shown that the photocurrent increases linearly in a wide range with increasing optical input power (see Figure 3.3). Furthermore, with increasing reverse bias voltage, the saturation of the photocurrent moves towards higher optical input powers which can be attributed to the internal field screening [130]. At a reverse bias of 3 V, no saturation up to about 35 mW of optical input power is observed. For safety reasons, photocurrents higher than 12 mA were not applied.

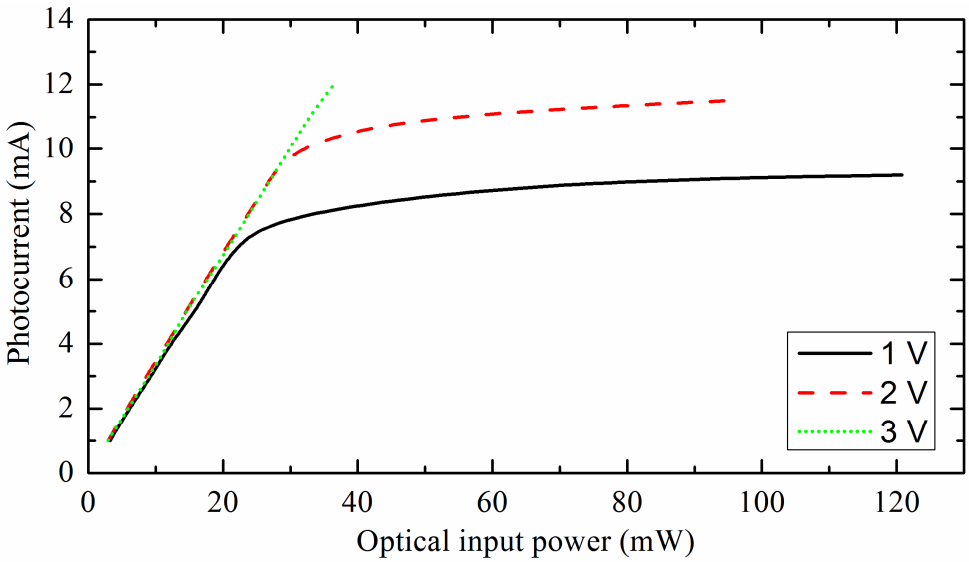

Figure 3.3: DC response of the employed pin waveguide PD at different reverse bias voltages.

In Figure 3.4, the photonic MW synthesizer setup using the optical heterodyning technique is shown. For optical MW signal generation, light from a TLS with frequency f_1 and light from a fixed frequency laser source (LS) with frequency f_2 are combined by using a standard 3 dB coupler. By adjusting the frequency of the TLS, both laser modes are separated with a difference frequency of Δf. To ensure an identical polarization state of the

two constituent laser sources, a PC is applied after the TLS. The dual-mode signal is amplified by an EDFA and further filtered by an optical bandpass filter (OBPF) to reduce the contribution of ASE noise from the EDFA. After transmission via a standard SMF, the photonic MW signal is o/e converted via the broadband high power pin PD.

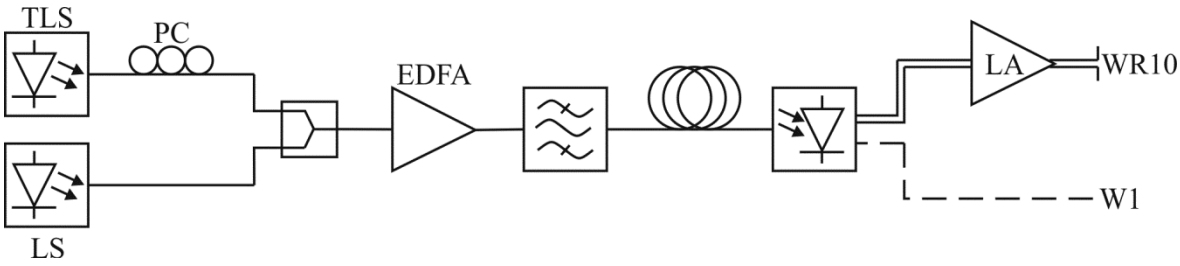

Figure 3.4: Photonic MW synthesizer using a dual-laser approach. The output of the PD is either coupled to a limiting W-band amplifier with WR10 output port or to a coaxial W1 output port.

The setup consists of two different output port configurations depending on the application field of the photonic MW synthesizer. The first setup features a coaxial W1 output port (Anritsu) which is based on the 1 mm coaxial connector according to IEEE Std. 287 [131]. This is the only coaxial standard covering a frequency range from DC to 110 GHz. With this configuration MW signal generation providing continuously frequency tuning within the whole frequency range can be achieved as used e.g. for broadband test and measurement applications.

For characterizing the photonic MW synthesizer, the frequency response was measured via an ESA from Hewlett-Packard (HP 8565E). Up to 50 GHz, measurements were carried out directly with the internal mixers of the ESA. Measurements above 50 GHz were carried out by using an external V-band mixer to cover the frequency range from 50 up to 75 GHz and an external W-band mixer for the frequency range of 75-110 GHz. As can be seen from Figure 3.5, a flat and wideband frequency response was achieved with a total signal roll-off of about 6 dB and electrical output power levels up to -3.23 dBm. Considering a frequency range from 20 GHz up to 110 GHz, the total signal roll-off is below 3 dB.

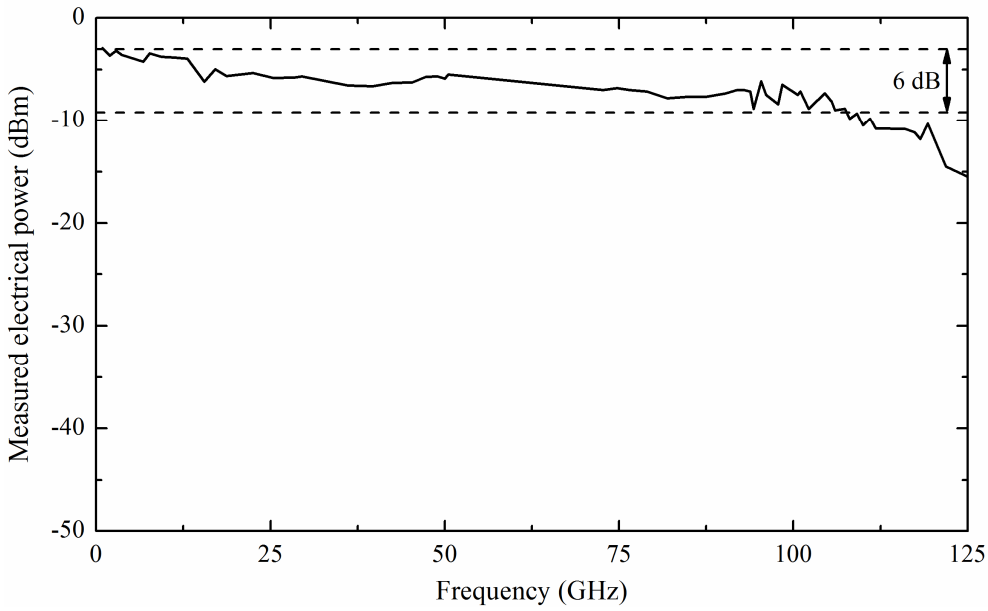

Figure 3.5: Wideband frequency response of the W1 coupled photonic MW synthesizer. The photocurrent was set at 10 mA.

It should be noted that this photonic MW synthesizer exceeds the frequency tuning range of commercially available electronic synthesizers (e.g. Agilent E8257D, DC-67 GHz) where such a high tuning range can only be achieved using additional external multiplier stages.

For several applications like e.g. communications, however, broadband operation is not required as so-called frequency bands are defined allowing to operate only inside a given bandwidth around a given frequency. Here, the focus is typically laid on a very flat frequency response inside the frequency band of interest as well as high RF output powers. Furthermore, the possibility to adjust the RF output power is also often desired. Thus, with the aim to reach these specifications even at millimeter-wave frequencies, in the second configuration a WR10 rectangular waveguide output comprising an additional amplifier for W-band operation (75 to 110 GHz) is deployed.

For this output port configuration, a constructed limiting two-stage amplifier (LA) with an inter-stage isolator and a noise figure of 4.5 dB is used, allowing an increased RF output power, as well as a flattened frequency response. As can be seen from Figure 3.6, the amplifier's gain is inversely proportional to the MW input power inside a range from about 0 dBm down to -35 dBm. For input powers below -35 dBm, first the gain reaches a

maximum (saturation) before it, by further decreasing the input power, also strongly decreases. Assuming a 100 GHz MW signal with an RF power of -10 dBm is introduced to the LA, the gain becomes about 8 dB resulting in an RF output power of -2 dBm. If now the RF input power will be decreased to be -20 dBm, the gain of the LA becomes about 18 dB also resulting in an RF output power of -2 dBm. Thus, fluctuations of the RF input power between -35 dBm and 0 dBm can be easily compensated.

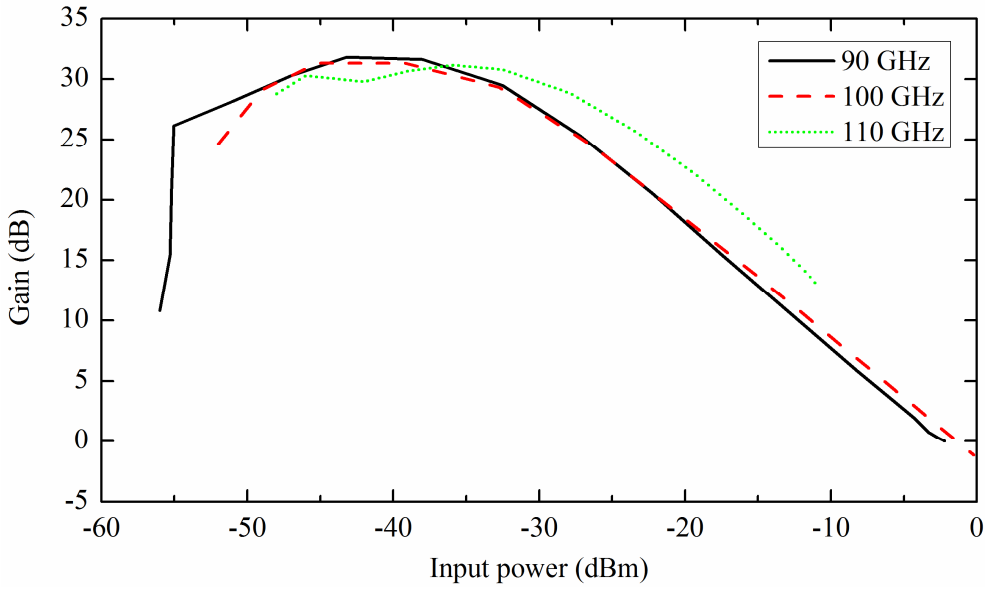

Figure 3.6: Millimeter-wave gain of the constructed limiting amplifier versus input power at different frequencies.

Although the gain characteristic is slightly different for different frequencies, a flattened frequency response inside the whole operating range can be achieved with the LA. For measuring the frequency response of the photonic MW synthesizer, also the ESA was used in conjunction with the external W-band mixer. Figure 3.7 shows the measured frequency response of the photonic MW synthesizer. As can be seen, the frequency response is very flat, showing a low and high 3 dB cut-off frequency of about 70 GHz and 112 GHz, respectively. At frequencies lower than 69 GHz, the output power rapidly decreases, which is due to the lower cut-off frequency of the WR10 waveguide. At frequencies above 112 GHz it can be seen that the output power also rapidly drops. This can be attributed to the reduced output power of the PD (see also Figure 3.5) while at the same time, the amplifier provides a lower gain.

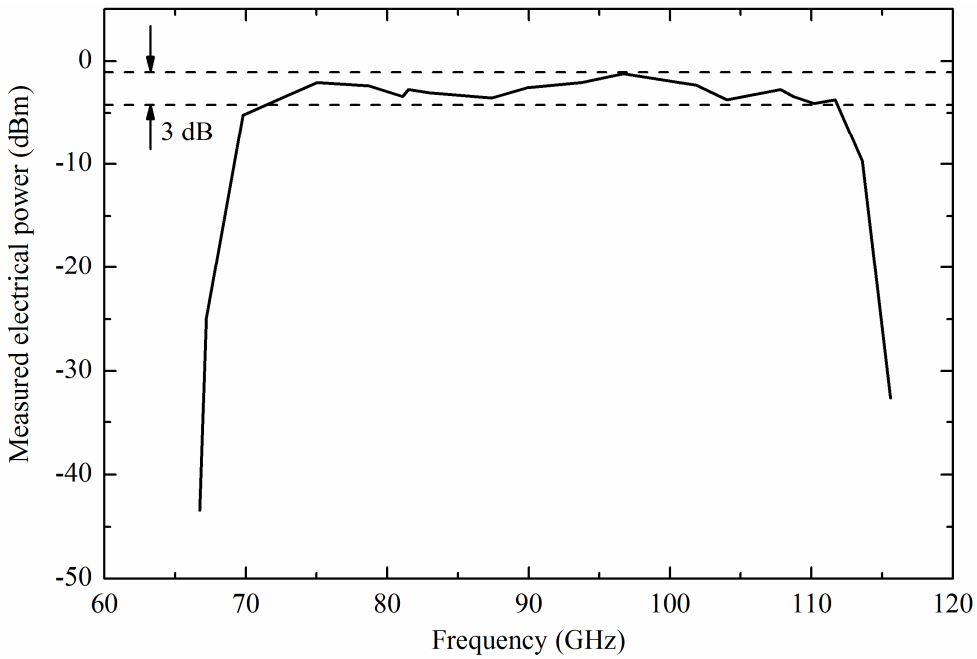

Figure 3.7: Output power of the photonic MW synthesizer vs. frequency.

However, the output power variation is just about 3 dB for the whole W-band, which makes this configuration suitable for millimeter-wave applications requiring a flat frequency response inside a given bandwidth.

In order to investigate the RF output power performance of the photonic MW synthesizer, the electrical output power as a function of the PD's photocurrent at a sample frequency of 110 GHz has been measured. As can be seen from the results shown in Figure 3.8, the saturation output power is about -2.5 dBm. The output power can be varied linearly from about -36 dBm up to the 1 dB compression point of about -4 dBm by controlling the PD's photocurrent, i.e. by controlling the optical input power. This is due to the fact that the gain of the LA is decreasing for input power levels below about -40 dBm (see Figure 3.6). If the PD is operated such that the electrical input power to the LA is below that level, an increase of the optical input power to the PD will result in an increase of the electrical input power to the LA and thus an increase of the RF output power up to the point where the gain starts to saturate. As a result, the output power of the photonic MW synthesizer can be varied quite linearly up to the 1 dB compression point. The dynamic range of the photonic MW synthesizer was found to be ~32 dB.

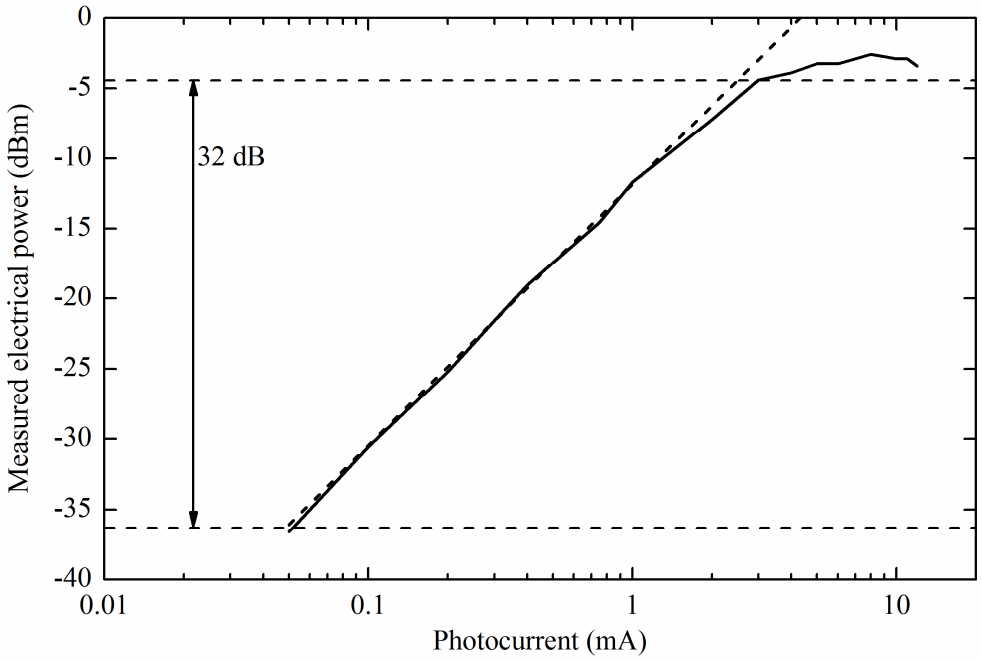

Figure 3.8: Measured electrical output power of the photonic MW synthesizer as a function of the photocurrent at a sample frequency of 110 GHz.

The results presented with the WR10 output port configuration clearly show that the requirements on a flat frequency response as well as high RF output powers can be easily achieved even at millimeter-wave frequencies (here W-band).

For many applications, also the signal quality plays a major role, i.e. a low phase noise performance of the generated MW signal is required (e.g. PHOMIGEN project). Thus, to obtain information about the signal quality of the photonic MW synthesizer, phase noise measurements were performed. The presented photonic MW synthesizer with its different output configurations exhibits a phase noise level of about -50 dBc/Hz at an offset frequency of 100 kHz within the whole spectral range which is too high for practical use. For example, the minimum phase noise at 100 kHz offset from a 100 GHz carrier required for the PHOMIGEN synthesizer is -80 dBc/Hz. The poor phase noise performance of the present photonic MW synthesizer can be attributed to the fact that both lasers were free running, i.e. the optical phase noise contributions of the two optical modes were not correlated (see also chapter 2.6) which will be transferred to the generated MW signal. Thus, for low phase noise operation these contributions have to be correlated.

3.1.3 Optical Locking Techniques

Optical locking techniques are aiming at achieving phase correlation between optical modes. Thus, using such techniques the phase noise of a generated MW signal based on optical heterodyning can be reduced. In this chapter two optical locking techniques, namely optical injection locking (OIL) and optical phase lock loop (OPLL) will be discussed. It will be shown that although MW signals with high-spectral-purity can be generated, these techniques are limited in terms of frequency tunability and are highly increasing the complexity of a photonic synthesizer concept.

Optical Injection Locking

Optical injection locking is a method for synchronizing a free-running slave laser to a stabilized master laser by optical means [124], [125]. A phase variation in the injection beam of the master laser is reproduced in the slave laser. Furthermore, it permits both, frequency locking of the slave laser to the master laser and spectral purity transfer from the master to the slave laser. As a consequence, OIL will result in a stable signal with high spectral purity.

An OIL system consisting of a frequency modulated master laser and a long-cavity slave lasers was investigated in [124]. Without optical injection, the slave laser oscillates at multimode with a mode spacing of about 35 GHz. The master laser was frequency modulated such that the frequency difference between the $+3^{rd}$ and -3^{rd} sideband was approximately 35 GHz. Thus, two modes of the slave laser were locked while the others are suppressed so that a 35 GHz MW signal was generated. Although no phase noise measurements were performed, the 3 dB spectral width of the generated beat note was smaller than the 10 Hz resolution of the used spectrum analyzer.

Experiments using two slave lasers each locked to a different mode of an optical frequency comb were performed in [125]. One of the slave lasers was a special kind of DFB laser allowing tuning the wavelength over a wide range to achieve injection locking to different modes of the frequency comb. Frequency tunable MW signal generation with a tuning range from 10 GHz to 110 GHz with a frequency tuning resolution of 10 GHz which is equivalent to the optical frequency comb spacing was shown. The measured phase noise at 10 kHz offset from each carrier up to 80 GHz was about -79 dBc/Hz. For carrier frequencies above 80 GHz, the phase noise was higher.

Although these results show the potential of the OIL technique to generate low phase noise MW signals, the frequency tuning range and/or the frequency tuning resolution is limited. Furthermore, it should be noted that stable locking is only possible inside a small region where the optical frequency of the slave laser matches the optical frequency of the master laser [125], i.e. high adjustment accuracy and frequency stable lasers are needed. As a consequence, this approach is unsuitable for the photonic synthesizer concepts to be developed in this work.

Optical Phase Lock Loop

An approach to overcome the limitations of OIL is to use an optical phase lock loop instead [126]-[128]. The basic configuration for generating the MW signal is similar to the heterodyning approach shown in Figure 3.1 but due to the OPLL, the phase of one laser is actively locked to that of the other laser [126]. In order to achieve phase locking, the phase of the generated MW signal will be compared with that of an RF reference signal by using a phase detector followed by a loop filter. As an outcome of this, an electrical signal proportional to the phase error between them is generated. This "error signal" is fed back to one laser source to control the phase by changing e.g. the injection current. This reduces the relative phase fluctuations between both lasers allowing generating low phase noise MW signals.

In [127] the generation of a continuously tunable MW signal from 6 up to 34 GHz using a complex OPLL system with two Nd:YAG lasers was shown. Two frequency synthesizer and different mixers were used to achieve frequency tuning inside three bands (6-18 GHz, 18-26.5 GHz and 26.5-34 GHz) making the system bulky and highly complex. However, although no phase noise measurements were performed, the linewidth was reported to be less than 1 mHz.

An OPLL system which aims at generating tunable MW signals up to 125 GHz was investigated in [128]. In this approach, two phase locking loops, two DFB lasers, an electro-optic phase modulator and several other optical as well as electrical components were needed making the system extremely complex and bulky. Furthermore, this system was not experimentally tested. Only experiments on a simplified system at a beat frequency of 500 MHz were performed as a proof-of-concept demonstrating the phase locking capability.

These results show that, compared to the OIL technique, MW signal generation with a continuously high frequency tuning range can be principally achieved with an OPLL. However, the major drawback is the extremely high complexity of the feedback loop as well as the fact that such a system becomes very bulky such that this technique will not be pursued.

3.2 Photonic Signal Generation Using External Modulation

An approach which is able to generate low phase noise MW signals without the need for a highly complex feedback loop on the one hand and to overcome the frequency tuning limitations from OIL on the other hand is to use external modulation. This chapter will deal with the generation of MW signals based upon external modulation using Mach-Zehnder modulators. In chapter 3.2.1, the principle of double- and single-sideband modulation is analyzed shortly. Next, double-sideband modulation with carrier suppression scheme is discussed and corresponding experimental results are presented in chapter 3.2.2. Finally, a method for achieving a high-order optical multiplication is presented in chapter 3.2.3.

3.2.1 Double- and Single-Sideband Modulation

In many analog applications where external modulation using an MZM plays a role, often the MZM is biased at its quadrature point as there the optical input signal is linearly modulated by the electrical RF signal resulting in a double-sideband signal. Here, the behavior of the MZM is quasi-linear for small amplitudes of the modulation RF signal. Nevertheless, this modulation scheme has the drawback that if the signal has to be distributed over long fiber distances, e.g. for remote applications, chromatic dispersion plays a critical role. So it can happen that the optical MW signal will be completely canceled out as already shown in chapter 2.4 of this work. Single-sideband (SSB) modulation is an attractive solution for e.g. RoF links to overcome the power penalty issue caused by CD [132]. In such a scheme, typically the carrier and one sideband are present while all other sidebands are suppressed. A common way for generating an SSB signal is to use a dual-drive (DD)-MZM where both electrodes are driven by the same RF source. Before the RF signal enters the electrical input ports of the DD-MZM it will be splitted equally into two parts, using a 3 dB RF splitter. While one of the signals enters the first RF input port directly, the other will be phase shifted by $\pi/2$ before entering the second RF

port [133]. As a result, an MW signal where the difference frequency between the carrier and the present sideband is equal to the applied RF signal can be generated. Another possibility to generate an optical SSB signal is to use filter techniques. If e.g. a fiber Bragg grating is inserted after a modulator which generates an optical DSB signal, one sideband will be removed, thus leading to an SSB signal [134].

Nevertheless, both techniques are not practical for generating high frequency MW signals as desired in this work. Assuming an MW signal with a central frequency of 100 GHz should be generated, thus, the central frequency of the needed LO source also has to be 100 GHz, which is still a challenge for electronic sources. Furthermore, the modulation bandwidth of the MZM also has to be around this frequency which is not common. The MZM used in this work provides a modulation bandwidth of around 41 GHz. As a result, the DSB-CS modulation scheme is preferred.

3.2.2 Double-Sideband Modulation with Carrier Suppression

In contrast to the DSB and SSB modulation scheme, the DSB-CS modulation scheme offers the advantage of generating high frequency MW signals using a reference oscillator with half the frequency of the generated MW signal. Furthermore, electrical reference LOs with lower frequency typically provide lower phase noise performance than high frequency LOs which result in lower phase noise of the generated MW signal. Figure 3.9 shows the configuration of an MW synthesizer using the DSB-CS modulation scheme. Here, the two optical modes are generated using an external electro-optical modulator after a laser [10], [135], [136]. The frequency of the generated MW signal is equal to the double frequency of the MW signal of the reference LO which is applied to the external Mach-Zehnder modulator [I], [N].

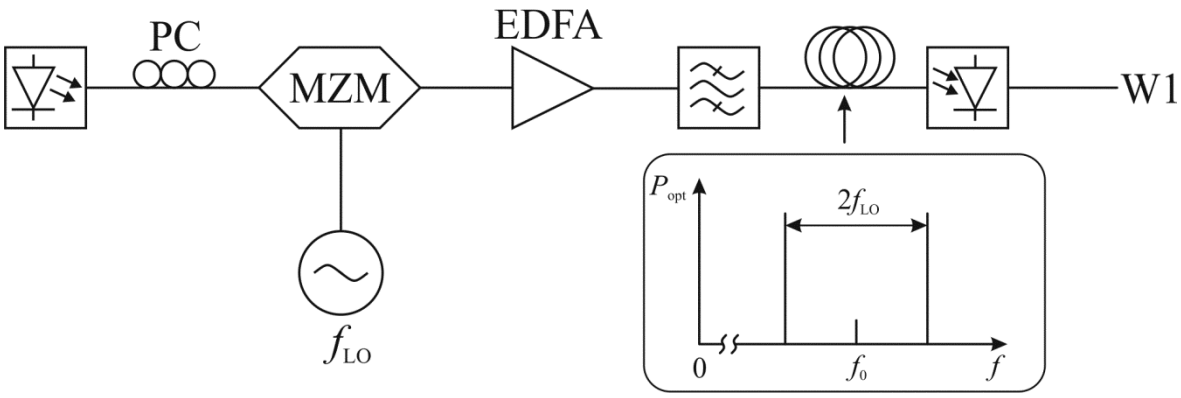

Figure 3.9: Photonic MW synthesizer using an external Mach-Zehnder modulator which is biased to double-sideband operation with carrier suppression.

For the optical MW signal generation, light from a laser source with a wavelength of 1.55 µm is modulated by a single-drive MZM with a 3 dB bandwidth of around 41 GHz. The MZM is biased at its half-wave voltage V_π to generate an optical DSB-CS signal. The modulator is driven by a tunable low phase noise sinusoidal synthesizer with a frequency range of 10 MHz up to 60 GHz. The carrier of the optical signal with frequency f_0 was suppressed by about 26 dB. After amplification of the optical signal using an EDFA with a noise figure below 4.5 dB and filtering by an OBPF to reduce the spontaneous emission noise of the EDFA, the optical signal is transmitted via an SMF to the PD. After photo-detection, the generated MW signal is transmitted to a W1-coupled coaxial output port. The tuning range of this system is limited by several components: the bandwidth of the MZM, the bandwidth of the PD and the tuning range of the LO source. However, although the MZM was operated at an LO frequency much higher than its 3 dB cut-off frequency, the complete operational frequency range of 20 MHz-110 GHz could be applied to the PD due to the optical amplification. Beside the advantage of having the complete operational frequency range by just needing half the frequency from the LO, this scheme is also nearly resistant against CD. In order to verify this, simulation and measurement results for the dispersion induced power penalty as a function of the RF frequency for the DSB and DSB-CS scheme are shown in Figure 3.10. Also here, as already supposed by the simulations shown in chapter 2.4, the influence of chirp for the simulations has been neglected as the used MZM is a zero chirp device.

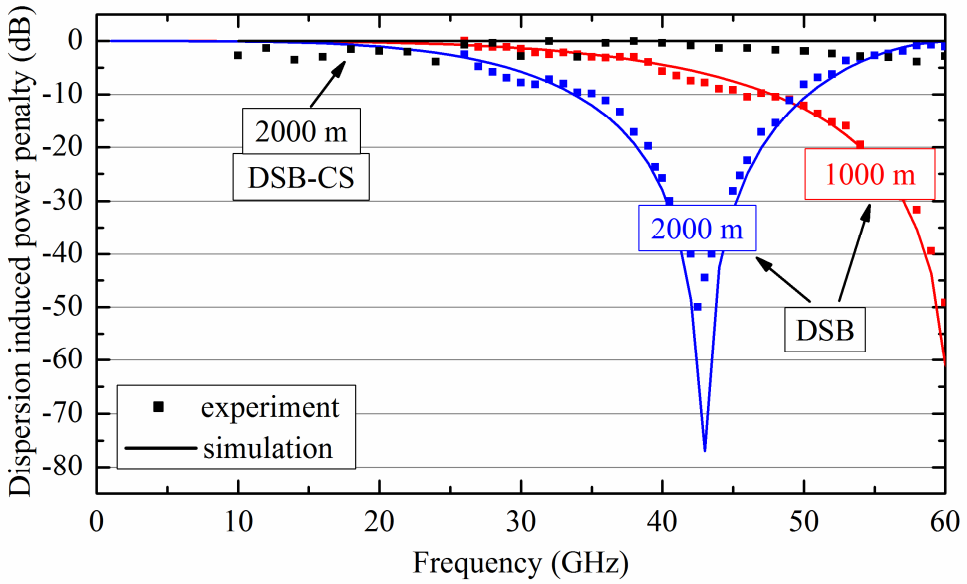

Figure 3.10: Dispersion induced power penalty for DSB and DSB-CS modulation as a function of frequency for different SMF lengths at a wavelength of 1550 nm and a dispersion factor of $D = 17$ ps/nm/km.

For the simulations and measurements, two different fiber lengths (1000 m and 2000 m) were used. Furthermore, for the DSB modulation scheme measurements only up to 60 GHz were possible as this was the limit of the used LO. Nevertheless, from the figure it can be seen that the simulation results for the DSB modulation scheme are matching very well with the experimental results. One can clearly see the minima where the dispersion drastically limits the transmission power at the corresponding frequency. However, from the measurement results of the DSB-CS modulation scheme it can be seen no minima up to 100 GHz is observed, i.e. that one cannot see an influence due to CD. This comes from the fact that the carrier is highly suppressed and, in contrast to the DSB modulation scheme, the generated MW signal results from the difference frequency between the first upper and lower sideband. Thus it can be stated that CD is negligible when using the DSB-CS modulation scheme and therefore this scheme is well suited if a remote transmitter unit is desired.

With this modulation scheme, also phase noise measurements of an applied 50 GHz signal coming from the LO, as well as the corresponding optically generated 100 GHz signal after photo-detection were performed. The measurements were carried out using an ESA with a computer assisted phase noise capture program. It should be noted that some boundary conditions have to be fulfilled in order to get reasonable results as the measurement using an ESA is an “all-noise” measurement (see phase noise theory in chapter 2.6). First of all,

the amplitude noise has to be negligible because the ESA measures the carrier power at one specific time and uses this value as the reference, i.e. the phase noise at 0 Hz offset (carrier) has a value of 0 dBc/Hz. If now the amplitude changes, the following measured values at higher offset frequencies also vary leading to the fact that they are related to the "wrong" reference value. The second boundary condition is that no frequency jitter or a fast frequency drift is observed as this would also lead to incorrect results (carrier as reference). The last important boundary condition is referred to the (measurement) noise floor of the ESA. The minimum measureable value cannot be lower than the noise floor of the ESA. However, under consideration of these boundary conditions the ESA allows precise phase noise measurements.

The measurement noise floor (MNF) for different RF powers was also measured, which sets the limit of the minimum measureable phase noise. The MNF will be measured without applying any signal. However, as the measurement system normally uses the carrier power as a reference, the measurement of the MNF will be performed by setting the RF power in the computer assisted phase noise capture program to the same RF power as measured with an RF signal. Thus, the phase noise cannot go below a specific value, determined by the difference between the RF power and the absolute noise floor of the ESA. This is denoted as the dynamic range. If the RF power of the MW signal is decreased, the dynamic range also decreases and thus, the MNF increases as the phase noise at 0 Hz offset is 0 dBc/Hz. The phase noise performance of the 50 GHz LO signal was measured directly using the ESA whereas the phase noise of the generated 100 GHz signal was measured using an external W-band harmonic mixer. The results are shown in Figure 3.11.

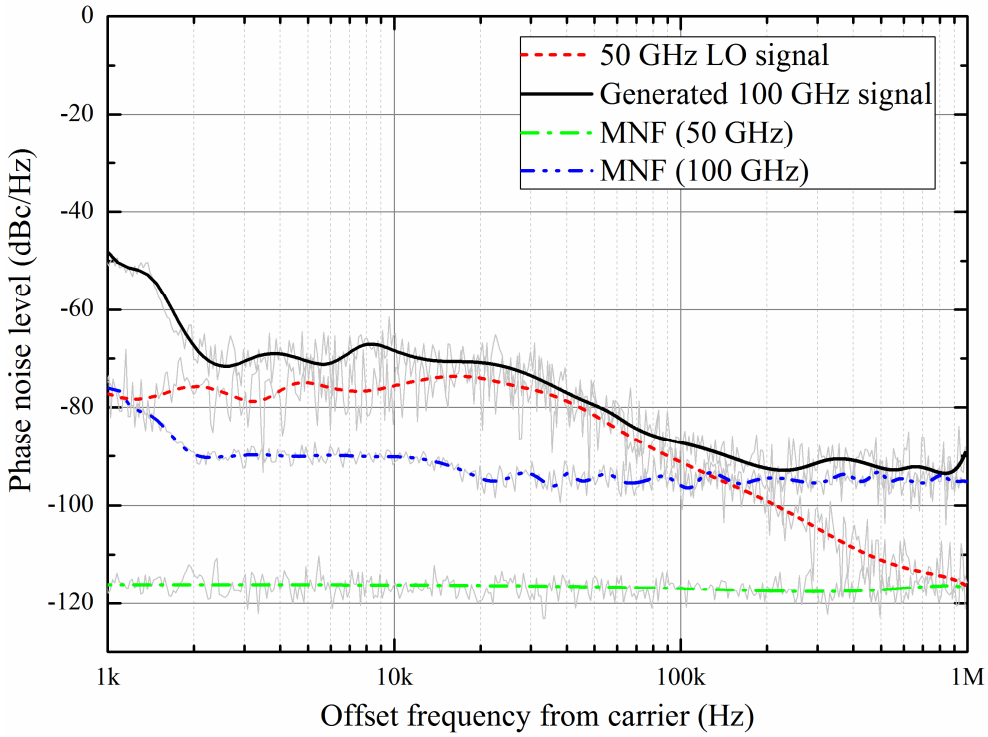

Figure 3.11: Phase noise measurement of the optically generated 100 GHz signal and the 50 GHz LO signal.

At an offset frequency of 10 kHz from the carrier, phase noise levels of about -76 dBc/Hz and -70 dBc/Hz from the LO and the PD output were measured, respectively. The RF power of the 50 GHz LO signal was -3 dBm while the power of the generated 100 GHz signal was -33 dBm without any amplification. For offset frequencies below ~3 kHz, the phase noise penalty between the LO and the generated signal is very high. Additional measurements have shown (see Figure 3.12) that this is due to the fact that a harmonic mixer was used to measure the generated MW signal. It is expected that this is the phase noise of the LO source, needed for the harmonic mixer, from the ESA itself. This can be seen from the measurement of the MNF (shows the same behavior) in Figure 3.11, which was measured without any signal but the LO from the ESA. For offset frequencies above ~200 kHz, the phase noise penalty rises drastically. Thus, additional measurements to get information about the measurement noise floor for the different power levels, also included in Figure 3.11, were performed. As the powers of the LO and the generated signal were -3 dBm and -33 dBm, the MNFs for both cases were also measured, showing that the minimum phase noise levels are about -118 dBc/Hz and -97 dBc/Hz, respectively. It is expected that an increase of the RF power leads to a measurement showing lower phase noise at high offset frequencies as the MNF decreases. Within an offset frequency range from ~20 kHz to 200 kHz, the phase noise penalty is ~2 dB. From the well-known formula

given in (2.58) which describes the relation between phase noise degradation and multiplication factor N, a phase noise penalty of 6 dB can be calculated. Nevertheless, the difference in phase noise penalty inside the mentioned region between calculation and measurement is ~4 dB, which is also an issue coming from the use of the harmonic mixer (see Figure 3.12). Here, it can be seen that the phase noise penalty between the measurements with and without harmonic mixer in the mentioned region is ~4 dB. As a conclusion, this can be traced back to the influence of the harmonic mixer.

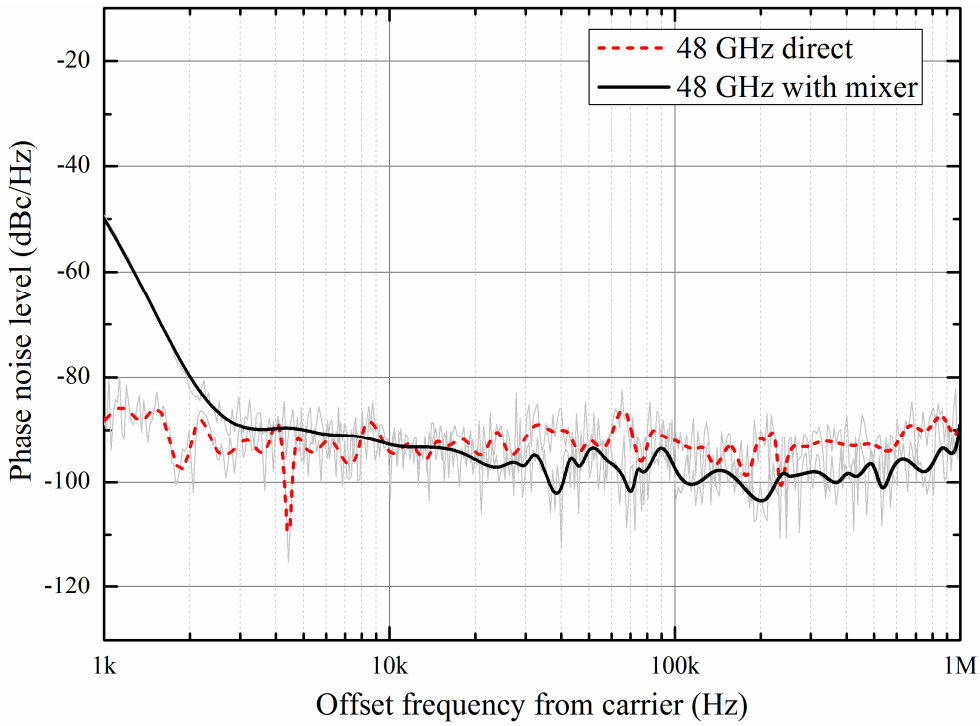

Figure 3.12: Comparison between phase noise measurements of an optically generated 48 GHz signal with and without a harmonic mixer.

As a result it can be stated that the DSB-CS modulation scheme is well approved to generate low phase noise MW signals. The phase noise is strongly dependent on the performance of the applied LO source.

As already described above, the measurement using an ESA is an “all-noise” measurement, i.e. the measurement also includes noise contributions from the ESA (noise floor) and from the setup itself (influence of the harmonic mixer). In order to get a better knowledge about these contributions, the phase noise of a fixed frequency MW signal source with a known phase noise spectrum (Rohde & Schwarz (R&S) FSUP Signal Source Analyzer –

performed by the manufacturer of the MW signal source) has been measured. Figure 3.13 shows the measured phase noise results of the MW source performed by the manufacturer with the R&S FSUP Signal Source Analyzer alone.

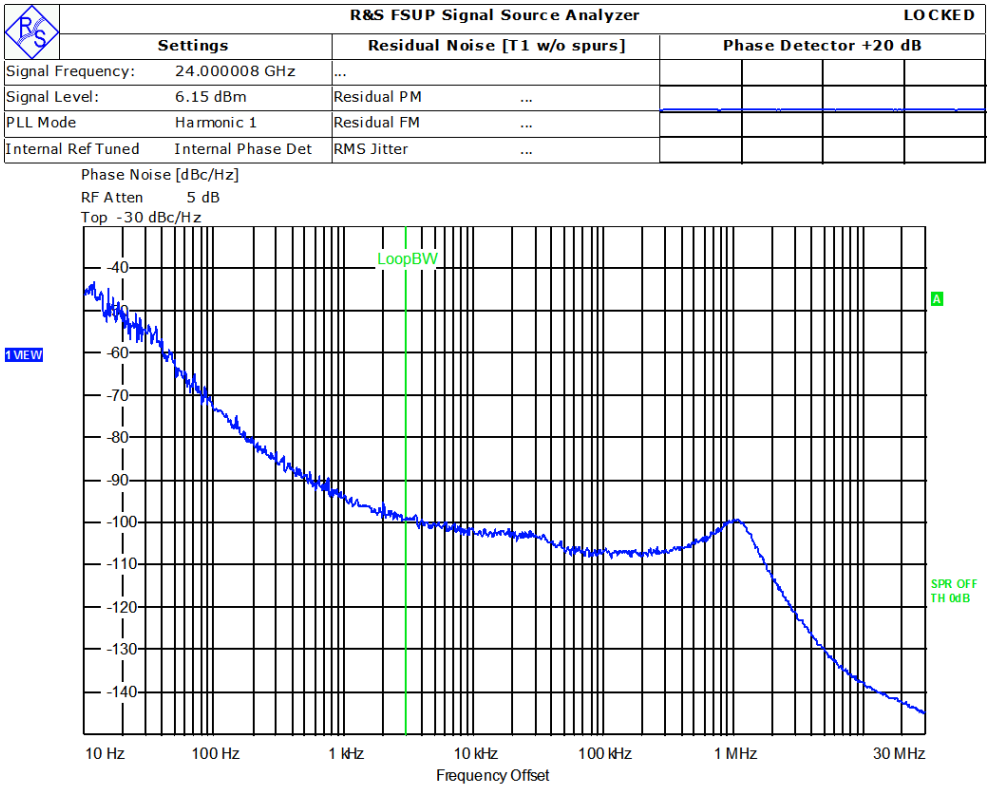

Figure 3.13: Phase noise measurement of a fixed frequency MW signal source using an R&S FSUP Signal Source Analyzer.

To visualize the noise contributions from the ESA, a phase noise measurement of the same fixed frequency MW signal source has been performed using the ESA. The results of both measurements techniques are shown in Figure 3.14.

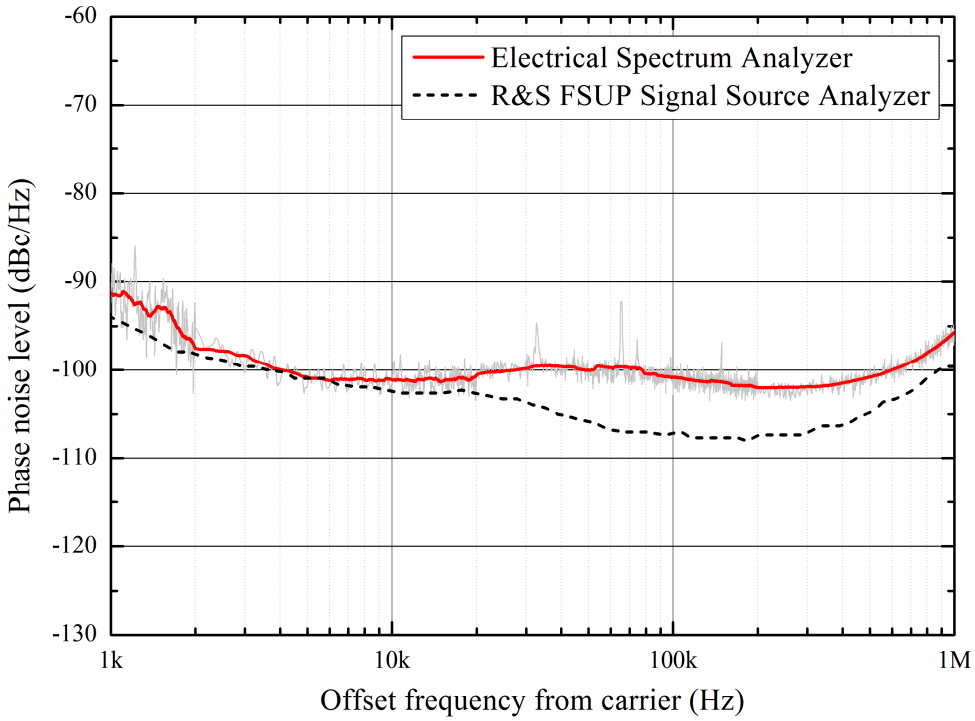

Figure 3.14: Comparison between phase noise measurements using different measurement techniques.

It can be seen that inside an offset frequency range of 10 kHz to 1 MHz the phase noise deviation varies between 2 and 7 dB, i.e. the measured phase noise level using the ESA inside this range is about 2-7 dB higher. Below 10 kHz offset, the measured phase noise level using the ESA is about 0.1-4 dB higher (without external harmonic mixer). Thus, it can be stated that the real phase noise is better than the measured phase noise using the ESA. Nevertheless, this measurement technique provides an easy solution to get a good knowledge about the phase noise performance of a photonic synthesizer.

3.2.3 Optical Multiplication Techniques

One major aim of this work is to develop a fully functional and RF tested photonic LO with a remote transmitter unit which fulfills technical specifications such as wide tunability, low phase noise performance and high output power. The center frequency of the generated photonic MW signal has to be around 100 GHz. The external modulation scheme is capable to fulfill all of the above mentioned specifications. Nevertheless, the requirements on the reference LO, e.g. when using the DSB-CS modulation scheme, are very strict. The center frequency has to be at least 50 GHz and the tuning range of the LO has to be half the tuning range of the generated MW signal while the phase noise has to be

low at the same time. Although electrical synthesizers providing such a high center frequency and tuning range are commercially available, the phase noise performance is often not good enough. Furthermore, such synthesizers are very costly. Thus, to decrease the requirements on the center frequency and the tuning range of the LO, optical multiplication schemes using an external modulation approach are suitable. In addition, the phase noise performance of low frequency synthesizers is much better than for high frequency tunable synthesizers, so one can expect to be able to compensate the additional phase noise resulting from the optical multiplication.

Optical quadrupling

One solution to achieve higher-order optical multiplication is to use two cascaded MZMs which will result in the generation of an MW signal at four times the reference LO frequency. Figure 3.15 shows the configuration of the photonic MW synthesizer using the optical quadrupling scheme.

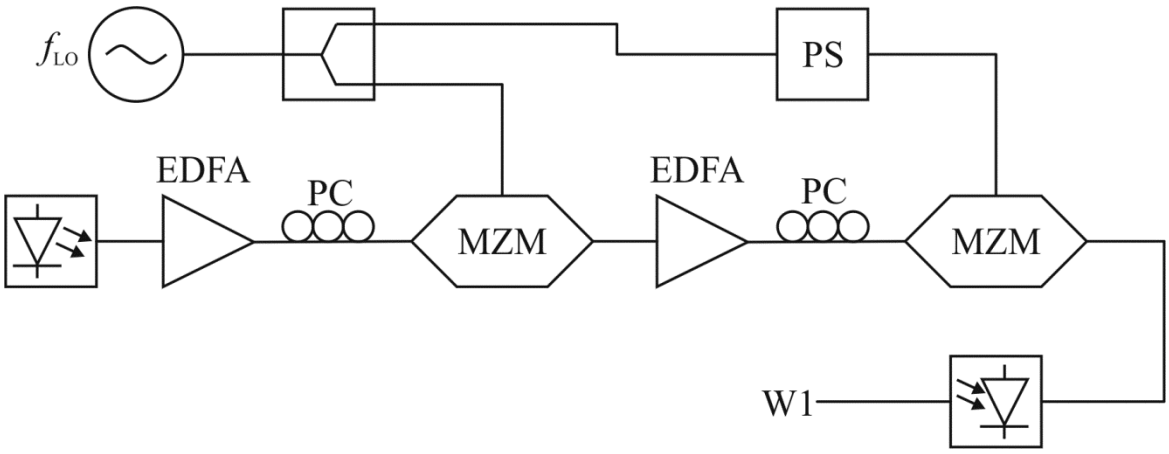

Figure 3.15: Photonic MW synthesizer using two cascaded MZMs to generate an MW frequency four times the reference frequency of the LO.

The first MZM is biased at V_π to achieve a DSB-CS signal where the side-modes are referred to as first order upper and lower sideband (USB and LSB). The optical frequency of the USB after the first modulator is $f_0 + f_{\mathrm{LO}}$, and that of the LSB is $f_0 - f_{\mathrm{LO}}$, where f_0 is denoted as the optical carrier frequency coming from the LD. Thus, the optical electric field at the output of the first MZM using the Bessel functions given in (2.11) can be approximately written as [137]

$$E_{\mathrm{out},1}(t) \approx E_0 \mathrm{J}_1(m_1) \cdot \{\cos[(\omega_0 - \omega_{\mathrm{LO}})t - \phi_1] + \cos[(\omega_0 + \omega_{\mathrm{LO}})t + \phi_1]\}, \quad (3.6)$$

where m_1 is the modulation index of the first MZM, ω_0 and ω_{LO} are the optical and electrical angular frequencies and ϕ_1 is the initial phase of the LO.

At the second MZM which is also biased at V_π, the $f_0 + f_{\mathrm{LO}}$ component (the USB of the first modulator) is modulated, resulting in an f_0 and $f_0 + 2f_{\mathrm{LO}}$ component. At the same time, f_0 and $f_0 - 2f_{\mathrm{LO}}$ components are generated from the $f_0 - f_{\mathrm{LO}}$ component (the LSB of the first modulator). Due to the fact that a phase shifter (PS) is inserted in front of the second MZM, the phase of the LO signal can be adjusted. This leads to a phase of the LO signal referred to as ϕ_2. Using the same analysis as for the first MZM, but with $E_{\mathrm{out},1}(t)$ as the input optical electric field, the optical electric field at the output of the second MZM becomes [137]

$$\begin{aligned} E_{\mathrm{out},2}(t) \approx\ & E_0 \mathrm{J}_1(m_1)\mathrm{J}_1(m_2) \cdot \cos[(\omega_0 - 2\omega_{\mathrm{LO}})t - \phi_1 - \phi_2] \\ & + E_0 \mathrm{J}_1(m_1)\mathrm{J}_1(m_2) \cdot \cos[(\omega_0 + 2\omega_{\mathrm{LO}})t + \phi_1 + \phi_2] \\ & + 2E_0 \mathrm{J}_1(m_1)\mathrm{J}_1(m_2) \cdot \cos(\phi_2 - \phi_1)\cos(\omega_0 t), \end{aligned} \quad (3.7)$$

with m_2 as the modulation index of the second MZM. By changing the phase ϕ_2 such that the phase difference between the RF inputs of the first and the second MZM is equal to $\pi/2$, the carrier component ($\omega_0 = 2\pi f_0$) will be suppressed at the output. As shown from the schematic in Figure 3.16, the output just comprises the $f_0 + 2f_{\mathrm{LO}}$ and $f_0 - 2f_{\mathrm{LO}}$ components while the others are highly suppressed. Thus, the MW signal at the output of the PD is four times the frequency of the LO.

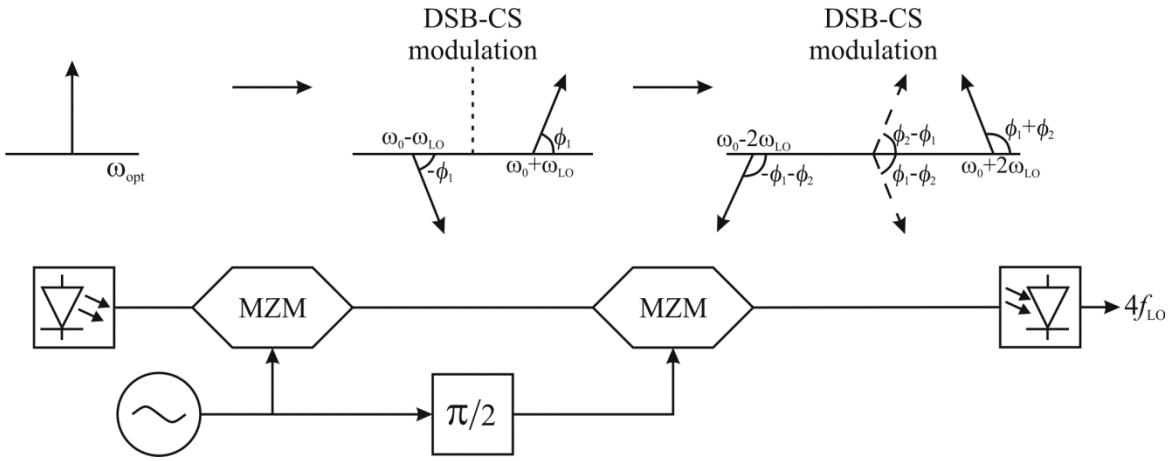

Figure 3.16: Principle of the quadrupling scheme using cascaded MZMs.

Experiments have been performed showing the capability of generating high-frequency MW signals with low phase noise. A low phase noise MW signal with a carrier frequency of 96 GHz was generated from a 24 GHz low phase noise fixed frequency LO provided by the INWAVE GmbH. Phase noise measurement results of the 24 GHz LO signal and the generated 96 GHz signal are shown in Figure 3.17.

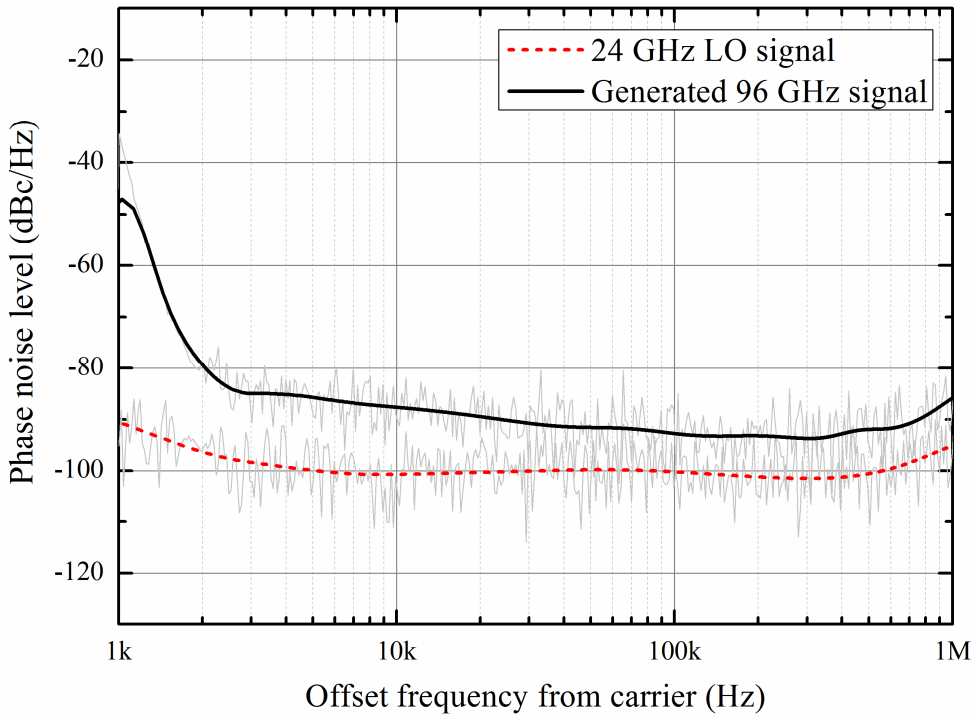

Figure 3.17: Phase noise measurement results using the optical quadrupling scheme.

It is obvious that for offset frequencies below ~3 kHz, the influence of the harmonic mixer drastically degrades the measured phase noise. From calculations it is expected that the phase noise due to quadrupling degrades by about 12 dB. Nevertheless, within an offset frequency range from ~20 kHz to 1 MHz, the phase noise penalty is just 8 dB. Taking into account the influence of the harmonic mixer concerning the power penalty as already mentioned above (Figure 3.12), i.e. the power penalty of ~4 dB, the measurements also confirm the calculated phase noise degradation.

Although the present system is well suited for frequency quadrupling, it is bulky and complex because two EDFAs, two polarization controllers, an electrical 3 dB coupler and a phase shifter, which has to be adjusted very well, are necessary. To reduce the size and the complexity, a quadrupling approach using just one MZM is investigated. As already described in chapter 2.2, an MZM is a nonlinear device which is also capable of creating higher harmonics. Thus, the applied LO power has to be increased. In order to get a better knowledge on the nonlinearity of an MZM, the optical output spectrum at different applied RF input powers based on the theory developed in chapter 2.2 has been simulated. Figure 3.18 shows simulation results of the optical output field for an MZM driven at an RF input power of 8 and 18 dBm. Furthermore, the simulations are based on carrier suppression modulation. Although the MZM which has been used for measurements can handle RF input powers up to 24 dBm, the maximum RF input power for the simulations was set at 18 dBm. This is due to comparison reasons with measurements, as the maximum provided RF output power of the synthesizer used for the measurements (Anritsu 68087B) is only 18 dBm. Furthermore, the LO frequency for the simulations was set at 4 GHz because the maximum provided output power of 18 dBm of the synthesizer is only available for frequencies up to 4 GHz while it drastically decreases for higher frequencies. Using these conditions, simulations are the only option to get information about the optical electric field at the output of the MZM because the minimum resolution of the available optical spectrum analyzer is just 0.1 nm, which is equal to ~12.5 GHz at 1550 nm wavelength.

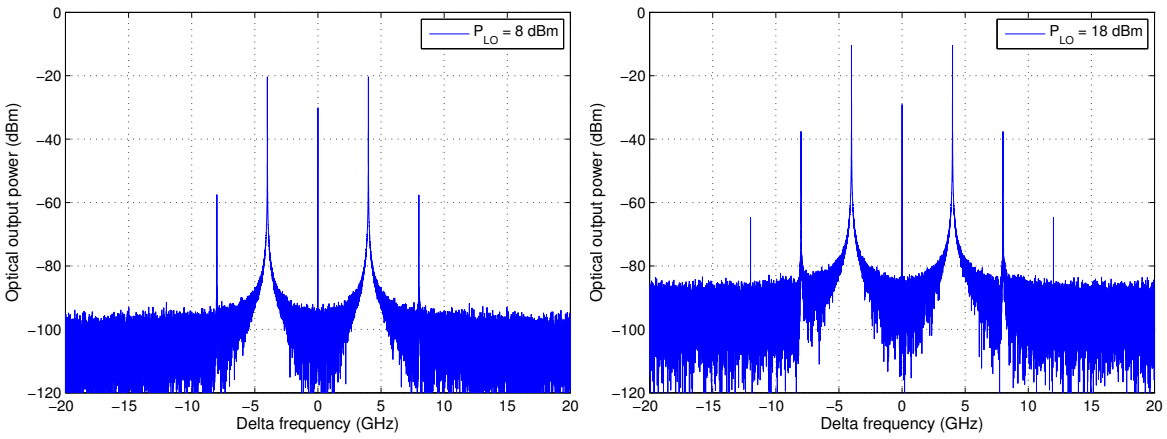

Figure 3.18: Simulation results of the optical output field of an MZM driven at an RF input power of 8 dBm (left) and an RF input power of 18 dBm (right).

From the simulation results on the left hand side, one can see that second order side modes are present, allowing a four time multiplication of the applied LO frequency. If the RF input power has been increased by 10 dB, as can be seen from the simulation on the right hand side, the optical power of the second order side modes increases by 20 dB. This is due to the fact that the second order side modes are related to the first kind Bessel function of second order which shows a quadratic behavior. Furthermore, such an increase of the RF input power will also give rise to third order side modes. Using a PD with a comparatively high responsivity, one can imagine to achieve six times the frequency of the LO. Furthermore, one can see that the optical carrier is suppressed by about 10 dB and 19 dB for an LO power of 8 dBm and 18 dBm, respectively. This is due to the fact that the sideband power strongly increases with LO power while the optical carrier power just changes slightly. The carrier is located at 0 GHz, which represents the carrier wavelength of 1550 nm, and the harmonics are given as a delta frequency from the carrier.

For the experimental characterization, the RF conversion efficiencies η_{RF} for the single-MZM approach driven by an LO source with a frequency of f_{LO} = 4 GHz were measured for different multiplication levels N. The used PD has a responsivity of 0.6 A/W and the generated photocurrent was fixed at 2 mA, which is equal to an optical input power of ~5 dBm. Figure 3.19 shows the measured conversion efficiencies for a multiplication factor of N = 4 as a function of the LO drive power. Additionally, the model described in chapter 2.2 has been used to simulate the RF conversion efficiencies of the single-MZM and of the cascaded MZM approach. The simulation results are also included in Figure 3.19.

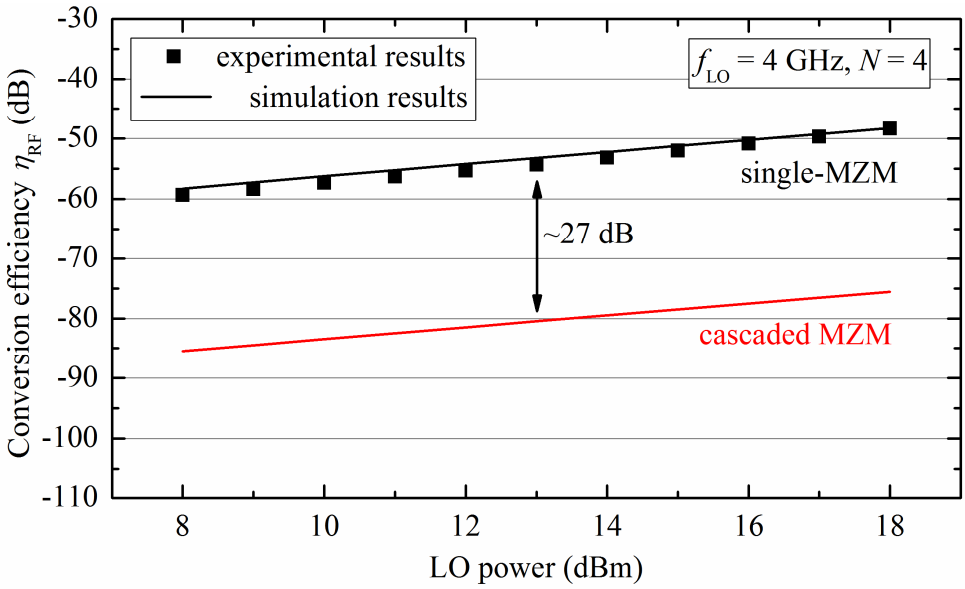

Figure 3.19: RF conversion efficiency vs. LO drive power for the single-MZM and the cascaded MZM approach.

For the simulation of the cascaded MZM approach, it was assumed that the optical input power in front of the first MZM was the same as for the single-MZM approach and furthermore, the second EDFA in front of the second MZM was omitted. It can be seen that the simulation results agree very well with the measurements. As expected, the RF conversion efficiency depends on the LO drive power in a linear behavior. This is due to the quadratic behavior of the second order harmonics as described above in combination with the square law detection of a PD. It can be further noted that the efficiencies for the cascaded MZM approach are approximately 27 dB smaller as compared to the single-MZM approach. This is caused by two reasons: Firstly, for the cascaded MZM approach, the LO power has to be divided for driving both MZMs, thus, it is reduced by 3 dB for each MZM. Furthermore, this leads to the fact that the generated first order harmonics of the first MZM, which will be used as the optical input signal for the second MZM, are also reduced by 3 dB. Additionally, the used phase shifter (ATM P1608) which is required for the phase adjustment has another ~2 dB loss. Therefore, the RF drive power for the first MZM is 3 dB lower, while the drive power for the second MZM is even 5 dB lower as compared to the single-MZM approach. Secondly, both MZMs have an optical insertion loss of ~7.8 dB. Thus, the optical input power to the second MZM is reduced by ~7.8 dB (insertion loss) in addition to the 3 dB mentioned above (first order harmonics). Taking into account the insertion loss of the second MZM and the losses from the 3 dB coupler and the PS, the overall losses can be calculated to be 26.6 dB. From formula (3.7), it can be

further seen that the behavior between conversion efficiency and LO drive power is also linear.

Based upon the above discussion, it can be concluded that the cascaded MZM approach would be as efficient as the single-MZM approach only if another electrical low-noise amplifier (LNA) with about 5 dB gain (to compensate for the losses of the RF drive power) and another optical amplifier with about 8 dB gain (to compensate for the optical insertion loss) was used. The cascaded MZM approach thus would significantly increase the complexity of the system, as not only an electrical LNA and an EDFA would be required but also an electrical phase shifter, a 3 dB coupler and a second polarization controller. Furthermore, the noise figure of the LNA and the ASE noise of the EDFA could also have an effect on the phase noise performance. If enough electrical or optical gain is provided, the cascaded MZM approach allows using a slightly higher multiplication factor, but this does not compensate for the additional noise and expenditure.

Higher-order multiplication using FWM effects in SOAs

To further increase the multiplication factor N, the optical signal which has been generated from the single-MZM approach is used to drive a highly nonlinear SOA. As theoretically investigated in chapter 2.3, a nonlinear SOA is capable of generating higher harmonics due to the FWM effect. The basic configuration of a photonic synthesizer concept based upon external modulation in conjunction with the FWM effect of the highly nonlinear SOA is shown in Figure 3.20.

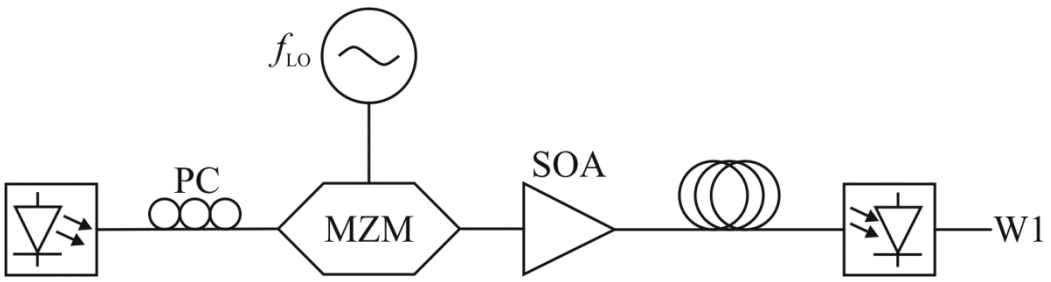

Figure 3.20: Photonic MW synthesizer using a single-MZM with a subsequent SOA to generate an MW frequency N times the reference frequency of the LO.

To achieve a high nonlinear operation and thus FWM, the SOA has to be driven in saturation condition. This means that the gain of the SOA will be decreased if the incident signal power increases. Thus, the gain characteristic is nonlinear depending on the input

signal power. Therefore, the optical input power to the SOA has to be as high as possible. Assuming the optical output signal from the single-MZM approach is introduced to the input port of the highly nonlinear SOA. Using the theory described in chapter 2.3, simulations have been performed showing the electrical output power of the PD for different multiplication factors N versus different LO drive powers applied to the MZM (see Figure 3.21). It has to be mentioned that the material parameters used for the simulations are taken from [50] as the datasheets of the SOAs used in this work do not provide this information. Thus, also the boundary conditions for the simulations have been adapted such that the SOA is driven in saturation. However, these simulations show that this photonic MW synthesizer concept is in principle able to achieve a higher-order multiplication.

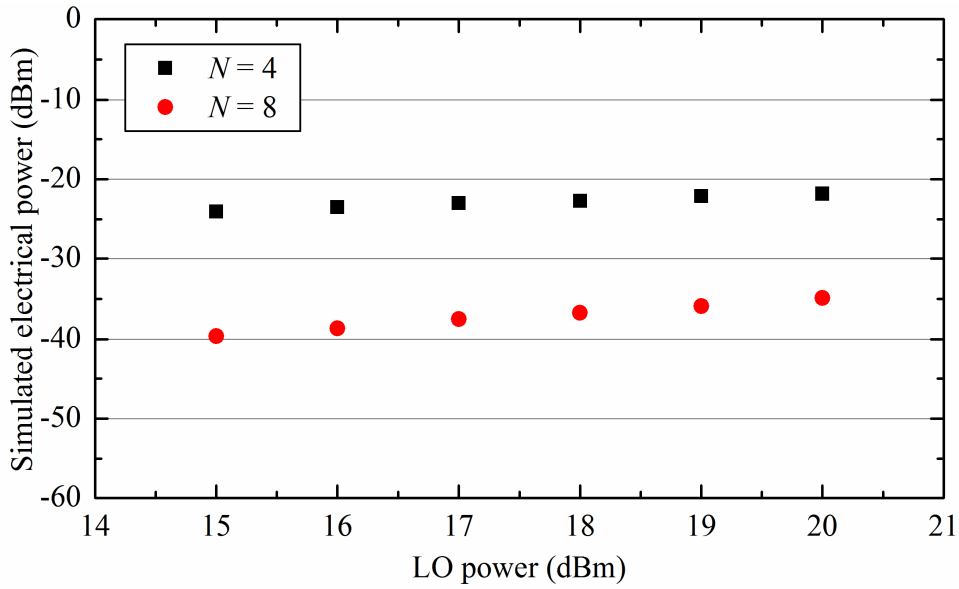

Figure 3.21: Simulated electrical power vs. LO drive power.

In order to verify this characteristic, experiments concerning the electrical output power as well as the RF conversion efficiency have been performed using two different SOAs, both from Covega/Thorlabs. The first SOA (BOA-1004) is a booster SOA providing a lower nonlinear behavior than the second SOA (SOA-1117) which is especially designed for nonlinear operation. The characterization is based on the setup described above, but with an additional EDFA in front of the SOA to obtain the needed high optical input power. The maximum allowed optical input power referred to the manufacturer's datasheet is about +13 dBm for both SOAs. Nevertheless, for safety reasons, the maximum optical input power was set to +11 dBm. As the saturation optical output power of the SOAs are too

high for the subsequent PD, an optical attenuator was used to set the optical input power to the PD at ~5 dBm, which is equal to 2 mA of photocurrent. Furthermore, the LO frequency was also set at 4 GHz. Figure 3.22 shows the measured electrical power at the output of the PD as a function of the LO drive power for the two different SOAs.

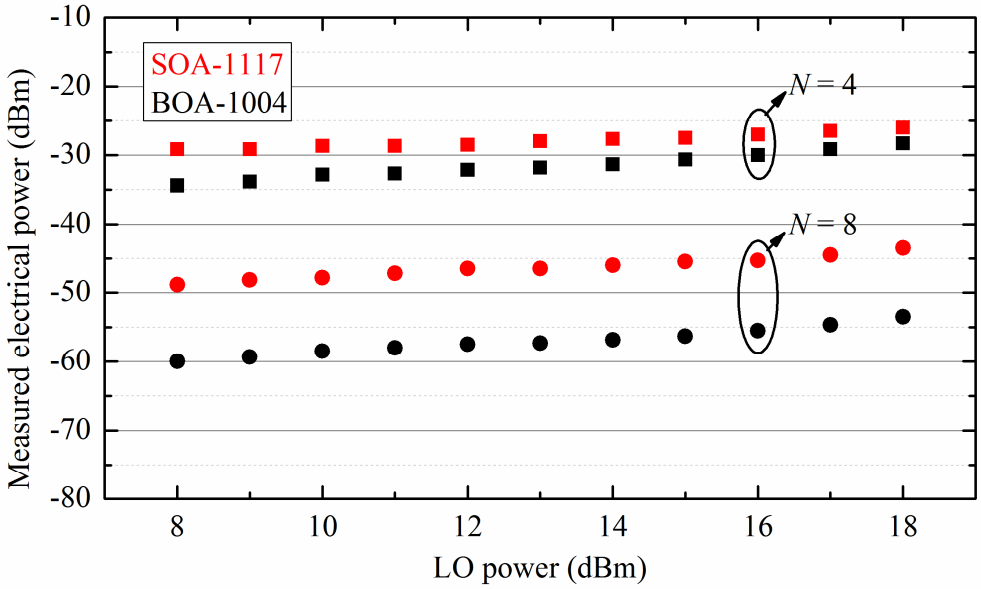

Figure 3.22: Measured electrical power vs. LO drive power for two different SOAs.

From the measurement first of all it can be seen that if the LO power increases, the RF output power also increases. This is in principle the same behavior as found from the simulations, although the results cannot be directly compared due to the unknown material parameters. Compared to the MZM approaches without SOA, here an increase of 1 dB of LO power will just result in an average increase of about 0.5 dB for the RF output power. As a consequence, the RF conversion efficiency will slightly decrease while increasing the LO drive power as shown in Figure 3.23.

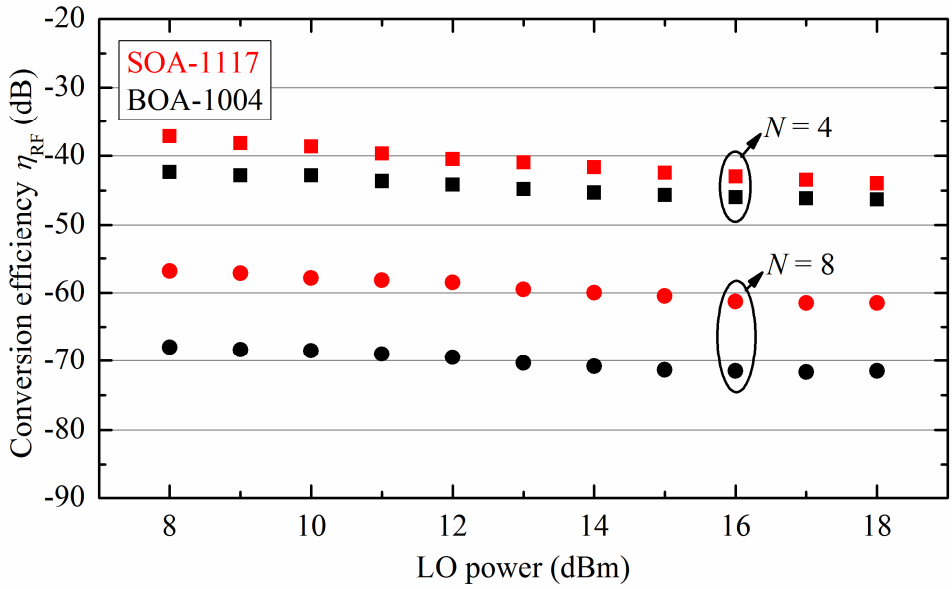

Figure 3.23: RF conversion efficiency vs. LO drive power for two different SOAs.

This can be attributed to the fact that the SOA is driven in saturation condition. Thus, the provided optical gain of the SOA is dependent on the optical input power, limited by the saturation output power. If the LO power is now decreased, the optical power of the harmonics from the MZM also decreases (see Figure 3.18). But, if the overall optical power of the harmonics is high enough so that the SOA is still in saturation, the optical gain of the SOA increases. This will result in the fact that the gain provided by the SOA will again increase the optical power of the harmonics. This phenomenon can be seen from the results in Figure 3.23, as a saturation of the conversion efficiency is observed for RF input powers higher than about 15 dBm.

Furthermore, it is shown that a multiplication of $N = 8$ has been achieved resulting from the nonlinear behavior of the SOA which is theoretically described in chapter 2.3. The difference in conversion efficiency between the SOAs is due to the difference in the nonlinear behavior. Thus, if the nonlinear behavior is even stronger, it is expected that the conversion efficiency will further increase, as the nonlinearity has a strong influence on the FWM efficiency. As already mentioned above, the measurements of the conversion efficiency were performed at an LO frequency of 4 GHz. Additional measurements have shown that the RF conversion efficiency at the same multiplication level slightly depends on the LO frequency. For example, when varying the LO frequency from 2-4 GHz at a multiplication level of $N = 8$, the RF conversion efficiency just changes by about 0.5 dB. When the LO frequency is changed from 4 to 6 GHz, the change in RF conversion

efficiency is about 3 dB. The main reason is that the 3 dB bandwidth of the used PD was limited at 50 GHz. Thus, it is expected that the RF conversion efficiency is nearly independent from the LO frequency and only limited by the bandwidth of the PD.

When comparing this approach with the single-MZM approach, it can be stated that for a multiplication factor of $N = 4$, the difference in conversion efficiency at high LO powers is comparably small. As the MZM can handle RF input powers up to 24 dBm, it is assumed that due to the gain saturation of the SOA, the conversion efficiency at such a high LO power is nearly equal for both approaches, provided that the conversion efficiency for the single-MZM approach further increases. Nevertheless, to achieve such a high RF input power, an additional RF amplifier is needed. If a high conversion efficiency using a low power LO source is desired, the SOA approach is favorable, as e.g. the conversion efficiency at an LO power of 8 dBm is more than 20 dB higher, compared to the single-MZM approach. The major advantage of the SOA approach is that it is capable of generating a frequency N-times (eight times has been shown experimentally) of the LO frequency. This allows using a low frequency LO source to generate a high frequency MW signal. Furthermore, as the conversion efficiency for a multiplication factor of $N = 8$ shows nearly the same behavior as for $N = 4$, also a low power LO source can be used.

To investigate the signal quality, phase noise measurements were performed for the fundamental LO frequency ($f_{\mathrm{LO}} = 4$ GHz) and for the generated MW signals with a multiplication factor of $N = 4$ and $N = 8$. Furthermore, the corresponding measurement noise floor for the different MW signals has also been measured. Based upon the theory given in chapter 2.6, it is expected that the phase noise for a multiplication factor of $N = 4$ and $N = 8$ increases by 12 and 18 dB, respectively. The results of these phase noise measurements are shown in Figure 3.24.

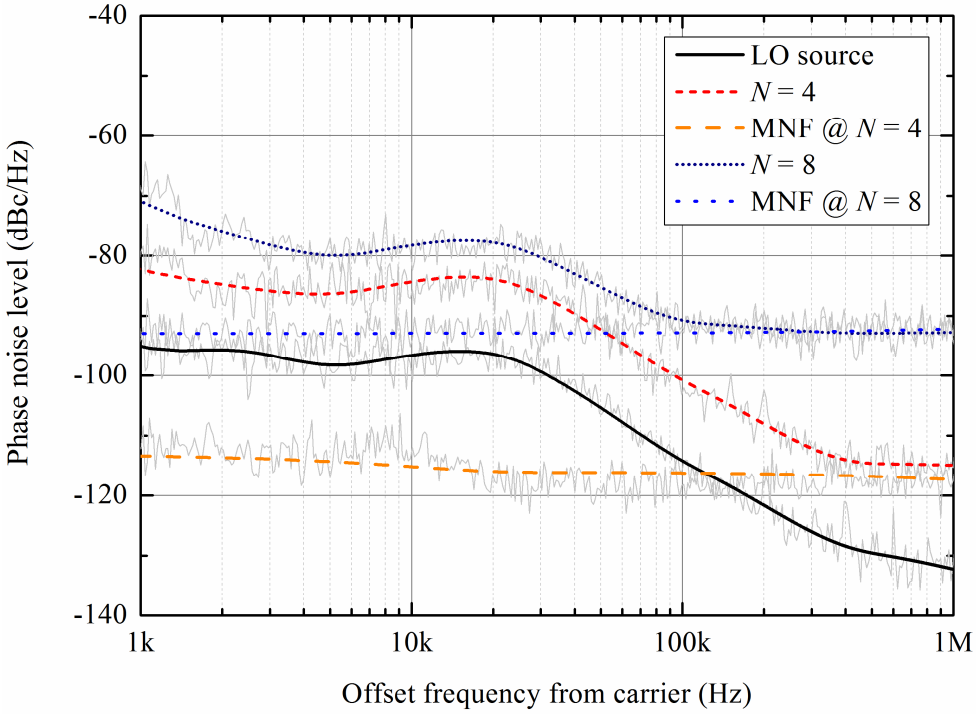

Figure 3.24: Phase noise measurements of the LO signal and the four and eight times multiplied MW signal.

From the figure, it can be seen that the phase noise performance degrades as expected. It is obvious that at high offset frequencies, the phase noise measurement is limited by the measurement noise floor which is described in chapter 3.2.2. Furthermore, as also shown in chapter 3.2.2, for offset frequencies below about 3 kHz the measurement setup also has an influence on the phase noise measurement. Thus, it is expected that the phase noise of the generated MW signals at low and even high offset frequencies are showing the same behavior as for the LO signal, but with the corresponding degradation of 12 and 18 dB for $N = 4$ and $N = 8$, respectively. Although an SOA generates noise (ASE), it can be stated that no influence on the quality of the generated MW signal is observed.

The results have shown that the optical multiplication scheme using a single MZM with a subsequent SOA is capable of generating high frequency and low phase noise MW signals from a low frequency reference source. Assuming such a system with a high power photoreceiver which either offers a 3 dB bandwidth of ~100 GHz or which is resonant at ~100 GHz offering 10% bandwidth and an LO source providing a central frequency of 12.5 GHz with a tuning range of 1.25 GHz and phase noise levels 18 dB below the required specifications for the PHOMIGEN project, the overall project goal can be achieved. Furthermore, as the photonic synthesizer working at 1.55 µm wavelength should

include a remote transmitter unit, it was also shown that the influence of CD is negligible when using DSB-CS modulation.

4 Optoelectronic Oscillators

Although it has been shown that external modulation in conjunction with the nonlinearities in an SOA, which allows a high optical frequency multiplication, relaxes the requirements on the needed electrical reference oscillator, the phase noise of the generated MW signals is still limited by the phase noise performance of the electrical reference oscillator. To overcome this limitation, it was another major objective of this work to investigate possibilities for generating high frequency tunable MW signals with low phase noise using a concept that does not require any electrical reference oscillator.

Early investigations have shown the capability to generate stable picosecond pulses without the need for a reference LO by using a resonant feedback loop [12]. An approach using a fiber-based feedback loop, investigated by Yao and Maleki [138], [139], is referred to as optoelectronic oscillator (OEO). An OEO is an oscillator that converts optical energy from a CW laser source into a pure and stable MW signal. An OEO consists of an electro-optic modulator driven by a feedback circuit which uses a long optical SMF as a delay line to achieve a high quality factor (Q) and a PD to convert the optical energy to a feedback RF voltage. The Q-factor given by $Q = 2\pi f \tau_\mathrm{d}$ is a figure of merit for a resonator. The energy-decay time τ_d, which is equivalent to the delay time, describes the energy storage capability of the resonator at its resonant frequency f. High Q or low loss energy storage elements are essential for generating such high-spectral-purity and high-stability MW signals. Such an optoelectronic oscillator has the capability to generate MW signals with extremely low phase noise. For an OEO with a single loop of 2 km length, the phase noise was measured to be -105 dBc/Hz at 1 kHz offset from a 10 GHz carrier [13].

In order to get knowledge about the mode of operation and the phase noise performance of an OEO, at first an OEO, consisting of one long fiber loop, will be described and analyzed in chapter 4.1. Here, it will be shown that a major drawback of such an OEO is the need for a bandpass filter providing an ultra-narrow bandwidth as in reality, a bandpass filter with a center frequency in the GHz range and a bandwidth below MHz is hard to realize. In order to relax the requirements on the bandpass filter, another approach using additional loops, referred to as multi-loop OEO, will be discussed in chapter 4.2. Nevertheless, also in a multi-loop OEO a narrow bandwidth bandpass filter is an essential component.

In contrast to the generation of MW signals using e.g. external modulation schemes, the frequency tuning capability is very limited, mainly due to the need for a narrow bandwidth bandpass filter. In order to achieve frequency tuning with an OEO, several bandpass filters selected by a switch had been used in [13] to allow for coarse tuning (stepwise tuning) the frequency. In addition, the continuous frequency tuning range around the center frequency of the employed bandpass filter was limited to be slightly above 100 kHz. However, such an approach makes the system more complex and to achieve a high frequency tuning range with a low tuning resolution at the same time, a lot of narrow bandwidth bandpass filters are needed. With the aim to improve the frequency tuning range of an OEO, an approach using a tunable laser for taking the advantage of having wavelength dispersion in fibers was used in [14]. But although the laser was tunable by ±40 nm in the optical domain, the frequency tunability of the generated MW signal was still very limited with a maximum tuning range of less than 2 MHz around the bandpass filter's center frequency of 9 GHz. To overcome the frequency tunability limitation due to the narrow bandwidth bandpass filter, a novel approach of an OEO, using a standard high-pass filter instead, will be presented and analyzed in chapter 4.3 [T], [U]. Experimental results are verifying that the novel OEO allows high frequency MW signal generation with ultra-low phase noise while at the same time providing hundreds of MHz frequency tuning range.

4.1 Single-Loop Optoelectronic Oscillators

As the name "singe-loop" implies, this OEO consists of just one long fiber loop. The single-loop OEO consists of a laser, an e/o-modulator which is typically an MZM, a long fiber link, a PD followed by an electrical RF amplifier, a narrow bandwidth bandpass filter and an electrical 3 dB splitter which on the one hand closes the feedback loop to the RF driving port of the MZM and on the other hand provides the RF output port (Figure 4.1). The long fiber link serves as the delay, providing the needed high Q for low noise oscillation.

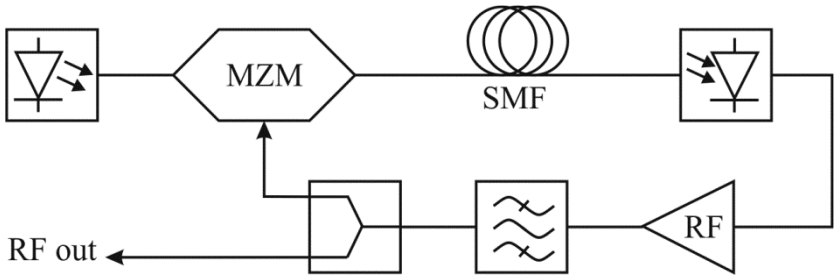

Figure 4.1: Block diagram of the single-loop OEO.

By closing the loop, self-sustained oscillation starts from noise which will be amplified inside the loop. The threshold condition for achieving oscillation is that the small signal open-loop gain G_S, defined by equation (4.1), must be larger than unity [138].

$$G_\mathrm{S} = \frac{\mathrm{d}V_\mathrm{out}}{\mathrm{d}V_\mathrm{in}}\bigg|_{V_\mathrm{in}=0} = -\frac{\eta\pi I_\mathrm{ph} R_\mathrm{L} G_\mathrm{A}}{V_\pi}\cos\left(\frac{\pi V_\mathrm{B}}{V_\pi}\right). \tag{4.1}$$

Here, the factor η determines the extinction ratio of the MZM by $(1+\eta)/(1-\eta)$. Furthermore, I_ph is the photocurrent, R_L is the load resistance of the PD, G_A is the voltage gain of the amplifier and V_B and V_π is the bias and half-wave voltage of the MZM, respectively. This means that inside the loop the sum of the gain and all losses due to the feedback must be larger or at least equal to 1. If this condition is fulfilled, several modes which add up in phase can sustain oscillation. The oscillation frequency is then determined by [138]

$$f_\mathrm{osc} = \frac{k}{\tau} = k\frac{\mathrm{c}_0}{n_\mathrm{SMF} L} = k \cdot \Delta\nu, \qquad (k = 0, 1, 2, \dots), \tag{4.2}$$

where τ is denoted as the time delay due to the fiber loop, c_0 is the velocity of light in vacuum, $n_\mathrm{SMF} \approx 1.4682$ is the refractive index of the SMF, L is the fiber length and $\Delta\nu$ is the free spectral range (FSR). It should be noted that also the electronic circuit inside the loop causes a time delay, but as this time delay is much smaller than the time delay resulting from the fiber it will be neglected in this case. It is obvious that (4.2) will result in a frequency comb where the FSR is inversely proportional to the time delay τ. Assuming a long fiber in the kilometer-range which is a typical value for an OEO, the FSR is thus just in the kHz-range. Here, the very narrow bandwidth bandpass filter is used to select the

mode with the desired frequency while suppressing the unwanted modes at the same time. As the threshold condition for oscillation is typically only fulfilled for modes around the center frequency of the filter, the modes (in terms of frequency) closest to this center frequency will oscillate. Thus, the bandwidth of the filter should be ideally lower than the FSR to completely suppress all other modes. Furthermore, concerning the frequency tunability, the need for a bandpass filter with a very low bandwidth is a drawback. The maximum achievable tuning range is limited by the bandwidth of the filter, i.e. the threshold condition for oscillation can be only fulfilled inside the bandwidth around the center frequency of the filter. If e.g. the filter's bandwidth is about 1 MHz, then the maximum achievable frequency tuning range cannot exceed this value.

The phase noise of the generated signal in an OEO is related to the time delay and thus the loop length. The RF power spectral density for a single-loop OEO is given as [138], [139]

$$S_{\mathrm{RF}}(f') = \frac{\delta}{(2-\delta/\tau) - 2\sqrt{1-\delta/\tau}\cos(2\pi f'\tau)}, \tag{4.3}$$

where f' is the frequency offset from the carrier and δ is the noise-to-signal ratio (NSR) determined by the small-signal open-loop gain, the noise contributions from the components (laser, PD, amplifier) and the driving conditions of the MZM. A detailed analysis can be found e.g. in [138] and [139]. Assuming that amplitude fluctuations are negligible, the PSD of the OEO is equal to the single-sideband phase noise. Although a longer loop theoretically offers lower phase noise performance, the minimum achievable phase noise is also limited by the NSR of the generated MW signal given as [139]

$$\delta = \frac{|G_{\mathrm{S}}|^2}{1-1/|G_{\mathrm{S}}|}\frac{4\mathrm{k_B}T(NF) + N_{\mathrm{el,shot}} + N_{\mathrm{el,RIN}}}{4\eta^2\cos^2(\pi V_{\mathrm{B}}/V_{\pi})I_{\mathrm{ph}}^2 R}, \tag{4.4}$$

with $4\mathrm{k_B}T(NF)$ as the thermal noise including the noise figure of the amplifier, $N_{el,shot}$ and $N_{\mathrm{el,RIN}}$ as the shot noise and RIN, respectively (see also chapter 2.6). In order to get a better knowledge on the limitation, the NSR for different laser RIN levels as a function of the photocurrent has been simulated, as can be seen from Figure 4.2 [139]. For the simulation the small-signal open-loop gain $|G_{\mathrm{s}}|$ was assumed to be 1.5, as the NSR is

minimal at this value [139]. The equation used for simulating the NSR is thus determined by [139]

$$\delta_{\min} = \frac{4k_B T(NF) + N_{\text{el,shot}} + N_{\text{el,RIN}}}{(16/27) I_{\text{ph}}^2 R}. \tag{4.5}$$

The NF of the RF amplifier was assumed to be 3 dB which represents a low noise amplifier. Here, additional noise contributions like e.g. ASE noise when using an EDFA are not taken into account.

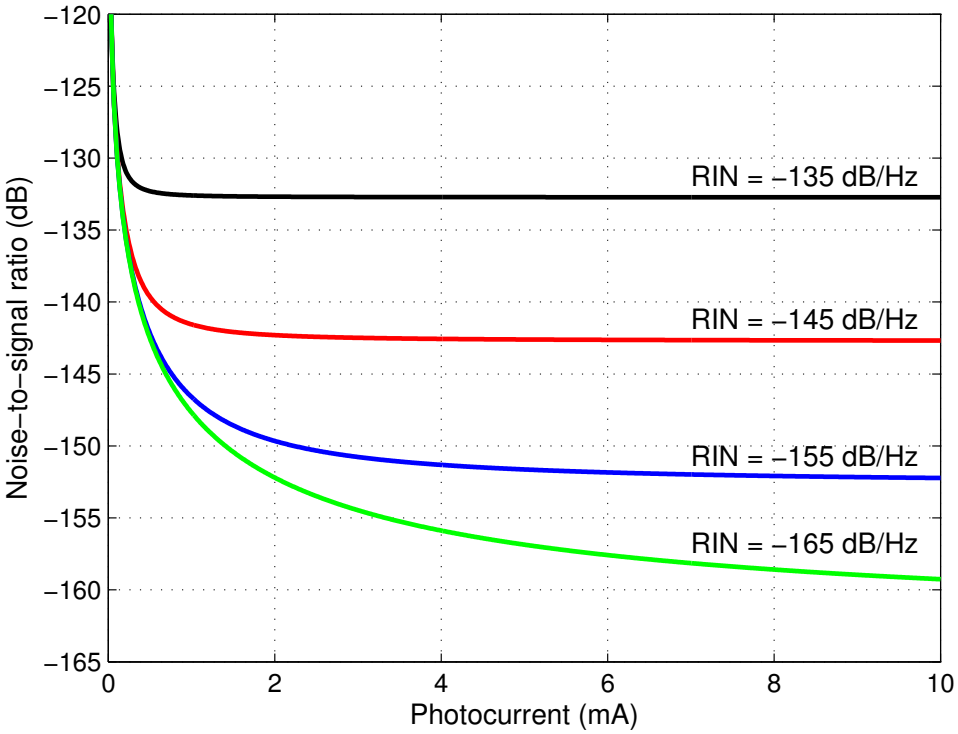

Figure 4.2: Calculated NSR as a function of the photocurrent for different RIN values from the laser.

From the figure, it is obvious that the SNR, which is the inverse NSR, of the generated MW signal is strongly limited by the laser's RIN. Furthermore, it can be also seen that the higher the photocurrent, the lower the NSR until it saturates, i.e. there is a limitation such that the SNR cannot be further increased. This comes from the fact that the NSR is inversely proportional to the quadratic photocurrent and the noise contribution from the RIN is the only noise which also increases quadratically with photocurrent while the thermal noise is constant and the shot noise increases linearly (see equation (4.5)). This means that the contributions from thermal noise and shot noise are becoming small

compared to RIN noise with increasing photocurrent. As a consequence, the RIN noise dominates at high photocurrents.

Due to the fact that the SNR is limited, the minimum achievable phase noise, calculated by using equation (4.3), of the generated MW signal is also limited. Assuming an OEO with a fiber length of 2 km, resulting in a time delay of ~9.8 µs and an FSR between the modes of ~102 kHz, as well as a laser having a RIN of -145 dB/Hz. Furthermore, it is also assumed that the small-signal open-loop gain is again 1.5 and the noise figure of the RF amplifier is also 3 dB. Then the NSR from the simulation above becomes -142.7 dB at a photocurrent of 10 mA. Using these values, the phase noise spectrum has been simulated using equation (4.3) as shown in Figure 4.3. From the equation it becomes clear that the phase noise is lowest if the cosine becomes -1, i.e. at a frequency offset of $f' = 1/2\tau$ which is about 51 kHz. Furthermore, as the NSR is about 10^9-times smaller than the time delay, the δ/τ-terms can be neglected such that the minimum achievable phase noise becomes $S_{\mathrm{RF,min}}(f' = 1/2\tau) \approx \delta/4$, which is about -148.7 dBc/Hz. Another strong influence on the phase noise performance of a single-loop OEO is given by the fact that the bandwidth of the bandpass filter is usually wider than the FSR between the modes. Thus, the phase noise spectrum contains the contributions of these modes which are reflected as strong spurious peaks. Here, it should be mentioned that the simulation is independent of the filter characteristics, i.e. the bandwidth of the filter is not taken into account.

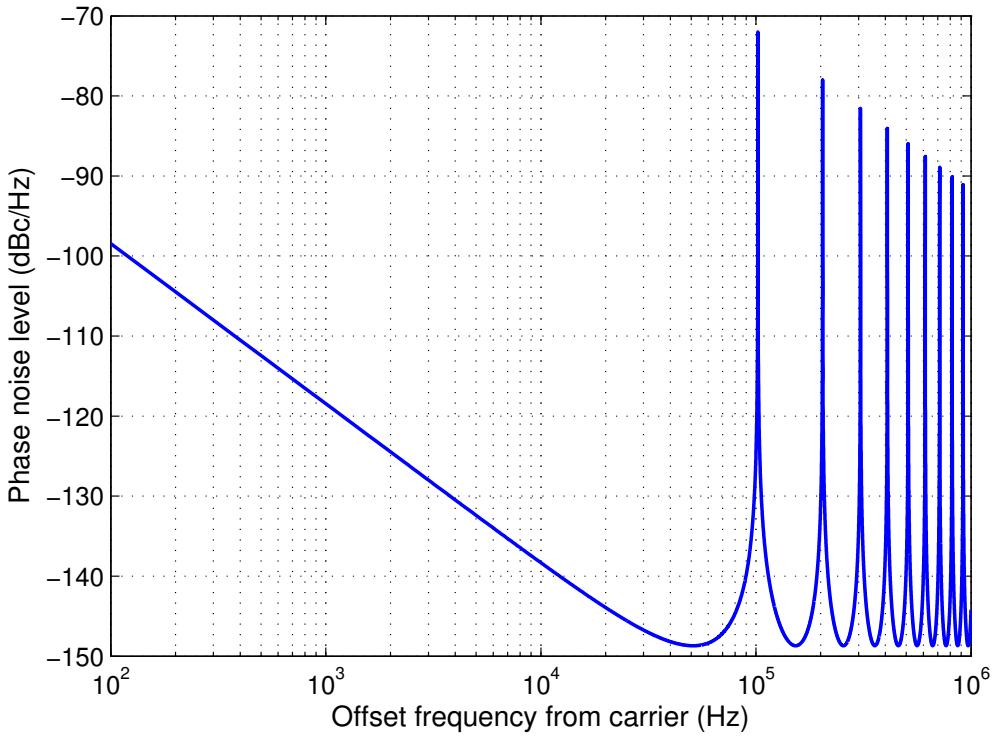

Figure 4.3: Simulation of the phase noise spectrum of the single-loop OEO.

As expected, one can see that the phase noise saturates at about -148.7 dBc/Hz. Furthermore, one can clearly see the above mentioned spurious peaks at multiples of ~102 kHz. In order to suppress these spurious peaks, the bandwidth of the bandpass filter has to be smaller than the FSR. But, as already stated above, in reality a bandpass filter with a center frequency in the GHz range and a bandwidth below MHz is hard to realize. Another possibility to reduce these peaks is to use additional loops resulting in a so called multi-loop OEO.

4.2 Multi-Loop Optoelectronic Oscillators

In a multi-loop OEO, additional loops are inserted with lengths much shorter than that of the “main” loop. Assuming a multi-loop OEO with two loops, which is referred to as dual-loop OEO, the light coming out of the MZM is splitted equally into two parts. Both parts form a loop including an SMF which is typically in the km-range for the main loop, a few meters up to a few hundreds of meters for the second loop and a subsequent PD. After photo-detection, both generated signals are combined by using an electrical 3 dB combiner. The further procedure is the same as for the single-loop OEO. The oscillation frequency for the dual-loop OEO is determined by [140]

$$f_{\mathrm{osc}} = \frac{k}{\tau_1} = \frac{m}{\tau_2}, \tag{4.6}$$

where k and m are integers and τ_1 and τ_2 are the time delays resulting from the lengths of the long and the short loop, respectively. Assuming that both loops are independent of each other, every loop generates a frequency comb having a different FSR depending on the loop length. Due to the use of the electrical 3 dB combiner both frequency combs overlap. As the FSR of both loops is different, just the modes which have exactly the same frequency in both loops are able to oscillate while the other modes are highly suppressed, i.e. the resulting FSR is the FSR between the modes which are able to oscillate. Thus, the short loop relaxes the frequency selectivity of the bandpass filter [140]. The principle of the mode selection is shown in Figure 4.4.

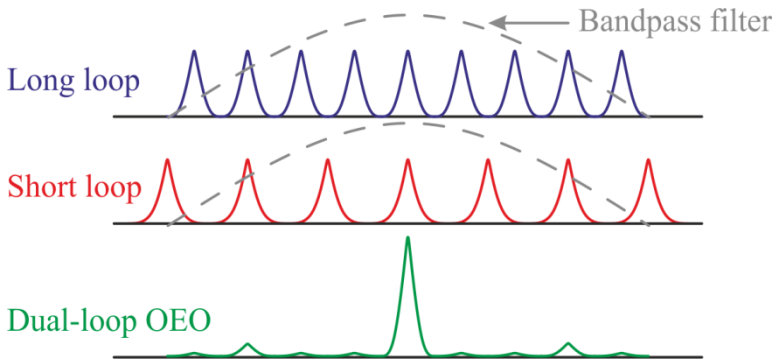

Figure 4.4: Principle of mode selection in a dual-loop OEO.

It should be mentioned that such a scheme strongly reduces the spurious peaks, but they are not completely cancelled out because other than the filter characteristic shown in Figure 4.4, the bandwidth of the bandpass filter is typically broader than the resulting FSR of the dual-loop OEO.

The RF power spectral density and thus the single-sideband phase noise, when neglecting the amplitude fluctuations, for a dual-loop OEO including the filter characteristics (single pole filter) can be written as [142]

$$S_{\mathrm{RF}}(f') = \frac{\delta}{\left|1 - A(f') \cdot \left(\exp(\mathrm{j}2\pi f'\tau_1) + \exp(\mathrm{j}2\pi f'\tau_2)\right)/2\right|^2 \cdot \sqrt{2\pi f'}}, \tag{4.7}$$

with f' as the frequency offset from the carrier and δ as the NSR. The term $A(f')$ describes the filter's characteristic and is given as [142]

$$A(f') = \frac{2\pi f_{\mathrm{f}}}{2\pi f_{\mathrm{f}} - \mathrm{j}2\pi f'}, \tag{4.8}$$

where f_{f} is the half-width at half-maximum transmission spectrum of the filter. It should be noted that the factor $\sqrt{2\pi f'}$ in equation (4.7) acts as a correction factor for the filter characteristic and also includes a noise source although it is not yet fully clarified [142]. However, this also influences the slope of the phase noise at low offset frequencies which means that the filter not only influences the spurious peaks but also the complete phase noise. As can be seen from equation (4.7), if the short loop is x-times shorter than the long loop ($\tau_1 = x\tau_2$) then the phase noise performance is mainly determined by the long loop.

A multi-loop OEO can be realized either with additional optical loops [141] or an additional electrical loop [143]. Both schemes are capable of generating high-spectral-purity and high-stability MW signals.

4.3 Tunable Dual-Loop Optoelectronic Oscillator

As already described above, the frequency tuning capability of an OEO is limited by the bandpass filter, i.e. the tuning range cannot exceed the bandwidth of the employed bandpass filter. In order to extend the frequency tuning range, the limitation resulting from the narrow bandwidth of the bandpass filter has to be overcome. In this chapter, a novel concept for a tunable dual-loop OEO, taking the advantage of using a high-pass filter instead of narrow bandwidth bandpass filters, will be investigated. With this approach, MW signal generation inside K-band with a frequency tuning capability in the GHz range will be presented. It will be furthermore shown that due to small changes in the setup, MW signal generation in the mm-wave region with a tuning range of more than 100 MHz can be achieved.

In contrast to previous works using a long (few kilometers) and a short (few meters) loop [140], the two loop lengths of the novel dual-loop OEO are similar (kilometer range) but not equally long. Because of this, the mode spacing of both loops is close to each other and

thus, the difference in time delay of both loops is even lower than for the conventional dual-loop approach. Nevertheless, the resonance condition given in equation (4.6) above still has to be fulfilled. Thus, just a small change of one loop length will result in the fact that the time delay of this loop changes as well, so that the oscillation frequency f_{osc} of the resonator mode is shifted in order to fulfill the new resonance condition. This way, frequency tuning of the generated signal can be achieved. Beside the frequency tuning capability of the tunable dual-loop OEO, it is another aim to generate high frequency MW signals. Thus, a high-pass filter with a lower cut-off frequency in the GHz-range is needed to suppress lower frequencies which are otherwise also fulfilling the resonance condition.

The block diagram of the novel frequency tunable dual-loop OEO is shown in Figure 4.5. It consists of a single-mode CW laser operating at 1.55 µm wavelength with a subsequent EDFA to boost up the power to the needs of the MZM which is biased at its half-wave voltage V_{π}. A PC is used in front of the MZM to control the polarization state. After the MZM, a second low-noise EDFA is used for adjusting the power level to the requirements of the two PDs. Both PDs (u^2t XPDV2120R) have a 3 dB bandwidth of around 50 GHz and a responsivity of ~0.6 A/W. Before splitting the light with an optical 3 dB power splitter, it will be transmitted through a 7000 m long standard single-mode fiber (SMF 1). A second 2000 m long fiber (SMF 2) is inserted in front of the second photodetector (PD 2). After the first photodetector (PD 1), a phase shifter (PS) with a mechanical adjustment screw (ATM P1608) is used for tuning the frequency of the generated MW signal. The PS allows a phase adjustment of 90° per GHz resulting in a maximum time delay (τ_{el}) of ~250 ps (corresponding length is about 51 mm). Then, the RF output ports from PD 1 and PD 2 are combined and a coaxial high-pass filter with a lower cut-off frequency around 10 GHz is applied. After amplifying the signal with a standard LNA having 26 dB gain and a noise figure of less than 4 dB, the signal is split with an electrical 3 dB power splitter to close the loop on the one hand and to obtain an RF output port on the other hand. The RF output port is connected to an ESA (HP 8565E) for performing measurements.

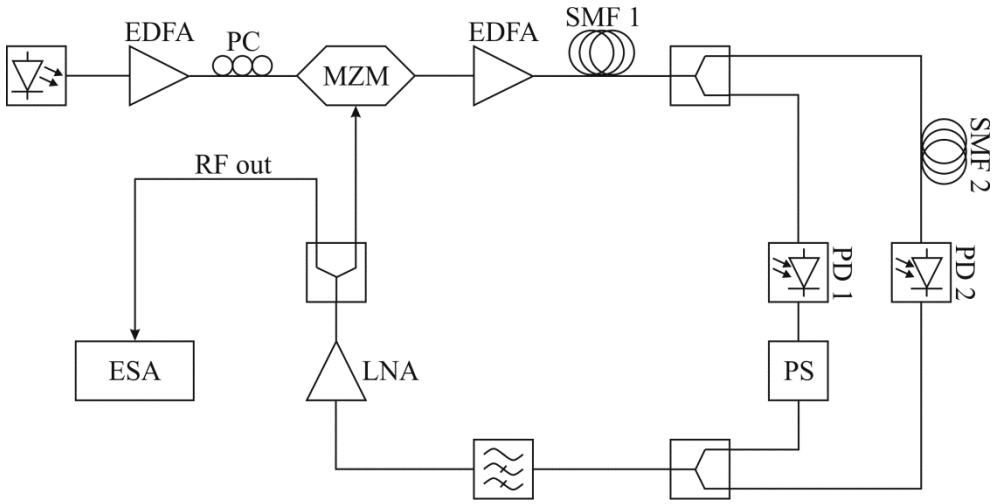

Figure 4.5: Block diagram of the proposed tunable K-band oscillator.

For the experimental characterization, measurements were performed using an ESA connected to the RF output port of the tunable OEO. Figure 4.6 shows an overlay of all the MW signals generated within the frequency range from 20.7-21.8 GHz. It should be noted that for simplicity the individual MW signals are plotted in a single diagram, however, only one mode is present for a given phase shift. The maximum variation of the signal power for the entire frequency range was found to be well below 1 dB between the single MW signals. By changing the phase and therefore the electrical time delay τ_{el} from 0 to 250 ps using the PS, the frequency of the resonator mode is tunable within a frequency range of about ±500 MHz from the central frequency of ~21.3 GHz, thus resulting in a total frequency tuning range of about 1 GHz. It should be mentioned that these frequencies are the second harmonic frequencies resulting from the fact that the MZM is biased at its half-wave voltage. The corresponding fundamental frequencies (about 10.4-10.9 GHz), which are also fulfilling the resonance condition, are not completely suppressed. However, a suppression of more than 30 dB relative to the second harmonic frequencies was observed. Higher order frequencies were not seen on the ESA inside a frequency span from DC to 50 GHz, i.e. the suppression is even higher.

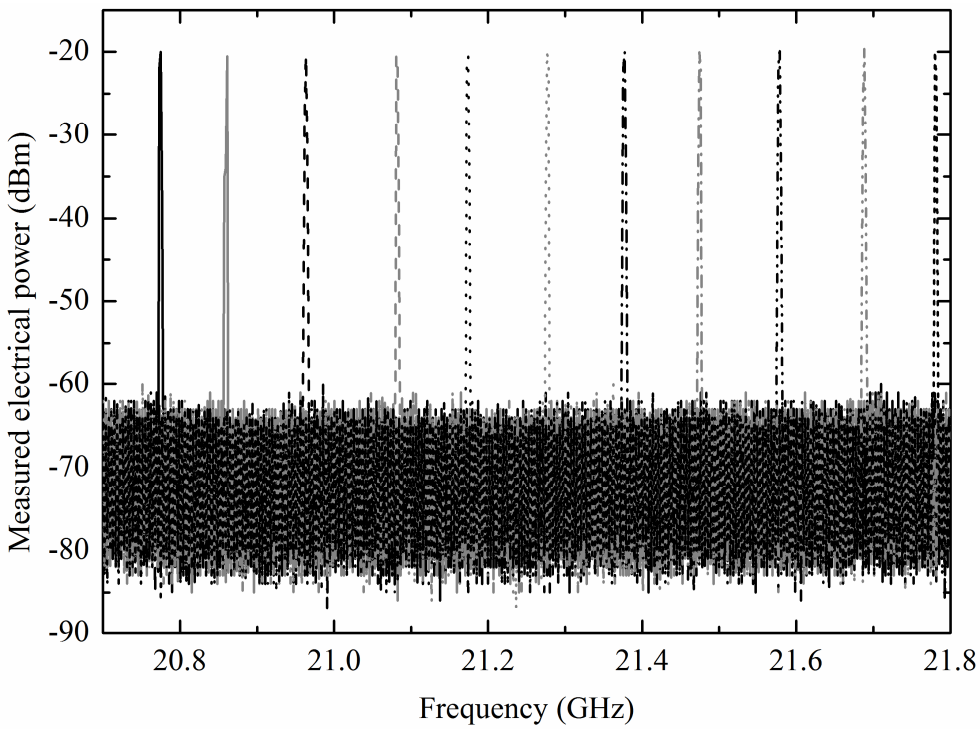

Figure 4.6: Spectrum to show the coarse frequency tunability of the K-band oscillator (Span = 1.1 GHz).

Concerning the limited tuning range there is first of all a trade-off between provided gain inside the loop and single frequency operation. If the gain inside the loop is increased by increasing the optical power (EDFA), also frequencies below 20.7 GHz as well as above 21.8 GHz can be observed, i.e. the threshold condition is fulfilled for many modes and a frequency comb is generated. Thus, the gain has to be adjusted such that the oscillation condition is fulfilled for only one mode (neglecting the fundamental and higher order modes). The lowest achievable frequency is thereby determined by the characteristic of the filter. It is the lowest frequency of the filter where the threshold condition for oscillation on the one hand and the resonance condition on the other hand are fulfilled. Before finding an explanation for the maximum frequency, which then defines in conjunction with the lowest frequency the total frequency tuning range, it is necessary to have a closer look at the tuning behaviour.

From Figure 4.6 it can be seen that the frequency spacing between the individual MW signals is approximately 100 MHz, i.e. that the tuning is not continuously but stepwise. Considering only one individual loop of the K-band OEO, the frequency spacing between the modes, i.e. the FSR ($\Delta\nu_x$) is mainly determined by its length as already shown in formula (4.2). Taking a closer look at the investigated K-band oscillator, where both loop

lengths are similar but not equally long, it is clear that $\Delta\nu_1$ and $\Delta\nu_2$ are close to each other but still different. Assuming that a lowest common multiple ($\Delta\nu_c$) of $\Delta\nu_1$ and $\Delta\nu_2$ exist, particular modes that are separated by $\Delta\nu_c$ match each other's frequency (Figure 4.7) resulting in the fact that only stepwise tuning is possible.

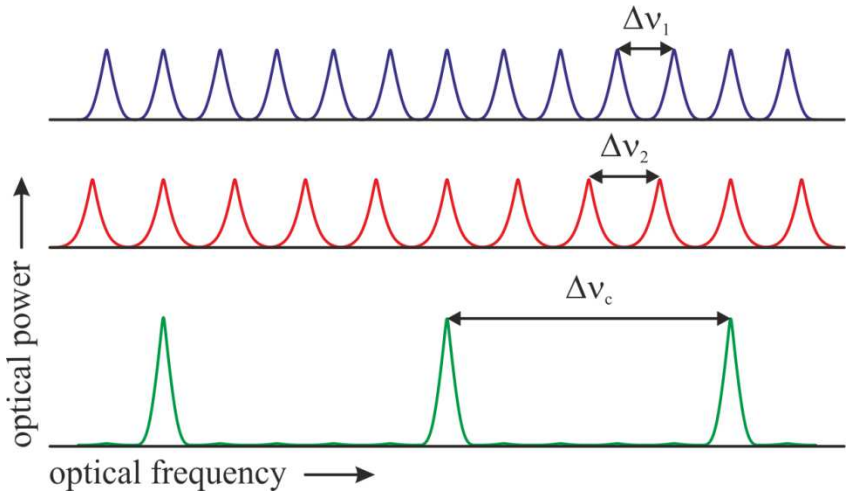

Figure 4.7: Schematic view of the FSR of loop 1, loop 2, and lowest common multiples (effective FSR).

Thus, the lowest common multiple of the FSR from both individual loops is the effective FSR of the dual-loop OEO given as

$$\Delta\nu_c = k \cdot \Delta\nu_1 = m \cdot \Delta\nu_2, \tag{4.9}$$

which is also the oscillation condition for the dual-loop OEO (equation (4.6)).

Based on this, simulations have been performed to get a better knowledge on the tuning resolution as a function of the loop lengths. The fiber lengths were chosen to be similar to the investigated K-band OEO, i.e. the fiber lengths to PD 1 and PD 2 (SMF 2) are fixed at 1.5 m and 2000 m, respectively, while the length of fiber SMF 1, which has an influence on both individual loops, changes from 6998 m to 7002 m in steps of 1 mm. It should be noted that all time delays resulting from components as well as from the electrical paths have been neglected. From the simulation results in Figure 4.8 first of all it can be seen that the lowest common multiple and thus the achievable tuning resolution (effective FSR) strongly depends on the fiber and thus the loop lengths.

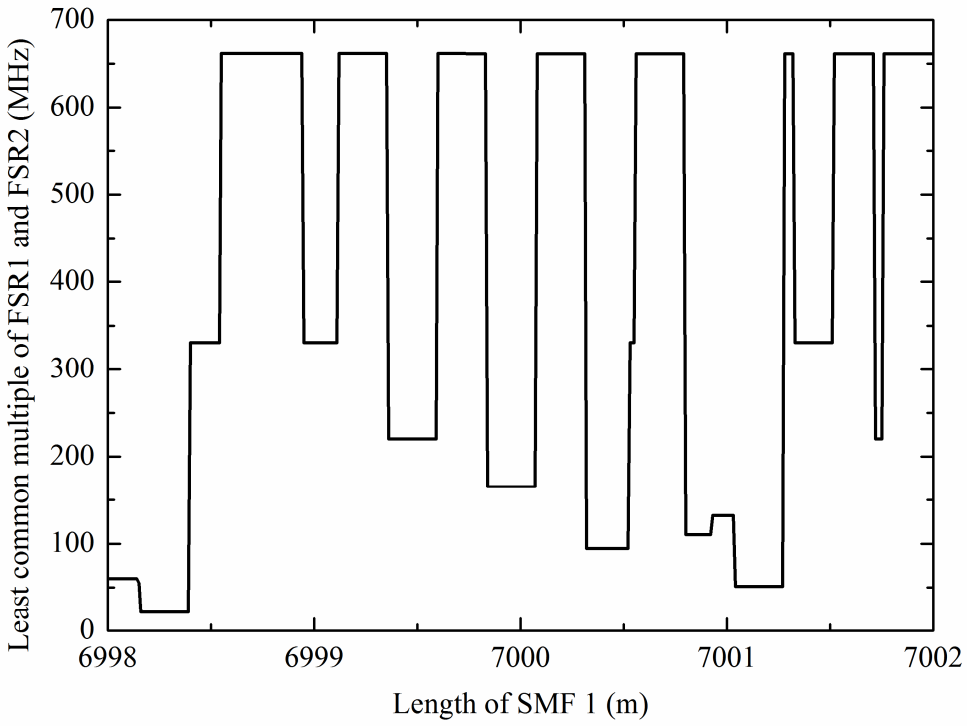

Figure 4.8: Simulation result of the lowest common multiple (effective FSR) vs. fiber length.

Furthermore, it can be seen that the FSR changes abruptly from one value to another. This comes from the fact that for the simulations the FSR of each individual loop was rounded to be an integer (accuracy of 1 Hz), i.e. the FSR versus the length of each individual loop becomes a step function instead of being continuous. Nevertheless, it is expected that a similar behaviour is also true for the investigated K-band OEO because the scheme of superposition of two modes or frequencies (see Figure 4.7) is comparable to optical locking schemes like e.g. OIL where stable locking between two optical frequencies can be achieved even if the two optical frequencies are slightly different, i.e. inside a small region [125]. Thus, it is assumed that in this case there is also a small region where superposition of the two modes occurs even if there is also such a small frequency difference. From the simulation results it can be also seen that an effective FSR and accordingly a tuning resolution of about 100 MHz, similar to the measured results, can be achieved. However, a change of the fiber length of just a few centimeters can drastically influence the tuning resolution if the fiber length is close to the edge where the FSR changes. The highest FSR for a change in fiber length of 4 m is ~660 MHz. It has to be mentioned that there is not only one maximum at ~660 MHz which can be achieved for different fiber lengths, i.e. the longer the fiber, the smaller the maximum FSR. This is due to the fact that if the ratio between the short and the long loop is getting small, which is the case for a very long fiber

(SMF 1), the maximum value of the effective FSR is also getting smaller compared to the case if the ratio between the short and the long loop becomes higher, which means that the length of SMF 1 becomes smaller. As the ratio between the loops of the K-band OEO is small, the change of the maximum value inside the simulated fiber length range is also rather small. Concerning the minimum values also at much higher ratios between the short and long loop very small effective FSRs can be reached but with the disadvantage that the fiber length has to be adjusted very precise because the range where the same FSR is obtained strongly decreases. However, for the investigated K-band OEO the effective loop lengths, also taking into account the additional lengths (time delay) from the components and the electrical path, are also as long as to achieve a tuning resolution of ~100 MHz. Furthermore, due to the fact that the ratio between the short and the long loop is small, it is expected that the additional length of about 51 mm, resulting from the PS, do not influence the fiber length too much that the tuning resolution changes.

The frequency tuning behaviour of the developed K-band OEO is not only limited to the coarse tuning capability as shown above. The frequency of each mode can also be fine-tuned within a frequency range of about ±5 MHz before “hopping” to the next mode. Figure 4.9 shows the frequency fine-tuning capability of the OEO at a sample frequency of about 21.29 GHz. All other obtainable frequencies inside the coarse frequency tuning range have shown similar results. It should be mentioned that not all possible frequencies are shown, i.e. that the frequency resolution is well below 1 MHz. Furthermore, the signal power variation was found to be well below 1 dB as the frequency is tuned.

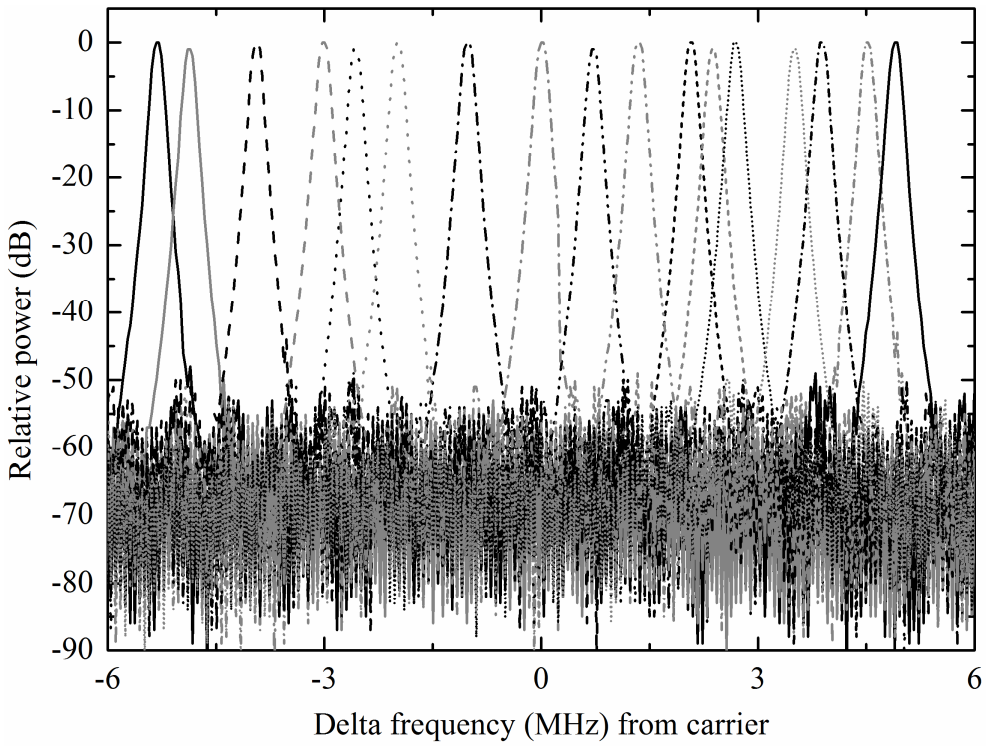

Figure 4.9: Spectrum to show the fine frequency tunability of the K-band oscillator (Span = 12 MHz).

In order to get knowledge about the frequency tuning capability and its limitations, one have to take a deeper look at the theory developed for a mode-locked fiber laser with a composite cavity as presented in [144]. The general structure of the mode-locked laser consists of two sub-cavities of different lengths (composite cavity). Here, so-called supermodes exist which are relying on the principle of the effective FSR described above on the one hand but also on the principle of having so-called periodic frequency windows on the other hand. Due to the feedback loop, the investigated dual-loop OEO forms a resonator similar to the mode-locked fiber laser with composite cavity. Thus, the theory which is valid for the mode-locked laser can be transferred to the OEO. As observed for the laser, it is expected that the comb modes of the OEO are also located inside periodic frequency windows as discussed in the following. By analogy with the theory from the mode locked laser, first of all the transfer function of the dual-loop OEO has to be calculated. As the transfer function is based on the input and output electrical field, it is assumed that the dual-loop OEO is virtually opened at any point before or after the loops are separated (Figure 4.10) [144].

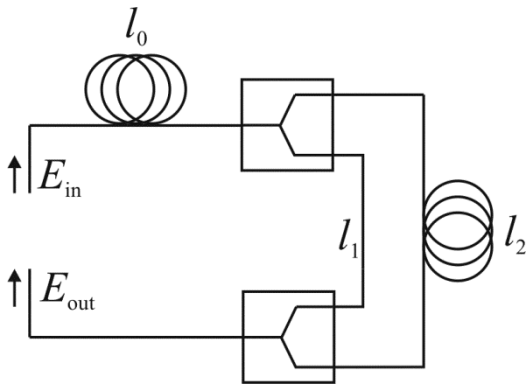

Figure 4.10: Schematic of the virtually opened dual-loop OEO to calculate transfer function.

From the figure it can be seen that the virtually opened dual-loop OEO is in principle similar to a Mach-Zehnder interferometer. Thus, the transfer function is also similar resulting in [144]:

$$T(f) = \frac{1}{2}\left(1 + \cos\left(2\pi f \frac{n_{\mathrm{SMF}} \cdot \Delta L}{\mathrm{c}_0}\right)\right), \tag{4.10}$$

with $\Delta L = (l_0 + l_2) - (l_0 + l_1) = l_2 - l_1$. In order to allow for simple calculating the RF output spectrum of the investigated tunable dual-loop OEO and furthermore to get information about the fine-tuning resolution, $\Delta\nu_{\mathrm{f}}$ and $\Delta\nu_{\mathrm{m}}$ will be introduced as follows. The variable $\Delta\nu_{\mathrm{f}}$, defining the period of the transmittance (see Figure 4.11), is given as

$$\Delta\nu_{\mathrm{f}} = \frac{\mathrm{c}_0}{n_{\mathrm{SMF}} \cdot \Delta L}, \tag{4.11}$$

while $\Delta\nu_{\mathrm{m}}$, describing the distance between two adjacent frequency modes, can be expressed as a function of $\Delta\nu_1$ and $\Delta\nu_2$ using the following relation [144]:

$$\Delta\nu_{\mathrm{m}} = \frac{2\Delta\nu_1\Delta\nu_2}{\Delta\nu_1 + \Delta\nu_2} = \frac{2\mathrm{c}_0}{n_{\mathrm{SMF}} \cdot (2l_0 + l_1 + l_2)}. \tag{4.12}$$

Thus, the transmittance of the tunable dual-loop OEO as a function of the normalized frequency $f_{\mathrm{norm}} = f/\Delta\nu_{\mathrm{m}}$ can be written as

$$T(f_{\mathrm{norm}}) = \frac{1}{2}\left(1 + \cos\left(2\pi f_{\mathrm{norm}} \frac{\Delta\nu_{\mathrm{m}}}{\Delta\nu_{\mathrm{f}}}\right)\right). \tag{4.13}$$

The graphical representation of formula (4.13) for different values of the parameter $\Delta\nu_{\mathrm{f}}/\Delta\nu_{\mathrm{m}}$ is shown in Figure 4.11 [144]. Here, the dashed lines correspond to frequencies, where the transmittance is less than unity. The bold lines indicate frequencies, where the transmittance is unity.

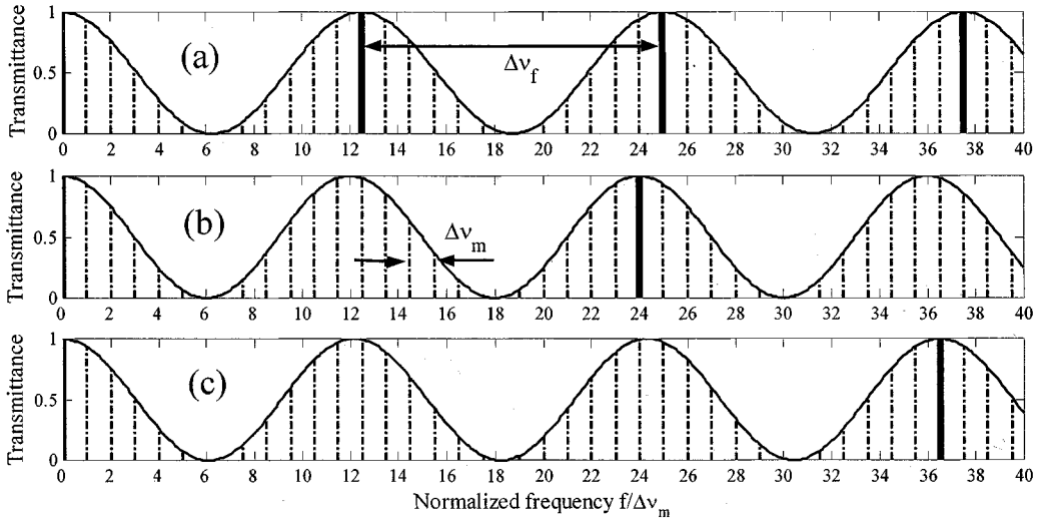

Figure 4.11: Transmittance for different values of the parameter $\Delta\nu_{\mathrm{f}}/\Delta\nu_{\mathrm{m}}$ = (a) 12.5, (b) 12.0 and (c) 12.17. Dashed and bold lines correspond to frequencies of transmittance less than or equal to unity [144].

From the figure it can be seen that depending on the ratio between $\Delta\nu_{\mathrm{f}}$ and $\Delta\nu_{\mathrm{m}}$, not every maximum contains a frequency where the transmittance is equal to unity. Thus, the effective FSR ($\Delta\nu_{\mathrm{c}}$), given in equation (4.9), is not automatically equal to the period of the transmittance. This is only true for the first case (a) shown in Figure 4.11. For the cases (b) and (c) the condition $N \cdot \Delta\nu_{\mathrm{f}} = \Delta\nu_{\mathrm{c}}$ is valid, where N is an integer describing that only every N^{th} period ($N = 2$ for (b) and $N = 3$ for (c)), a frequency with a transmittance of 1 exist. Furthermore, it can be also seen that the period of the transmittance changes, i.e. a frequency shift of the periodic frequency windows occurs, leading to the fact that the another mode (in terms of frequency) reaches a transmittance of 1. A more detailed analysis including all boundary conditions, which was however developed for the mode locked laser with composite cavity, can be also found in [144].

As the period $\Delta\nu_f$ of the present K-band OEO is much smaller than $\Delta\nu_c$, an N of about 925 is calculated when using the same simulation parameters to achieve an effective FSR ($\Delta\nu_c$) of about 100 MHz (see Figure 4.8). This means that just every 925th period of the transmittance comprises a frequency for which the transmittance is equal to 1. Nevertheless, as already described before, the gain was adjusted that only one mode fulfils the oscillation condition at the same time inside the tuning range (neglecting the fundamental and higher order modes). If the phase will be changed by the PS, the change of the N factor and thus the effective FSR is negligible as the corresponding change in length is too low. However, a frequency shift of the periodic frequency windows as well as a small change of $\Delta\nu_m$, which is rather low, is observed. Thus, it is expected that due to the frequency shift either the adjacent frequency next to the oscillating frequency inside the same frequency window or a frequency inside another nearby frequency window now fulfils the oscillation condition while the original oscillating frequency will stop oscillating. Thus, the lowest possible fine-tuning resolution of about 25.5 kHz for the K-band OEO, is thereby determined by the distance between the adjacent frequencies ($\Delta\nu_m$). If the phase will be further changed, it can also happen that the next frequency fulfilling the oscillation condition is another frequency inside the coarse tuning range (N times $\Delta\nu_f$ away from the actual frequency). Thus, the mode (in terms of frequency) jumps inside the coarse tuning range. For the limited coarse tuning range of the investigated K-band OEO it is has been observed that if the frequency which is 1 GHz above the lowest frequency is reached, the next adjustable frequency is again located inside the coarse tuning range, i.e. frequencies higher than about 21.8 GHz cannot be reached. Thus, it is expected that even if the oscillation condition is in principle fulfilled for a higher frequency (above ~21.8 GHz), at the same time it is also fulfilled for a frequency inside the present tuning range such that the lower frequency will start oscillation.

A direct comparison between simulation and measurement has been performed in order to prove that the theory described above, which was originally developed for the mode locked laser with composite cavity, can be transferred to the tunable dual-loop OEO approach. For the measurements, the same setup as shown Figure 4.5 was used but with a small modification of having an additional optical power combiner right after the MZM in order to allow for injecting an optical heterodyne signal into the loop. The loop lengths were chosen to be smaller because of the much broader FSR which allows an easier visualization of the different frequencies on the electrical spectrum analyzer. The lengths

of the fibers SMF 1, SMF 2 are about 45 m and 4 m, respectively, while the fiber to PD 1 is about 2 m. Figure 4.12 shows the simulation results using these fiber lengths.

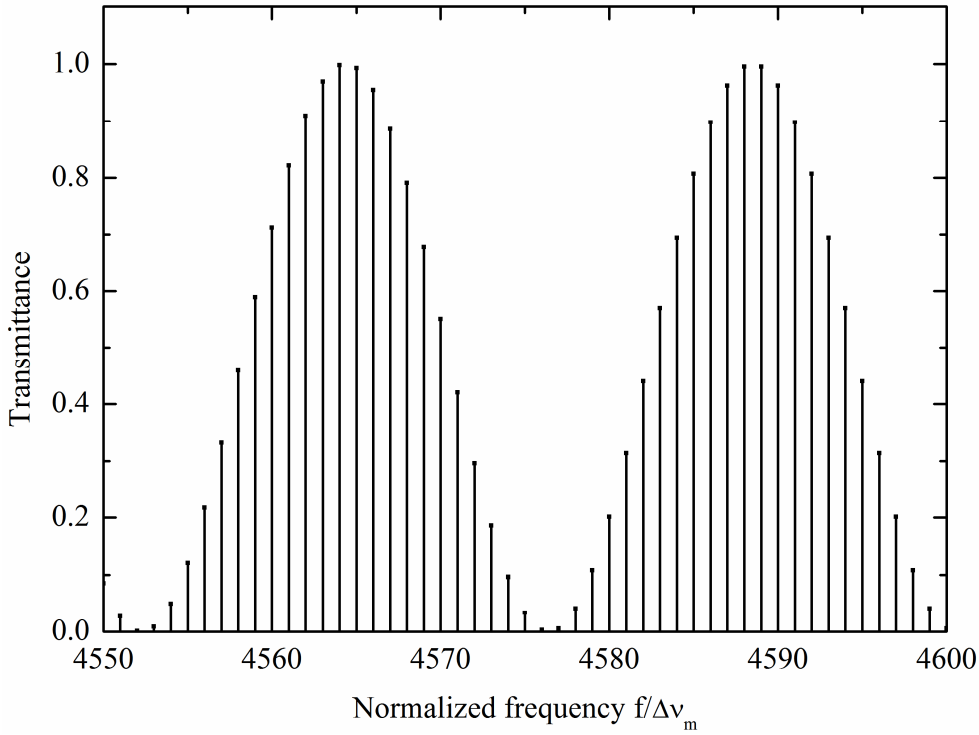

Figure 4.12: Simulation result of the RF spectrum showing the frequency windows.

From these results one can clearly observe the frequency windows. The period of the transmittance ($\Delta\nu_{\mathrm{f}}$) was calculated to be about 102 MHz while the distance between two adjacent frequency modes ($\Delta\nu_{\mathrm{m}}$) was calculated to be about 4.2 MHz.

For comparison reasons, measurements have been performed showing the capability of generating MW signals with frequencies around 18.3 GHz. With the aim to visualize the frequency windows, a frequency tunable heterodyne signal with a constant optical power of about -20 dBm was injected into the loops through the optical power combiner. Using this approach, also modes where the threshold condition for achieving oscillation is not fulfilled can be made viewable as the heterodyne signal provides additional power (gain) to the mode. At first, the difference frequency of the heterodyne signal was adjusted to be inside the frequency tuning range of the OEO. Then the heterodyne frequency was continuously changed inside the frequency tuning range of the OEO while the optical power was kept constant. The RF output signal of the tunable dual-loop OEO was measured with the ESA using the max-hold function. Thus, the ESA stores all measured

points and displays all frequencies. Figure 4.13 shows the measurement result of the generated RF spectrum of the tunable dual-loop OEO. The RF output power is normalized to 0 dB and the frequency axis is normalized to $f/\Delta\nu_{\mathrm{m}}$, where $\Delta\nu_{\mathrm{m}}$ was measured to be ~4 MHz.

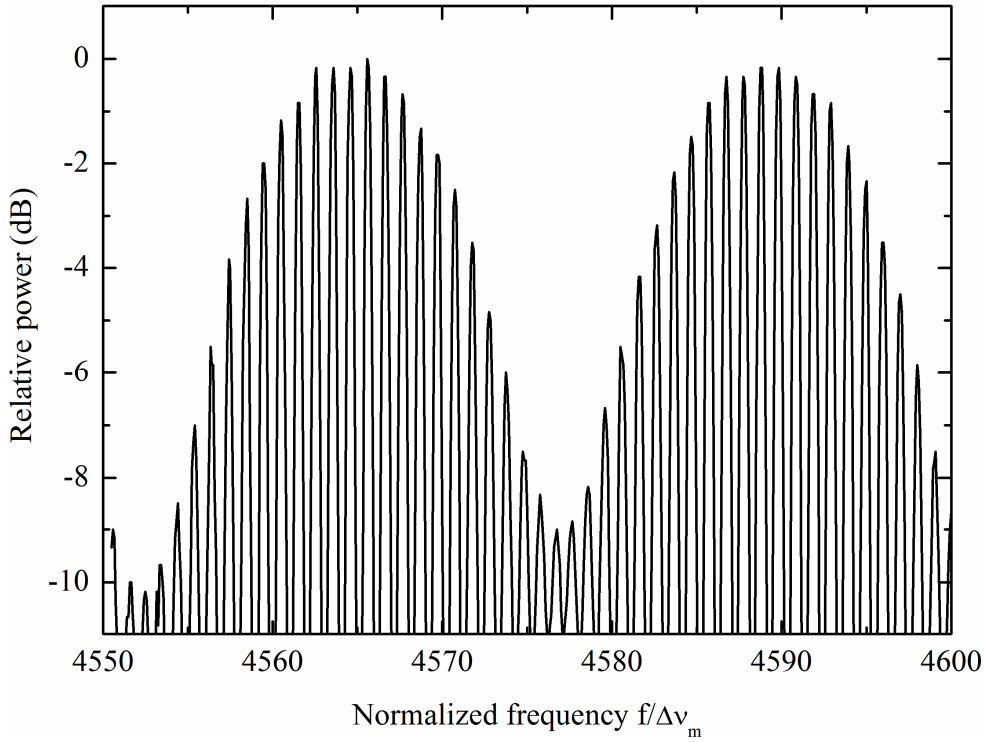

Figure 4.13: Measurement result of the RF spectrum showing the frequency windows.

From the measurement results one can clearly see the periodic frequency windows, similar to the simulation results in Figure 4.12, verifying that the theory of the mode-locked fiber ring laser with composite cavity is also valid for the investigated dual-loop OEO. Nevertheless, compared to the simulations where the transmittance changes between 0 and 1, here the minimum is just about 10 dB lower than the maximum, corresponding to a minimum transmittance of 0.1. This is due to the fact that, although the power of the injected optical heterodyne signal was chosen to be relatively small (about -20 dBm), the gain for each mode (in terms of frequency) is strong enough to allow oscillation such that it can be seen at the RF output port. In order to prove the theory about the tuning behaviour, the length of one loop has been also changed using a phase shifter. Here, a frequency shift of the periodic frequency windows (cf. Figure 4.11) as well as a small change of the FSR has been observed confirming the working principle of the tunability of the dual-loop OEO as already described above.

In order to get a deeper knowledge about the spectral-purity and to determine the spectral linewidth, i.e. the FWHM of the generated MW signal, a zoom-in view of the electrical output spectrum has been measured. Figure 4.14 shows the output spectrum of the generated MW signal at a sample frequency of about 21.29 GHz.

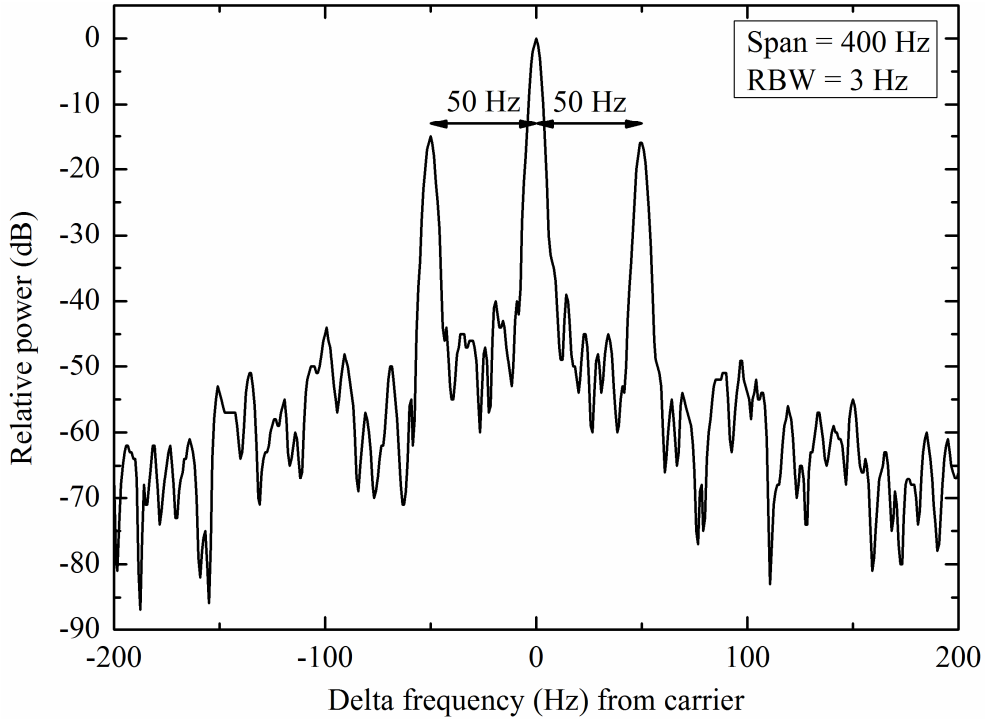

Figure 4.14: Measurement of one single frequency (21.29 GHz) to determine the FWHM (all other frequencies inside the tuning range are similar).

One can observe two side modes close to the carrier with a difference frequency of exactly 50 Hz. Additional measurements have confirmed that these modes are due to the ac power sources used on all the voltage supplies. To avoid this, one can imagine using sources with integrated 50 Hz filters or batteries. To measure the FWHM of the generated microwave signal, the span and resolution bandwidth (RBW) of the ESA were set at 400 Hz and 3 Hz, respectively. The measured FWHM of the carrier signal is as small as 3 Hz, which is also the minimum RBW of the ESA. It is also observed that both the signal amplitude and the frequency of the microwave signal are very stable. Over a duration of about 2 hours, the maximum observed RF power variation was less than 0.2 dB for all observed frequencies. Also the frequency drift was rather small; the maximum frequency drift measured within two hours was less than 1 kHz. This reflects that the locking between both loops is stable and phase correlated. It is worth mentioning that the above measurements were carried out

at room temperature in a laboratory environment. Additional measurements carried out in an oven at higher temperatures up to 50° Celsius revealed that while the temperature is changed, also the mode "jumps", but only within the fine tuning range of ±5 MHz. Once the temperature is stable, even at 50° Celsius, the frequency stability and tuning range are equal to those at room temperature.

For further studying the quality of the generated MW signal, the SSB phase noise has been measured using the ESA. The experimental result for a carrier frequency of ~21.29 GHz and the system's measurement noise floor are shown in Figure 4.15.

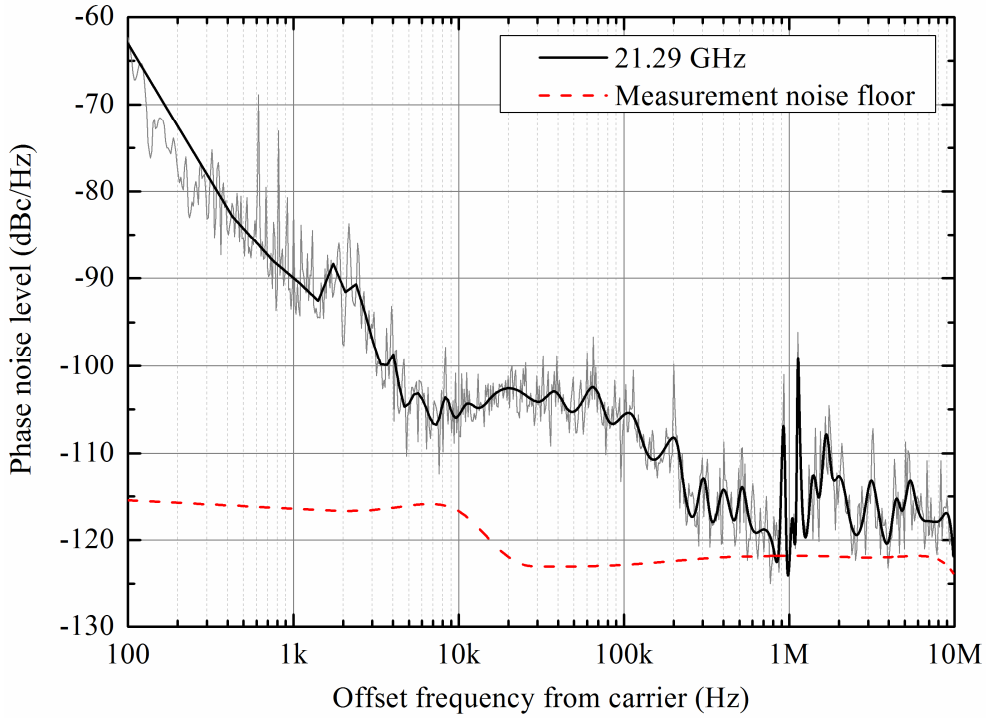

Figure 4.15: Phase noise measurement of a sample frequency of 21.29 GHz and measurement noise floor. Other frequencies inside the tuning range have shown similar results with a maximum deviation of ±1.5 dB.

As can be seen, the phase noise of the generated signal is about -105 dBc/Hz at 10 kHz offset from the carrier. Given that the relative intensity noise of the DFB laser used was -145 dB/Hz, it is expected that the intensity noise contributions are small (see also chapter 4.1). From the figure, it can be seen that the measured phase noise at high offset frequencies is limited by the measurement noise floor. Furthermore, at offset frequencies around 1 MHz, higher peaks are observed. It is expected that these peaks can be traced back to the fact that the modes inside the fine-tuning range are not completely

suppressed. Nevertheless, the influence on the phase noise performance of these peaks is rather small. For all other achievable frequencies, the maximum phase noise deviation was found to be below ±1.5 dB.

To bring the generated MW signal into the mm-wave range, the setup shown in Figure 4.5 was slightly changed [T]. The filter was replaced with a custom design high-pass filter providing a lower cut-off frequency of ~15 GHz instead of the 9 GHz as used for the K-band OEO. Due to the fact that first experiments have shown that the oscillation was not stable, i.e. the MW signal was alternately present and absent it was expected that the threshold condition could not be fulfilled which means that the small signal open-loop gain was just under unity. As both, the optical (EDFA) and the electrical gain (LNA) were limited, the fiber lengths were decreased to slightly minimize the losses and thus to achieve stable oscillation. The 7000 m long SMF 1 was replaced by a 4000 m long one while the second one (SMF 2) was replaced by a 500 m long SMF. With these modifications, stable tunable MW signal generation with a central frequency of nearly 50 GHz has been achieved. Figure 4.16 shows an overlay of the measured single-frequency output spectra at a central frequency of around 49.5 GHz. Here, it has to be mentioned that these frequencies are the third harmonic frequencies, i.e. three times the fundamental frequency. The bias voltage of the MZM was adjusted to achieve as much power as possible to the third harmonic frequency. However, as a consequence the fundamental frequency is not compressed but more than 30 GHz away from the desired frequency.

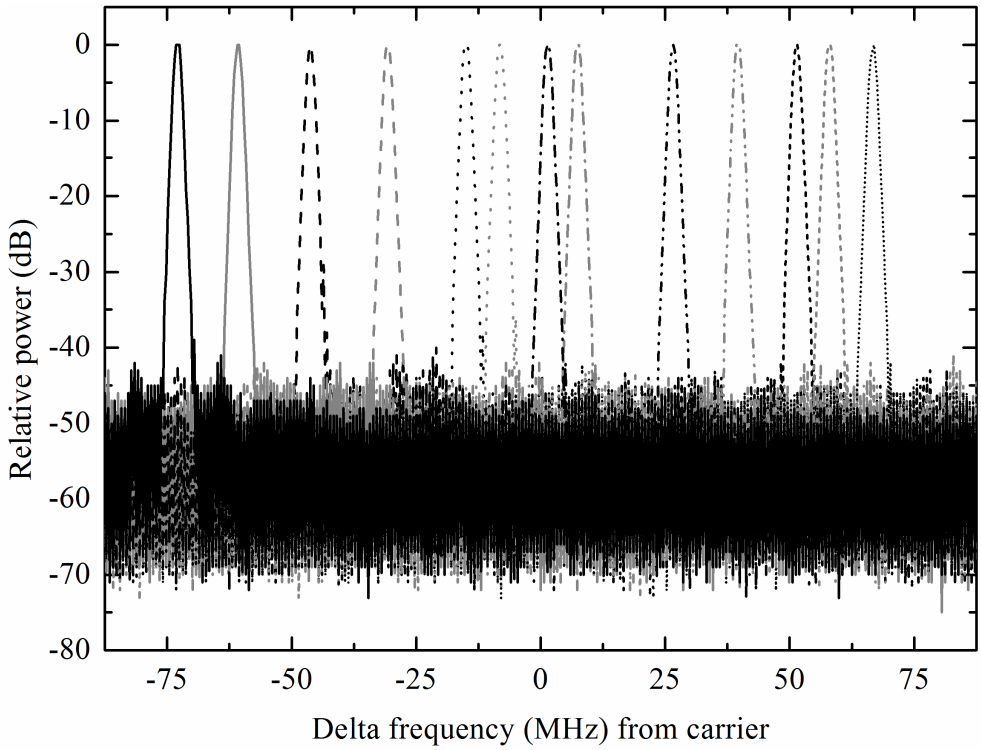

Figure 4.16: Spectrum to show the frequency tunability of the 50 GHz OEO (Span = 175 MHz).

The frequency can be tuned within a frequency range of about ±75 MHz by adjusting the phase and thus the electrical time delay using the PS. Here, also not all possible frequencies are shown, resulting in the fact that the tuning resolution is well below 10 MHz. The signal power variation between the different frequencies is also below 1 dB as the frequency is tuned.

Figure 4.17 gives a zoom-in view of the measured electrical output spectrum at a sample frequency of ~49.48 GHz, showing the high spectral purity of the desired frequency. The RBW of the ESA was set at 100 kHz and the span at 10 MHz. All other frequencies inside the tunable span have shown the same output spectrum.

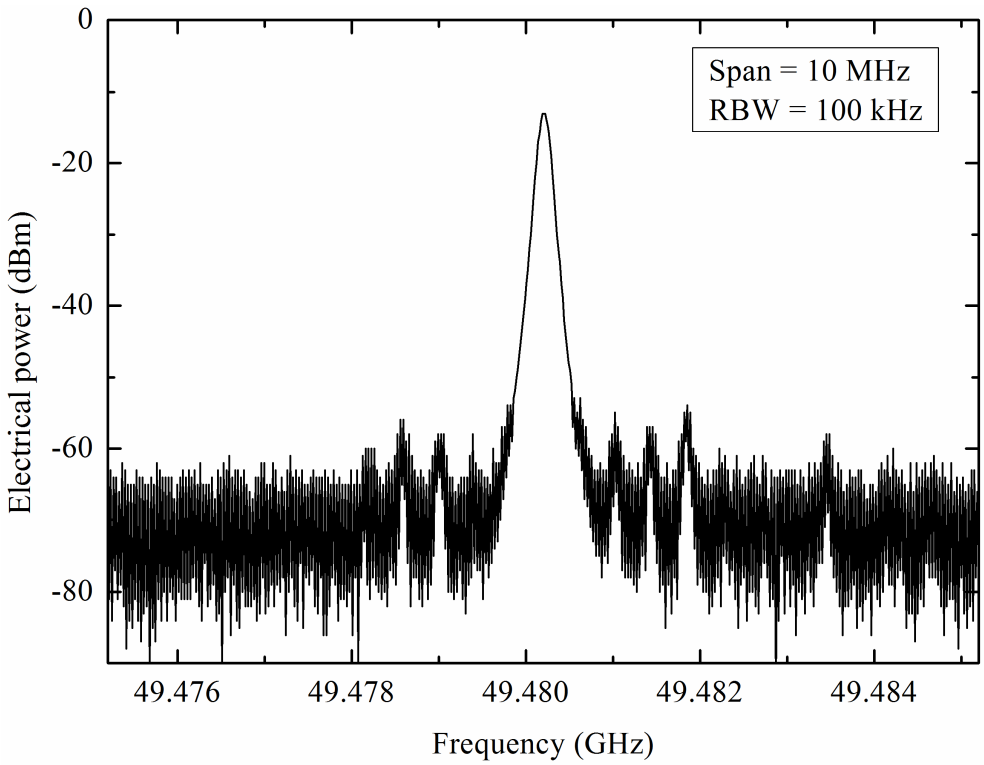

Figure 4.17: Experimental data for the OEO output taken at a sample frequency of ~49.48 GHz (all other frequencies are similar).

From the figure, one can see some “ripples” near the carrier frequency. These frequency components are supposed to be due to the not fully suppressed modes which result from the 500 m difference in length between both loops. The calculated period of the transmittance ($\Delta\nu_f$), which is defined by this difference (see equation (4.11)), is approximately 400 kHz. As the observed frequency components shown in the figure are exactly multiples of about 400 kHz, it is expected that they can be attributed to the difference of the lengths between both loops. This means that the modes (in terms of frequency) located inside the period of the transmittance are not fully suppressed.

In order to investigate the signal quality more detailed, the SSB phase noise of the output signal taken from the electrical output port was measured. The result of a sample frequency of ~49.5 GHz is shown in Figure 4.18.

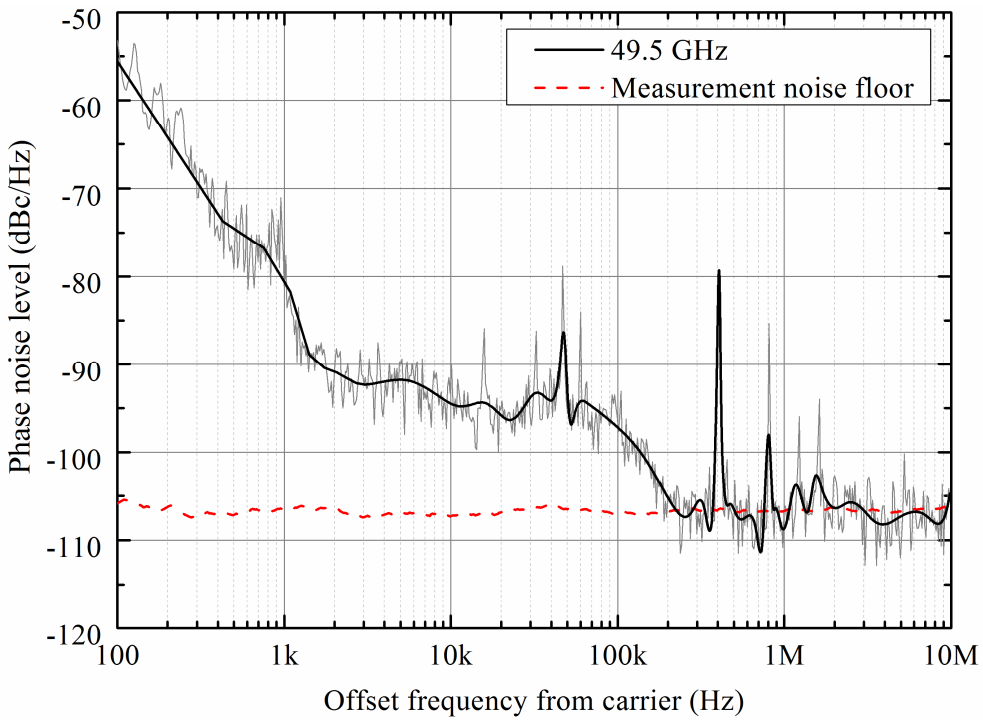

Figure 4.18: Phase noise measurement of a sample frequency of 49.5 GHz and measurement noise floor. Other frequencies inside the tuning range have shown similar results with a maximum deviation of ±1.5 dB.

The phase noise of the generated signal inside the tuning range is about -95 dBc/Hz at 10 kHz offset from the carrier. Phase noise measurements were also performed for all other frequencies shown in Figure 4.16. The maximum phase noise deviation was the same as for the previous setup, i.e. ±1.5 dB. It should be noted that the 50 GHz OEO was free-running, and no further efforts were made to reduce the phase noise. As already described above, one can observe the frequency components as strong peaks at multiples of ~400 kHz offset from the carrier.

In chapter 3.2.2, it has been shown that phase noise measurements using an ESA are affected by the measurement setup itself. In order to get a better knowledge on how the contributions of the measurement setup will affect the phase noise, simulations have been performed based on the theory developed in [138], [139] and [142]. Figure 4.19 shows a comparison between the measured phase noise results and a corresponding simulation using equation (4.7) in chapter 4.2.

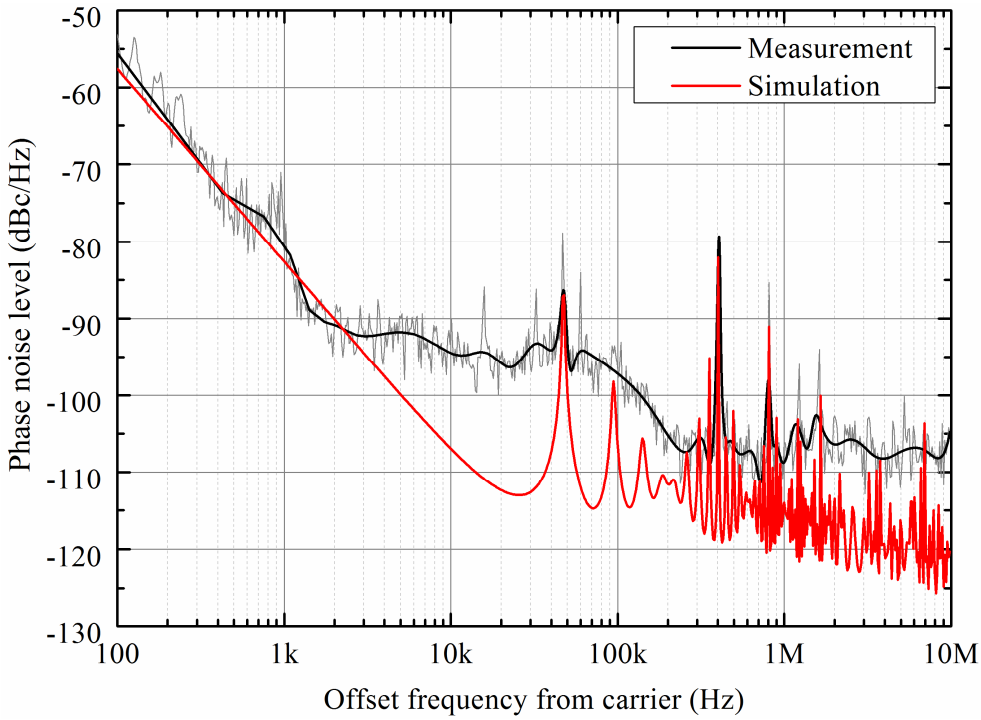

Figure 4.19: Phase noise comparison between measurement and simulation.

From the simulation results, one can also clearly see the peaks mentioned before. Although there is a deviation inside the offset frequency range between 3 kHz up to 10 MHz and although the peaks are not as high as from the measurement, it can be stated that the simulation results agree reasonably well with the measured spectrum except for the offset frequency range from about 3 kHz up to 200 kHz. At offset frequencies above ~200 kHz, the measured phase noise saturates due to the measurement noise floor (see also Figure 4.18) while the simulated phase noise further decreases. The deviation inside the offset frequency range between 3 kHz and 200 kHz can principally be traced back to the influence of the measurement setup using an ESA as a phase noise measurement using an ESA is an “all-noise” measurement, i.e. amplitude and frequency fluctuations as well as noise contributions from the ESA and the measurement setup itself are influencing the phase noise measurement (see phase noise theory in chapter 2.6 and measurement results in chapter 3.2.2). Nevertheless, it can be stated that the simulation environment is capable of predicting the phase noise spectrum very close to reality. Thus, it can be used to calculate and optimize the system’s phase noise performance by changing parameters or components like e.g. the laser (RIN noise).

The intention of this chapter was to investigate possibilities which are able to generate high frequency tunable MW signals with low phase noise without the need for any electrical reference oscillator. It has been shown that in principle an OEO is suited as it has the ability to generate MW signals with ultra-low phase noise. However, the frequency tunability of an OEO is very limited mainly due to the need for an ultra-narrow bandwidth bandpass filter. To overcome this limitation, a novel approach based on a dual-loop OEO with similar but not equally long loops and replacing the bandpass filter with a standard high-pass filter was presented in this chapter. For frequency tuning an electrical phase shifter, which introduces an effective length change of one loop, was used. With this approach a tuning range exceeding one GHz around a central frequency of 21.2 GHz has been experimentally demonstrated. For an OEO it is the first time that such a wide frequency tuning range has been achieved without the need for several bandpass filters or complex tunable bandpass filters as required in previous works. Within the whole tuning range, the phase noise at 10 kHz offset from the carrier was found to be -105 dBc/Hz. Furthermore, the phase noise and output power of the generated MW signal only varies by ±1.5 dB and 1 dB, respectively. By improving the developed dual-loop OEO, the central frequency could be increased to be about 50 GHz. Here, a frequency tunability of more than 100 MHz and a phase noise of -95 dBc/Hz at 10 kHz offset from the millimeter-wave carrier have been achieved. As the phase noise as well as the tuning resolution is strongly related to the loop lengths and thus the corresponding time delay, there is still some space for improvements. However, it has to be mentioned that the time delay is not only affected by the long fibers but also by every fiber used for the connections, every component as well as the time delay resulting from the electronics (components and RF cables) which result in a change of the effective fiber lengths and just to a change of the tuning resolution. This makes it is hard to realize exact time delays for each loop just by choosing the lengths of the fibers. Nevertheless, compared to the phase noise performance of the external modulation approach presented in chapter 3, providing a phase noise level of -76 dBc/Hz at 10 kHz offset from a 50 GHz carrier, an improvement of 19 dB has been achieved without any optimizations in loop lengths. Although OEOs presented previously by other groups [138]-[143] have shown better phase noise performances, the proposed technique has the advantage of a high tuning range without using a set of bandpass filters or a tunable laser where the tuning range was limited to less than 2 MHz. Furthermore, it should be noted that the central frequencies of the previously studied OEOs were just around 10 GHz.

5 Conclusion

The aim of this work was to theoretically and experimentally study the generation of low phase noise and frequency tunable micro- and millimeter-wave signals using photonic techniques. Novel and innovative microwave photonic techniques and advanced photonic technologies have been invented to develop photonic synthesizers that enable the generation of high frequency micro- and millimeter-wave signals with outstanding performances in terms of phase noise and ultra-wide frequency tunability.

The theoretical background of the key optical components and the various microwave photonic techniques studied in this thesis have been presented in the second chapter of this work. Theoretical details about lasers, common external modulation techniques, nonlinearities in semiconductor optical amplifiers, optical fiber propagation, photodetection, and noise in photonic synthesizers have been analyzed. Based upon these mathematical descriptions, a time-domain simulation model has been implemented in MATLAB®. By employing a fast Fourier transformation, this simulation model allows to theoretically study the spectral output signal of photonic synthesizers based upon external optical multiplication and thus, it allows to theoretically study important system performances such as the conversion efficiency and the achievable optical multiplication factor.

In order to enable an ultra-wide frequency tuning range, photonic micro- and millimeter-wave signal generation based upon optical heterodyning has been studied in chapter 3.1. Photonic millimeter-wave signal generation with ultra-wideband (W-band) and broadband (30 kHz-110 GHz) frequency tuning ranges has been successfully achieved using two free-running single-mode lasers and advanced photodetectors. In both cases, the frequency of the generated millimeter-wave signal can be tuned in a continuous manner, with a minimum frequency resolution less than 125 kHz. For W-band operation, a frequency tuning range of 69-112 GHz, a saturated maximum output power of 0 dBm, a 1 dB compression point of about -4 dBm, and a dynamic range of 32 dB have been achieved. For broadband operation, continuous frequency tunability within 30 kHz to 110 GHz with a power roll-off of less than 6 dB and a maximum output power of about -3 dBm have been demonstrated. These achievements clearly indicate that the developed photonic synthesizer concepts based on optical heterodyning are predestinated for high frequency

signal generation with extremely wide frequency tuning ranges. In comparison to all-electronic synthesizers based upon quartz reference oscillators, the photonic synthesizer concept based upon optical heterodyning is advantageous as it not only allows the generation of high-frequency signals with extremely wide frequency tuning ranges without the need for complex electronic-multiplier chains but also the low-loss transport of the high-frequency signals in the optical domain using optical fibers.

As shown in chapter 3.1, the phase noise of the millimeter-wave signal generated by optical heterodyning depends on the locking stability between the two optical modes and consequently, the phase noise performance using two free-running lasers is somewhat limited. Thus, for generating high frequency signals with a very low phase noise, the optical modes must be phase locked. Here, a good choice is to use external optical modulation as in this case, the optical modes are generated from only one laser source. In chapter 3.2, photonic millimeter-wave signal generation using an external Mach-Zehnder modulator biased at its half-wave voltage to achieve a double-sideband signal with carrier suppression has been presented. Using this scheme, frequency tunable high frequency millimeter-wave signal generation inside W-band with low phase noise performance has been achieved. At a carrier frequency of 100 GHz, a phase noise level of about -70 dBc/Hz at 10 kHz offset has been experimentally demonstrated. As shown in chapter 3.2, the external modulation approach allows optical generation of high-frequency signals well in the millimeter-wave range with ultra-wide frequency tuning ranges and low phase noise and it furthermore enables low-loss signal transport in the optical domain. However, the demonstrated external modulation approach still requires an electronic reference oscillator with a wide frequency tuning range. This not only increases complexity and cost, but the required frequency tuning range and phase noise is not easily achieved by electronic oscillators.

In order to reduce the performance requirements of the electronic reference oscillator in a first step, an optical multiplication scheme based on external modulation in conjunction with a highly nonlinear semiconductor optical amplifier has been studied. By using nonlinear optical frequency multiplication, the requirements on the carrier frequency and the frequency tuning range of the electronic reference oscillator have successfully been relaxed. Within this work, which has been part of the European Space Agency tender “PHOMIGEN”, an eight times optical multiplication of the fundamental frequency

provided by the reference oscillator has been achieved by using one Mach-Zehnder modulator in conjunction with a highly nonlinear semiconductor optical amplifier. Based upon this approach, a low frequency signal from a reference oscillator was successfully up-converted to a millimeter-wave signal. Furthermore, it has been experimentally shown that although additional noise sources such as relative intensity noise from the utilized laser and shot noise from the employed photodetector are present, their contributions on the phase noise of the generated signal are negligible. Thus, it could be shown that the phase noise of the generated millimeter-wave signal is proportional to the phase noise of the employed reference oscillator and is only degraded by a factor of $20 \cdot \log(N)$, where N is the optical multiplication factor.

As already mentioned above, the phase noise performance of an optically generated signal using external modulation approach is strongly related to the phase noise performance of the employed reference oscillator. To overcome this phase noise limitation, the use of any electrical reference oscillator has to be avoided. With the intention to develop a photonic approach that does not require the use of any electronic reference oscillator, a novel optical oscillator concept has been invented. This new concept, which is described in chapter 4, makes use of an optoelectronic feedback loop for generating frequency tunable micro- and millimeter-wave signals with ultra-low phase noise performance. In general, the invented new concept is based upon a dual-loop optoelectronic oscillator concept, but in contrast to previous works, the lengths of the two optoelectronic feedback loops were designed to be similar but not exactly equally long. This results in the fact that the time delay difference between the two feedback loops is much lower as compared to conventional dual-loop approaches. Nevertheless, it has been shown that the resonance condition as for the conventional dual-loop optoelectronic oscillators can be fulfilled. Thus, even a small change of one optoelectronic loop length results in the fact that the time delay difference changes while the resonance condition is still fulfilled, yet for another oscillation frequency. Thus, the developed approach enables frequency tuning even for small changes of the length of one of the feedback loops. In the work presented here, this has been achieved by using an electrical phase shifter to change the time delay of one feedback loop in conjunction with a standard high-pass filter. Experimentally, a tuning range exceeding one GHz at a central frequency of 21.2 GHz has been successfully demonstrated without the need for several bandpass filters or complex tunable bandpass filters required in previous works. It is the first time that such a wide frequency tunability has been achieved

using an optoelectronic oscillator. The linewidth and phase noise of the generated MW signal are <3 Hz and -105 dBc/Hz at 10 kHz offset from the carrier within the whole tuning range, respectively. Within the full gigahertz tuning range, the phase noise and output power of the generated microwave signal varies only by 1.5 dB and 1 dB, respectively. Furthermore, by improving the developed dual-loop optoelectronic oscillator, the central frequency could be increased to the millimeter-wave region. Experimentally, a millimeter-wave signal with low phase noise of -95 dBc/Hz at 10 kHz offset from a 50 GHz carrier and a frequency tunability of more than 100 MHz has been achieved. In comparison to the phase noise performance of the external modulation approach presented in chapter 3, providing a phase noise level of -76 dBc/Hz at 10 kHz offset from a 50 GHz carrier, an improvement of 19 dB has been achieved. It should be mentioned that even better phase noise performances can of course be achieved by using an optoelectronic oscillator for fixed frequency generation. It should furthermore be mentioned that the central frequency of previously studied frequency tunable optoelectronic oscillators using a set of bandpass filters or a tunable laser were just around 10 GHz and the frequency tuning range was limited to less than 2 MHz.

In summary, novel and advanced microwave photonic approaches, as well as new photonic technologies for the generation of ultra-wide frequency tunable and low phase noise micro- and millimeter-wave signals have been studied in this work. Advanced photonic approaches utilizing external optical modulation and optical multiplication offering superior high frequency optical millimeter-wave generation with extremely wide frequency tuning ranges and low phase noise characteristics have been studied theoretically and successfully demonstrated experimentally. To further improve the phase noise of the optically generated high frequency signals and to avoid the use of any electrical reference oscillator, a novel similar-length dual-loop optoelectronic oscillator was invented and experimentally demonstrated. Signal generation well in the millimeter-wave frequency region and tuning ranges in the gigahertz range were experimentally demonstrated for the first time using a dual-loop optoelectronic oscillator.

6 References

[1] J. Yao, "Microwave Photonics," *J. Lightw. Technol.*, vol. 27, no. 3, pp. 314-335, 2009.

[2] D. Jäger and A. Stöhr, "Microwave Photonics – From Concepts to Applications," *GeMiC,* pp. 136-139, 2005.

[3] A. Stöhr, "Pushing the boundaries," *IEEE Microwave Magazine*, vol. 10, no. 4, pp. 106-115, June 2009.

[4] A. T. Forrester, R. A. Gudmundsen, and P. O. Johnson, "Photoelectric Mixing of Incoherent Light," *Phys. Rev.*, vol. 99, no. 6, pp. 1691-1700, 1955.

[5] M. Chamberland, M. Tetu, and P. Tremblay, "Spectral characterization of microwave signals generated by the heterodyne of injection-locked semiconductor lasers," *Proc. SPIE*, vol. 2155, Optoelectronic Signal Processing for Phased-Array Antennas IV, 41, 1994.

[6] L. Morvan, D. Dolfi, J.-P. Huignard, S. Blanc, M. Brunel, M. Vallet, F. Bretenaker, and A. Le Floch, "Dual-frequency laser at 1.53 µm for generating high-purity optically carried microwave signals up to 20 GHz," *in proceedings of OSA Conference on Lasers and Electro-Optics*, 2004.

[7] G. Pillet, L. Morvan, M. Brunel, F. Bretenaker, D. Dolfi, M. Vallet, J.-P. Huignard, and A. Le Floch, "Dual-Frequency Laser at 1.5 µm for Optical Distribution and Generation of High-Purity Microwave Signals," *J. Lightw. Technol.*, vol. 26, no. 15, pp. 2764-2773, 2008.

[8] G. Pillet, L. Morvan, D. Dolfi, J. Schiellein, and T. Merlet, "Stabilization of new generation solid-state dual-frequency laser at 1.5 µm for optical distribution of high purity microwave signals," ," *Int. Topical Meeting on Microwave Photonics*, Oct. 5-9, Montreal, Canada, 2010.

[9] M. Al-Mumin, C. Kim, I. Kim, N. Jaafar, and G. Li, "Injection locked multi-section gain-coupled dual mode DFB laser for terahertz generation," *Optics Comm.*, vol. 275, pp. 186-189, 2007.

[10] G. Qi, J. P. Yao, J. Seregelyi, C. Bélisle, and S. Paquet, "Optical generation and distribution of continuously tunable millimeter-wave signals using an optical phase modulator," *J. Lightwave Technol.*, vol. 23, no. 9, pp. 2687-2695, Sep. 2005.

[11] T. Wang, M. Chen, H. Chen, and S. Xie, "Millimeter-Wave Signal Generation Using Four-Wave Mixing Effect in SOA," *in National Fiber Optic Engineers Conference, OSA Technical Digest Series*, paper JThA59, 2007.

[12] P. Paulus, R. Langenhorst, and D. Jäger, "Stable Pulsations of Semiconductor Lasers by Optoelectronic Feedback with Avalanche Photodiodes," *Electron. Lett.*, vol. 13, no. 9, pp. 471-472, 1987.

[13] S. Huang, L. Maleki, and T. Le, "A 10 GHz Optoelectronic Oscillator with Continuous Frequency Tunability and Low Phase Noise," *IEEE Trans. Freq. Contr. Symp.*, pp. 720-727, 2001.

[14] S. Poinsot, H. Porte, J.-P. Goedgebuer, W. T. Rhodes, and B. Boussert, "Continuous radio-frequency tuning of an optoelectronic oscillator with dispersive feedback," *Optics Letters*, vol. 27, no. 15, pp. 1300-1302, 2002.

[15] T. Schneider "Nonlinear Optics in Telecommunications (Advanced Texts in Physics)," *Springer*, 2004.

[16] K. Petermann, "Laser Diode Modulation and Noise (Advances in Opto-Electronics)," *Springer*, 1991.

[17] Prof. D. Jäger, "Einführung in die Lasertechnik," *Lecture notes*, Universität Duisburg-Essen, September 2006.

[18] P. G. Gallion and G. Debarge, "Quantum Phase Noise and Field Correlation in Single Frequency Semiconductor Laser Systems," *IEEE J. Quantum Electron.*, vol. QE-20, no. 4, pp. 343-349, 1984.

[19] K. Y. Lau and A. Yariv, "Ultra-high Speed Semiconductor Lasers," *IEEE J. Quantum Electron.*, vol. QE-21, no. 2, pp. 121-138, 1985.

[20] JDSU, "Relative Intensity Noise, Phase Noise, and Linewidth," *Application note*, 2006. [Online]. Available: www.jdsunph.com

[21] W. Franz, "Einfluß eines elektrischen Feldes auf eine optische Absorptionskante," *Z. Naturforsch.* Teil A, vol. 13, 1958.

[22] L. V. Keldysh, "Behaviour of non-metallic crystals in strong electric fields", *J. Exp. Theor. Phys. (USSR)*, vol. 33, 1957; translation: *Sov. Phys. JETP*, vol. 6, 1958.

[23] L. Lever, Z. Ikonic, and R. W. Kelsall, "Quantum-confined Stark effect electro-absorption modulators for CMOS compatible photonics," *6th IEEE Int. Conf. on Group IV Photonics*, pp. 169-171, 2009.

[24] S. Haxha, B. M. A. Rahman, and K. T. V. Grattan, "Bandwidth estimation for ultra-high-speed lithium niobate modulators," *Applied Optics*, vol. 42, no. 15, pp. 2674-2682, 2003.

[25] E. L. Wooten, K. M. Kissa, A. Yi-Yan, E. J. Murphy, D. A. Lafaw, P. F. Hallemeier, D. Maack, D. V. Attanasio, D. J. Fritz, G. J. McBrien, and D. E. Bossi, "A Review of Lithium Niobate Modulators for Fiber-Optic Communication Systems," *IEEE J. Selected Topics Quantum Electron.*, vol. 6, no. 1, pp. 69-82, 2000.

[26] R. Paschotta, "Encyclopedia of Laser Physics and Technology," *Wiley-VCH*, 2008. [Also Online]. Available: www.rp-photonics.com/encyclopedia.html

[27] M. Weiß, "60 GHz photonic millimeter-wave communication systems," *Ph.D. dissertation*, Universität Duisburg-Essen, Germany, 2010.

[28] C. H. Cox, III, "Analog optical links – Theory and practice," *Cambridge University Press*, 2004

[29] S. Walklin and J. Conradi, "Effect of Mach–Zehnder Modulator DC Extinction Ratio on Residual Chirp-Induced Dispersion in 10-Gb/s Binary and AM-PSK Duobinary Lightwave Systems," *IEEE Photon. Technol. Lett.*, vol. 9, no. 10, pp. 1400-1402, 1997.

[30] N. Courjal, J. M. Dudley and H. Porte, "Extinction-ratio-independent method for chirp measurements of Mach-Zehnder modulators," *Optics Express*, vol. 12, no. 3, pp. 442-448, 2004.

[31] M. T. Abuelma'Atti, "Large Signal Analysis of the Mach-Zehnder Modulator with Variable BIAS," *Proc. Natl. Sci. Counc. ROC(A)*, vol. 25, no. 4, pp. 254-258, 2001.

[32] S. Dubovitsky, W. H. Steier, S. Yegnanarayanan, and B. Jalali, "Analysis and Improvement of Mach–Zehnder Modulator Linearity Performance for Chirped and Tunable Optical Carriers," *IEEE J. Lightwave Technol.*, vol. 20, no. 5, pp. 886-891, 2002.

[33] A. G. Armada and M. Calvo, "Phase Noise and Sub-Carrier Spacing Effects on the Performance of an OFDM Communication System," *IEEE Comm. Letters*, vol. 2, no. 1, pp. 11-13, 1998.

[34] R. Hofstetter, H. Schmuck, and R. Heidemann, "Dispersion Effects in Optical Millimeter-Wave Systems Using Self-Heterodyne Method for Transport and Generation," *IEEE Trans. Microw. Theory and Techn.*, vol. 43, no. 9, pp. 2263-2269, 1995.

[35] G. Qi, J. Yao, J. Seregelyi, S. Paquet, and C. Bélisle, "Generation and Distribution of a Wide-Band Continuously Tunable Millimeter-Wave Signal With an Optical External Modulation Technique," *IEEE Trans. Microw. Theory and Techn.*, vol. 53, no. 10, pp. 3090-3097, 2005.

[36] N. W. McLachlan, "Bessel functions for engineers," *Oxford University Press*, 2nd edition, 1955.

[37] X. Yu, H. Zhang, and X. Zheng, "High carrier suppression double sideband modulation using polarization state rotation filter and optical external modulator," *Optics Communications*, vol. 267, pp. 83-87, 2006.

[38] M. J. Connelly, "Semiconductor Optical Amplifier," *Kluwer Academic Publishers*, 2004.

[39] G. P. Agrawal, "Nonlinear Fiber Optics," *Academic Press*, 3rd edition, 2001.

[40] C. W. Thiel, "Four-Wave Mixing and its Applications," *[Online]*. Available: http://www.physics.montana.edu/students/thiel/docs/FWMixing.pdf

[41] Y. R. Shen, "The Principles of Nonlinear Optics," *Wiley-Interscience*, Wiley Classics Library Edition, 2003.

[42] P. N. Butcher and D. Cotter, "The Elements of Nonlinear Optics," *Cambridge University Press*, 1990.

[43] S. J. Garth and C. Pask, "Four-photon mixing and dispersion in single-mode fibers," *Optics Letters*, vol. 11, no. 6, pp. 380-382, 1986.

[44] P. Baldeck and R. Alfano, "Intensity effects on the stimulated four photon spectra generated by picosecond pulses in optical fibers," *IEEE J. Lightwave Technol.*, vol. 5, no. 12, pp. 1712-1715, 1987.

[45] C. J. McKinstrie, G. G. Luther, and S. H. Batha, "Signal enhancement in collinear four-wave mixing," *J. Opt. Soc. Am. B*, vol. 7, no. 3, pp. 340-344, 1990.

[46] T. Yamamoto and M. Nakazawa, "Highly efficient four-wave mixing in an optical fiber with intensity dependent phase matching," *IEEE Photon. Technol. Lett.*, vol. 9, no. 3, pp. 327-329, 1997.

[47] M. Eiselt, "Limits on WDM systems due to four-wave mixing: a statistical approach," *IEEE J. Lightwave Technol.*, vol. 17, no. 11, pp. 2261-2267, 1999.

[48] C. Wu, H. Fan, and N. K. Dutta, "Small signal analysis of frequency response of four-wave mixing in semiconductor optical amplifiers," *J. Appl. Phys.*, vol. 87, no. 5, pp. 2076-2078, 2000.

[49] A. Mecozzi, S. Scotti, A. D'Ottavi, E. Iannone, and P. Spano, "Four-Wave Mixing in Traveling-Wave Semiconductor Amplifiers," *IEEE J. Quantum Electron.*, vol. 31, no. 4, pp. 689-699, 1995.

[50] D. Cassioli, S. Scotti, and A. Mecozzi, "A Time-Domain Computer Simulator of the Nonlinear Response of Semiconductor Optical Amplifiers," *IEEE J. Quantum Electron.*, vol. 36, no. 9, pp. 1072-1080, 2000.

[51] L. F. Tiemeijer, "Effects of nonlinear gain on four-wave mixing and asymmetric gain saturation in a semiconductor laser amplifier," *Appl. Phys. Lett.*, vol. 59, no. 5, pp. 499-501, 1991.

[52] K. Kikuchi, M. Kakui, C.-E. Zah, and T.-P. Lee, "Observation of highly nondegenerate four-wave mixing in 1.5 μm traveling-wave semiconductor optical amplifiers and estimation of nonlinear gain coefficient," *IEEE J. Quantum Electron.*, vol. 28, no. 1, pp. 151-156, 1992.

[53] J. Zhou, N. Park, J. W. Dawson, K. J. Vahala, M. A. Newkirk, and B. I. Miller, "Terahertz four-wave mixing spectroscopy for study of ultrafast dynamics in a semiconductor optical amplifier," *Appl. Phys. Lett.*, vol. 63, no. 9, pp. 1179-1181, 1993.

[54] K. Kikuchi, M. Amano, C. E. Zah, and T. P. Lee, "Analysis of origin of nonlinear gain in 1.5 μm semiconductor active layers by highly nondegenerate four-wave mixing," *Appl. Phys. Lett.*, vol. 64, no. 5, pp. 548-550, 1994.

[55] M. P. Kesler and E. P. Ippen, "Subpicosecond gain dynamics in GaAlAs laser diodes," *Appl. Phys. Lett.*, vol. 51, no. 22, pp. 1765-1767. 1987.

[56] K. L. Hall, J. Mark, E. P. Ippen, and G. Eisenstein, "Femtosecond gain dynamics in InGaAsP optical amplifers," *Appl. Phys. Lett.*, vol. 56, no. 18, pp. 1740-1742, 1990.

[57] S. Diez, C. Schmidt, R. Ludwig, H. G. Weber, K. Obermann, S. Kindt, I. Koltchanov, and K. Petermann, "Four-Wave Mixing in Semiconductor Optical Amplifiers for Frequency Conversion and Fast Optical Switching," *IEEE J. Sel. Topics in Quantum Electron.*, vol. 3, no. 5, pp. 1131-1145, 1997.

[58] G. P. Agrawal, "Population pulsation and nondegenerate four-wave mixing in semiconductor lasers and amplifiers," *J. Opt. Soc. Am. B*, vol. 5, no. 1, pp. 147-159, 1988.

[59] C. T. Politi, D. Klonidis, and M. J. O'Mahony, "Dynamic Behavior of Wavelength Converters Based on FWM in SOAs," *IEEE J. Quantum Electron.*, vol. 42, no. 2, pp. 108-125, 2006.

[60] G, Bramann, H.-J. Wünsche, U. Busolt, C. Schmidt, M. Schlak, B. Sartorius, and H.-P. Nolting, "Two-Wave Competition in Ultralong Semiconductor Optical Amplifiers," *IEEE J. Quantum Electron.*, vol. 41, no. 10, pp. 1260-1267, 2005.

[61] A. Mecozzi and J. Mørk, "Saturation Effects in Nondegenerate Four-Wave Mixing Between Short Optical Pulses in Semiconductor Laser Amplifiers," *IEEE J. Sel. Topics in Quantum Electron.*, vol. 3, no. 5, pp. 1190-1207, 1997.

[62] F. P. Kapron, D. B. Keck, and R. D. Maurer, "Radiation losses in glass optical waveguides," *Appl. Phys. Lett.*, vol. 17, no. 10, pp. 423-425, 1970.

[63] W. G. French, J. B. MacChesney, P. B. O'Connor and G. W. Tasker, "Optical waveguides with very low loss," *Bell System Technical Journal*, vol. 53, pp. 951-954, 1974.

[64] T. Miya, Y. Terunuma, T. Hosaka, and T. Miyashita, "Ultimate low-loss single-mode fibre at 1.55 µm," *Electron. Lett.*, vol. 15, no. 4, pp. 106-108, 1979.

[65] Prof. Dr. rer. nat. habil. D. Jäger, "Technische Elektronik III – Optoelektronik," *Lecture Script*, Fachgebiet Optoelektronik, Universität Duisburg-Essen, 2003.

[66] G. J. Meslener, "Chromatic Dispersion Induced Distortion of Modulated Monochromatic Light Employing Direct Detection," *IEEE J. Quantum Electron.*, vol. QE-20, no. 10, pp. 1208-1216, 1984.

[67] S. Kaneko, A. Adachi, J. Yamashita, and H. Watanabe, "A Compensation Method for Dispersion-Induced Third-Order Intermodulation Distortion Using an Etalon," *J. Lightwave Technol.*, vol. 14, no. 12, pp. 2786-2792, 1996.

[68] C. H. Lee, "Microwave Photonics," *CRC Press*, 2007.

[69] A. Stöhr, K. Kitayama, and T. Kuri, "Fiber-Length Extension in an Optical 60-GHz Transmission System Using an EA-Modulator with Negative Chirp," *IEEE Photon. Technol. Lett.*, vol. 11, no. 6, pp. 739-741, 1999.

[70] G. P. Agrawal, "Fiber-Optic Communication Systems," *Wiley-Interscience*, 3rd edition, 2002.

[71] J. P. Gordon and H. Kogelnik, "PMD fundamentals: Polarization mode dispersion in optical fibers," *Proc. Nat. Academy Sc. (PNAS)*, vol. 97, no. 9, pp. 4541-4550, 2000.

[72] J. Piprek, "Semiconductor Optoelectronic Devices – Introduction to Physics and Simulation," *Academic Press*, 2003.

[73] J. E. Bowers and C. A. Burrus, "Ultrawide-Band Long-Wavelength p-i-n Photodetectors," *J. Lightw. Technol.*, vol. LT-5, no. 10, pp. 1339-1350, 1987.

[74] K. Kato, "Ultrawide-Band/High-Frequency Photodetectors," *IEEE Trans. Microwave Theory Techn.*, vol. 47, no. 7, pp. 1265-1281, 1999.

[75] M. Gökkavas, O. Dosunmu, M. S. Ünlü, G. Ulu, R. P. Mirin, D. H. Christensen, and E. Özbay, "High-Speed High-Efficiency Large-Area Resonant Cavity Enhanced p-i-n Photodiodes for Multimode Fiber Communications," *IEEE Photon. Technol. Lett.*, vol. 13, no. 12, pp. 1349-1351, 2001.

[76] M. Dentan and B. de Cremoux, "Numerical Simulation of the Nonlinear Response of a p-i-n Photodiode Under High Illumination," *J. Lightw. Technol.*, vol. 8, no. 8, pp. 1137-1144, 1990.

[77] A. Alping, "Waveguide *pin* photodetectors: theoretical analysis and design criteria," *IEE Proceedings*, vol. 136, pt. J, no. 3, pp. 177-182, 1989.

[78] D. Wake, T. P. Spooner, S. D. Perrin, and I. D. Henning, "50 GHz InGaAs Edge-Coupled *pin* Photodetector," *Electron. Lett.*, vol. 27, no. 12, pp. 1073-1075, 1991.

[79] K. Kato, A. Kozen, Y. Muramoto, Y. Itaya, T. Nagatsuma, and M. Yaita, "110-GHz, 50%-Efficiency Mushroom-Mesa Waveguide p-i-n Photodiode for a 1.55-μm Wavelength," *IEEE Photon. Technol. Lett.*, vol. 6, no. 6, pp. 719-721, 1994.

[80] u^2t Photonics AG, "Device model: XPDV2140R," http://www.u2t.com, Jan. 2011.

[81] T. Ishibashi, N. Shimizu, S. Kodama, H. Ito, T. Nagatsuma, and T. Furuta, "Uni-Traveling-Carrier Photodiodes," *OSA TOPS on Ultrafast Electronics and Optoelectronics*, vol. 13, pp. 83-87, 1997.

[82] N. Shimizu, Y. Muramoto, Y. Miyamoto, and T. Ishibashi, "High Speed InP/InGaAs Uni-Traveling-Carrier Photodiodes," *Int. Conf. on Indium Phosphide and Related Materials*, pp. 313-316, May 2000.

[83] H. Ito, T. Furuta, S. Kodama, and T. Ishibashi, "InP/InGaAs uni-traveling-carrier photodiode with 310GHz bandwidth," *Electron. Lett.*, vol. 36, no. 21, pp. 1809-1810, 2000.

[84] H. Ito, T. Nagatsuma, A. Hirata, T. Minotani, A. Sasaki, Y. Hirota, and T. Ishibashi, "High-power photonic millimetre wave generation at 100GHz using matching-circuit-integrated uni-traveling-carrier photodiodes," *IEE Proc.-Optoelectron.*, vol. 150, no. 2, pp. 138-142, 2003.

[85] P.-L. Liu, J. Williams, M. Y. Frankel, and R. D. Esman, "Saturation Characteristics of Fast Photodetectors," *IEEE Trans. Microwave Theory Techn.*, vol. 47, no. 7, pp. 1297-1303, 1999.

[86] H. Ito, S. Kodama, Y. Muramoto, T. Furuta, T. Nagatsuma, and T. Ishibashi, "High-Speed and High-Output InP-InGaAs Unitraveling-Carrier Photodiodes," *IEEE J. Sel. Top. Quantum Electron.*, vol. 10, no. 4, pp. 709-727, 2004.

[87] H. Ito, F. Nakajima, T. Furuta, and T. Ishibashi, "Continuous THz-wave generation using antenna-integrated uni-traveling-carrier photodiodes," *Semicond. Sci. Technol.*, vol. 20, pp. S191-S198, 2005.

[88] A. Stöhr, R. Heinzelmann, C. Kaczmarek, and D. Jäger, "Ultra-broadband K_a to W-band 1.55µm traveling-wave photomixer," *Electron. Lett.*, vol. 36, no. 11, pp. 970-972, 2000.

[89] A. Malcoci, "Photonische Lokaloszillatoren für Anwendungen in der Terahertz-Radioastronomie," *Ph.D. dissertation*, Universität Duisburg-Essen, 2006.

[90] A. Stöhr, R. Heinzelmann, A. Malcoci, and D. Jäger, "Optical Heterodyne Millimeter-Wave Generation Using 1.55-µm Traveling-Wave Photodetectors," *IEEE Trans. Microw. Theory Techn.*, vol. 49, no. 10, pp. 1926-1933, 2001.

[91] K. S. Giboney, M. J. W. Rodwell, and J. E. Bowers, "Traveling-Wave Photodetector Theory," *IEEE Trans. Microw. Theory Techn.*, vol. 45, no. 8, pp. 1310-1319, 1997.

[92] J.-W. Shi, K.-G. Gan, Y.-J. Chiu, Y.-H. Chen, C.-K. Sun, Y.-J. Yang, and J. E. Bowers, "Metal-Semiconductor-Metal Traveling-Wave Photodetectors," *IEEE Photon. Technol. Lett.*, vol. 16, no. 6, pp. 623-625, 2001.

[93] A. Stöhr, A. Malcoci, A. Sauerwald, I. C. Mayorga, R. Güsten, and D. S. Jäger, "Ultra-Wide-Band Traveling-Wave Photodetectors for Photonic Local Oscillators," *J. Lightw. Technol.*, vol. 21, no. 12, pp. 3062-3070, 2003.

[94] J. Rutman and F. L. Walls, "Characterization of Frequency Stability In Precision Frequency Sources," *Proc. IEEE*, vol. 79, no. 7, pp. 952-960, 1991.

[95] I. Jacobs, "Dependence of Optical Amplifier Noise Figure on Relative-Intensity-Noise," *J. Lightw. Technol.*, vol. 13, no. 7, pp. 1461-1465, 1995.

[96] E. I. Ackerman, W. K. Burns, G. E. Betts, J. X. Chen, J. L. Prince, M. D. Regan, H. V. Roussell, and C. H. Cox III, "RF-Over-Fiber Links With Very Low Noise Figure," *J. Lightw. Technol.*, vol. 26, no. 15, pp. 2441-2448, 2008.

[97] J. B. Johnson, "Thermal agitation of electricity in conductors," *Phys. Rev.*, vol. 32, pp. 97-109, 1928.

[98] H. Nyquist, "Thermal agitation of electric charge in conductors," *Phys. Rev.*, vol. 32, pp. 110-113, 1928.

[99] W. Schottky, "Über spontane Stromschwankungen in verschiedenen Elektrizitätsleitern," *Annalen der Physik*, vol. 362, no. 23, pp. 541-567, 1918.

[100] S. B. Alexander, "Optical Communication Receiver Design," *SPIE*, 1997.

[101] G. N. Milford, C. C. Harb, and E. H. Huntington, "Shot noise limited, microwave bandwidth photodetector design," *Rev. Sci. Instrum.*, vol. 77, pp. 114701-(1-6), 2006.

[102] B. Wilson, Z. Ghassemlooy, and I. Darwazeh, "Analogue Optical Fibre Communications," *Institution of Electrical Engineers*, 1995.

[103] D. M. Baney and W. V. Sorin, "Broadband Frequency Characterization of Optical Receivers Using Intensity Noise," *Hewlett-Packard Journal*, issue Feb. 1995, pp. 6-12, 1995.

[104] X. Fernando and H. Kosek, "Improved Expression for Intensity Noise in Subcarrier Multiplexed Fiber Networks," *Int. J. Microw. Opt. Tech.*, vol. 2, no. 2, pp. 153-161, 2007.

[105] P. C. Becker, N. A. Olsson, and J. R. Simpson, "Erbium-Doped Fiber Amplifiers: Fundamentals and Technology," *Academic Press*, 1999.

[106] G. R. Walker, R. C. Steele, and N. G. Walker, "Measurement of Semiconductor Laser Amplifier Noise Figure in Coherent Optical Transmission System," *Electron. Lett.*, vol. 25, no. 25, pp. 1681-1682, 1989.

[107] R. C. Steele, G. R. Walker, and N. G. Walker, "Sensitivity of Optically Preamplified Receivers with Optical Filtering," *IEEE Photon. Technol. Lett.*, vol. 3, no. 6, pp. 545-547, 1991.

[108] I. P. Kaminow and T. L. Koch, "Optical Fiber Telecommunications IIIB," *Academic Press*, 1997.

[109] J. Rutman, "Characterization of Phase and Frequency Instabilities in Precision Frequency Sources: Fifteen Years of Progress," *Proc. IEEE*, vol. 66, no. 9, pp. 1048-1075, 1978.

[110] E. Rubiola, "Phase Noise and Frequency Stability in Oscillators," *Cambridge University Press*, 2009.

[111] Mini-Circuits Inc., "Characterizing and minimizing VCO phase noise," *Application note VCO15-6*, 1999.

[112] E. J. Baghdady, R. N. Lincoln, and B. D. Nelin, "Short-term frequency stability: Characterization, theory, and measurement," *IEEE Proceedings*, vol. 53, no. 7, pp. 704-722, 1965.

[113] B. Razavi, "A Study of Phase Noise in CMOS Oscillators," *IEEE J. Solid-State Circuits*, vol. 31, no. 3, pp. 331-343, 1996.

[114] B. H. Leung, "VLSI for Wireless Communication," *Prentice Hall Electronics and VLSI Series*, 2002.

[115] M. Poulin, C. Latrasse, M. Morin, S. Ayotte, and F. Costin, "Effect of Laser Decorrelation on the Phase Noise of RF Signals Generated by Optical Mixing of Modulation Sidebands," *Int. Topical Meeting on Microwave Photonics*, Oct. 5-9, Montreal, Canada, 2010.

[116] E. Rubiola, E. Salik, S. Huang, N. Yu, and L. Maleki, "Photonic-delay technique for phase-noise measurement of microwave oscillators," *J. Opt. Soc. Am. B*, vol. 22, no. 5, pp. 987-997, 2005.

[117] S. Camatel and V. Ferrero, "Narrow Linewidth CW Laser Phase Noise Characterization Methods for Coherent Transmission System Applications," *J. Lightw. Technol.*, vol. 26, no. 17, pp. 3048-3055, 2008.

[118] C.C.I.R. study group, "Characterization of frequency and phase noise," *Report 580*, TN-162, pp. 142-150, 1986.

[119] J. J. Grobbelaar, "Phase Noise Measurement," *Master Thesis*, Stellenbosch University, South-Africa, 2011.

[120] G. Qi, J. Yao, J. Seregelyi, S. Paquet, C. Bélisle, X. Zhang, K. Wu, and R. Kashyap, "Phase-Noise Analysis of Optically Generated Millimeter-Wave Signals With External Optical Modulation Techniques," *J. Lightw. Technol.*, vol. 24, no. 12, pp. 4861-4875, 2006.

[121] IEEE Standards Coordinating Committee 27, "IEEE Standard Definitions of Physical Quantities for Fundamental Frequency and Time Metrology - Random Instabilities," *IEEE Std. 1139 – 2008*, pp. c1 – 35, Feb. 2009.

[122] W. P. Robins, "Phase noise in signal sources," *Peter Peregrinus Ltd.*, 1982.

[123] E. Rubiola, "The Leeson Effect – Phase Noise in Quasilinear Oscillators," *arXiv:physics/0502143v1*, 2005.

[124] L. Goldberg, A. Yurek, H. F. Taylor, and J. F. Weller, "35 GHz microwave signal generation with an injection-locked laser diode," *Electron Lett.*, vol. 21, no. 18, pp. 714-715, 1985.

[125] S. Fukushima, C. F. C. Silva, Y. Muramoto, and A. J. Seeds, "Optoelectronic millimeter-wave synthesis using an optical frequency comb Generator, optically

injection locked lasers, and a unitraveling-carrier photodiode," *J. Lightw. Technol.*, vol. 21, no. 12, pp. 3043-3051, 2003.

[126] V. Ferrero and S. Camatel, "Optical Phase Locking techniques: an overview and a novel method based on Single Side Sub-Carrier modulation," *Optics Express*, vol. 16, no. 2, pp. 818-821, Jan. 2008.

[127] K. J. Williams, "6–34 GHz offset phase locking of Nd: YAG 1319 nm nonplanar ring lasers," *Electron. Lett.*, vol. 25, no. 18, pp. 1242–1243, Aug. 1989.

[128] J.-F. Cliché, B. Shillue, M. Têtu, and M. Poulin, "A 100-GHz-tunable photonic millimeter wave synthesizer for the Atacama Large Millimeter Array radiotelescope," in *proceedings of IEEE MTTS conference*, pp. 349-352, 3.-8. June 2007.

[129] S. Kawanishi, A. Takada, and M. Saruwatari, "Wide-Band Frequency-Response Measurement of Optical Receivers Using Optical Heterodyne Detection," *J. Lightwave Technol.*, vol. 7, no. 1, pp. 92-98, Jan. 1989.

[130] A. Beling, H. Pan, and J. C. Campbell, "High-Power High-Linearity InGaAs/InP Photodiodes," *ECS Transactions*, vol. 16, no. 41, pp. 39-48, 2009.

[131] IEEE Instrumentation and Measurement Society, "IEEE Standard for Precision Coaxial Connectors (DC to 110 Ghz)," *IEEE Std. 287-2007*, pp. C1-119, 2007.

[132] G. H. Smith, D. Novak, and Z. Ahmed, "Overcoming Chromatic-Dispersion Effects in Fiber-Wireless Systems Incorporating External Modulators," *IEEE Trans. Microw. Theory Techn.*, vol. 45, no. 8, pp. 1410-1415, 1997.

[133] B. Masella and X. Zhang, "Linearized optical single sideband Mach-Zehnder electro-optic modulator for radio over fiber systems," *Optics Express*, vol. 16, no. 12, pp. 9181-9190, 2008.

[134] D. Hervé, J. L. Corral, J. M. Fuster, J. Herrera, A. Martinez, V. Polo, F. Ramos, E. Vourc'h, and J. Marti, "Techniques for the Compensation for Chromatic-Dispersion Effects in Fiber-Wireless Systems," *U.R.S.I. The Radio Science Bulletin*, vol. 309, pp. 26-37, 2004.

[135] J. J. O'Reilly, P. M. Lane, R. Heidemann, and R. Hofstetter, "Optical generation of very narrow linewidth millimeter signals," *Electron. Letters*, vol. 28, no. 25, pp. 2309-2311, Dec. 1992.

[136] Y. Shen, X. Zhang, and K. Chen, "Optical carrier-suppression of microwave signals with stimulated Brillouin scattering in long fiber ring," *Microwave Opt. Techn. Lett.*, vol. 43, no. 3, Nov. 2004.

[137] J. Zhang, H. Chen, M. Chen, T. Wang, and S. Xie, "A Photonic Microwave Frequency Quadrupler Using Two Cascaded Intensity Modulators With Repetitious Optical Carrier Suppression," *IEEE Photon. Technol. Lett.*, vol. 19, no. 14, pp. 1057-1059, 2007.

[138] X. S. Yao and L. Maleki, "Converting light into spectrally pure microwave oscillation," *Optics Letters*, vol. 21, no. 7, pp. 483-485, 1996.

[139] X. S. Yao and L. Maleki, "Optoelectronic microwave oscillator," *J. Opt. Soc. Am. B*, vol. 13, no. 8, pp. 1725-1735, 1996.

[140] X. S. Yao and L. Maleki, "Multiloop Optoelectronic Oscillator," *IEEE J. Quantum Electron.*, vol. 36, no. 1, pp. 79-84, 2000.

[141] T. Bánky, B. Horváth, and T. Berceli, "Optimum configuration of multiloop optoelectronic oscillators," *J. Opt. Soc. Am B*, vol. 23, no. 7, pp. 1371-1380, 2006.

[142] D. Eliyahu and L. Maleki, "Low Phase Noise and Spurious Level in Multi-Loop Opto-Electronic Oscillators," *Proceedings of the 2003 IEEE Int. Freq. Control Symp. and PDA Exhibition*, pp. 405-410, 2003.

[143] K.-H. Lee, J.-Y. Kim, and W.-Y. Choi, "Injection-Locked Hybrid Optoelectronic Oscillators for Single-Mode Operation," *IEEE Photon. Technol. Lett.*, vol. 20, no. 19, pp. 1645-1647, 2008.

[144] O. Pottiez, O. Deparis, R. Kiyan, M. Haelterman, P. Emplit, P. Mégret, and M. Blondel, "Supermode Noise of Harmonically Mode-Locked Erbium Fiber Lasers With Composite Cavity," *IEEE J. Quantum Electron.*, vol. 38, no. 3, pp. 252-259, 2002.

Appendix

This appendix gives a list of the major components and measurement equipment used in this thesis.

Component	Experiments in chapter	Manufacturer & Type
24 GHz LO source	3	INWAVE GmbH prototype
Bias source	3, 4	Keithley 2400 Source Meter
EDFA 1	3, 4	IPG Photonics EAD-200CL
EDFA 2	3, 4	Polytec Low noise EDFA
Electrical spectrum analyzer	3, 4	HP 8565E
Harmonic V-band mixer	3	HP 11970V
Harmonic W-band mixer	3	Agilent 11970W
High-pass filter 1	4	Mini Circuits VHF-8400+
High-pass filter 2	4	MFC 17416 (custom design)
Laser source	3, 4	Agilent 8164B / 81680A
Limiting amplifier	3	Farran FLNA-10
Low noise amplifier	4	Mini Circuits ZVA-183-S+
LO source	3	Anritsu 68087B Synthesizer
Mach-Zehnder modulator	3, 4	2x Fujitsu FTM7938EZ
Optical band-pass filter	3	Tecos FC-1550B-1-1
Phase shifter	3, 4	ATM P1608
Photodiode	3, 4	u^2t Photonics AG XPDV2120R
SOA 1	3	Covega/Thorlabs SOA-1117
SOA 2	3	Covega/Thorlabs BOA-1004
Tunable laser source	3	HP 8168F